Theoretical and experimental investigations of creep groan in automotive disk brakes

vorgelegt von
M.Sc.
Xingwei Zhao
geb. in Hunan, China

von der Fakultät V - Verkehrs- und Maschinensysteme
der Technischen Universität Berlin
zur Erlangung des akademischen Grades

Doktor der Ingenieurwissenschaften
-Dr.-Ing.-

genehmigte Dissertation

Promotionsausschuss:

Vorsitzender: Prof. Dr. rer. nat. Wolfgang H. Müller
Gutachter: Prof. Dr.-Ing. Utz von Wagner
Gutachter: Prof. Dr.-Ing. Hartmut Hetzler

Tag der wissenschaftlichen Aussprache: 21. Dezember 2017

Berlin 2018

Acknowledgments

Contents

1 Introduction

1.1 Background and motivation

The brake is one of the most important safety and performance components of vehicles. On the one hand, the development of brakes has focused on the increase of braking power and reliability. On the other hand, the refinement of vehicle acoustics and comfort of vehicle design have increased the relative contribution of brake noise, vibration and harshness (NVH). A consumer may believe that the NVH problem is symptomatic of a defective brake and file a warranty claim, even though the brake is functioning as designed in all other parts [1], [2]. The entire automotive industry can attest to NVH repairs often dominating warranty claims at aftermarket service center and dealerships. Abendroth and Wernitz denote that many makers of materials for brake pads spend up to 50% of their engineering budgets on NVH issues [3]. Concentrating on NVH performance can be drawn back to the early 1990s, engineers focused much of their attention on eliminating high-frequency squeals. There is a wealth of literature on automotive disk brake squeal. Reviews conducted in the last 30 years provide a comprehensive source of information [4]. In contrast, creep groan received much less attention. However, this type of vibration receives a growing interest from the automotive industry because it primarily affects the comfort. Like other brake noise problems such as brake squeal, creep groan may bring complaints of customers, which eventually causes warranty claims and results in refinement costs to the industry.

1.1.1 NVH problems in vehicle brakes

In general, brake vibration and/or noise can be classified into many categories based on the occurring frequencies, such as judder, creep groan, moan, and squeal [5], [6]. As shown in Table 1.1, in the low-frequency range (0-1000 Hz) there are in general three different types of structural vibrations, named judder, creep groan, and moan, while squeal occurs in the high-frequency range (>1000 Hz).

- Brake squeal is a high frequency vibration noise, which is in general higher than 1000 Hz. It is caused by the flutter instability [7]-[17]. Squeal is a friction-induced self-excited oscillation. When an unstable equilibrium solution exists in the system, the system oscillates with increasing amplitude from the equilibrium solution and reaches a limit cycle (LC). The limit cycle oscillation can generate sound, and the brake disk emits the sound.

- Moan shows the same excitation mechanisms as low frequency squeal. It is a self excited vibration, where the equilibrium solution of the system becomes unstable due to the friction coupling of vibration modes. During moan, the harmonic vibration of brake carrier and axle can normally be observed [18], [19].

- Judder is caused by periodic features on the rotor surface that result in cyclic brake torques. The typical feature of this type of noise is that its frequency is a multiple of the rotor speed of rotation [20]-[26].

- Creep groan is a low frequency vibration noise caused by the stick-slip-effect, which describes the brake pad's total or partial, alternating adhesion and sliding on the disk. The phenomenon may take place whenever the brake is slowly released while the car starts moving from a statio-

nary state, which is a frequent problem of vehicles with automatic transmissions due to the continuous driving torque on the drive shaft [27]-[33].

Brake noise	Frequency region	Occurrence brake pressure	Occurrence speed	Triggering source
Judder [20]-[26]	Around 10 Hz	Low brake pressure	Proportional to speed	Forced vibration
Moan [18], [19]	100-1000 Hz	Low brake pressure	High speed	Self-excited (flutter instability)
Creep groan [27]-[33]	0-500 Hz	High brake pressure	Low speed	Self-excited (stick-slip)
Squeal [7]-[17]	>1000 Hz	Low brake pressure	High speed	Self-excited (flutter instability)

Table 1.1: NVH problems in vehicle brake

1.1.2 Friction law and stick-slip motion

Tribology is the study of adhesion, friction, lubrication and wear of surfaces in relative motion. It remains important today as it was in ancient times, arising in the fields of physics, chemistry, geology, biology and engineering [34]. Friction is a classical field that tracks back to Leonardo da Vinci, Guillaume Amontons, and Charles Augustin de Coulomb [35]. Amontons pointed out that the friction force is proportional to normal load but does not depend on the area of the apparent contact surface. Coulomb proposed a model where the friction force is opposite to the direction of velocity with a magnitude proportional to the normal force. Besides, it describes a static force at zero sliding velocity to be larger than a kinetic force at finite sliding velocities [36]. Measurements of the contact surface of rocks show that the friction force is proportional to true contact area, which is typically much less than the apparent contact surface [37], [38]. By measuring the velocity dependence of friction, Stribeck found that friction decreases with increasing velocity in certain velocity regimes. This phenomenon is called the Stribeck effect [39].

Stick-slip vibration is characterized by a sawtooth displacement-time evolution [40] which has clearly defined stick and slip regions. It appears in everyday life as well as in engineering systems, such as the sound of bowed instruments, creaking doors, rattling joints of a robot, creep groan of brake systems, and chattering machine tools [41].

The stick-slip motion can in the simplest usual way modeled as a 1-degree-of-freedom (DOF) system coupled with Coulomb's friction law. When dry friction is modeled as Coulomb's friction law, self-sustained stick-slip motion may occur [42]-[46]. Coulomb's friction model is normally described by piecewise differentiable equations, with switching between the stick and slip region. The way to solve these piecewise differentiable equations is studied in literature [47]-[53]. Popp *et at.* employed a point-mapping approach to calculate the stick-slip limit cycle [47], while Leine *et al.* studied the shooting method to find the limit cycle by solving a two-point boundary-value problem [48]. Another method to

solve the piecewise differentiable equations is so called "switch method". During the "switch method" the numerical calculation starts from an initial state with a differential equation. After each time step it is inspected if possible switch conditions within this time step are satisfied. If the switch conditions are satisfied, a new integration process is started with a modified set of differential equations and its initial conditions are the state at the switching point [49]. Based on the studies of flows for non-smooth dynamic systems, the switching conditions of a non-smooth system can be calculated by finding the separation boundaries of flows [50]-[53]. Due to the non-smooth characteristics of the stick-slip motion, chaotic motion can occur as well as multi-periodic solutions. Bilinear and nonlinear dynamic models have been considered to explain such friction phenomena as stick-slip, chatter and chaos by Ibrahim [54], [55]. Galvanetto and Knudsen described an event map of a two DOFs mechanical system under self-sustained oscillations induced by dry friction, and the parameter dependent bifurcation behavior is analyzed by the defined mappings [56]. Popp *et al.* proposed that the limit cycles of stick-slip vibrations can be broken up by a harmonic disturbance, and the bifurcation behavior and the chaos of a stick-slip system under external excitation are studied for different system parameters [41]. Storck *et al.* proposed that the friction will be reduced in presence of ultrasonic vibration [57]. Some scholars stated that the static friction coefficient can be strongly reduced under a normal or lateral mechanical oscillation [58]-[61].

With further investigations of friction law, it is well known that the phenomena such as pre-sliding, rate dependence, and hysteresis have been observed experimentally and are reproduced only by dynamic models [62]-[64]. As a result, the simple classical static models of Coulomb, Stribeck, etc. have given way gradually to more sophisticated, dynamical models with due attention to presiding hysteresis and time-lag effects. Dahl developed a simple dynamic friction model with one state in the late 1960s, which is widely used to simulate aerospace systems [65], [66]. However, this model does not capture the Stribeck effect and thus cannot predict stick-slip motion. Later, the LuGre model is an extension of the Dahl model that can describe the Stribeck effect, stick-slip effect, and hysteresis [67]-[71]. Canudas de Wit *et al.* [71] analyzed the stick-slip experiment using the LuGre friction model, whose gross features of the behavior are similar to those obtained with Coulomb's model, but the transitions are captured by dynamics for the LuGre friction model. Li *et al.* studied the bifurcation and chaos in friction-induced vibration through the LuGre friction model [72].

Thanks to the availability of measurement techniques and equipments such as scanning probe microscopy, laser interferometry, and the surface force apparatus, it is possible to measure friction at the nanoscale [73]. Mate *et al.* first introduced the friction force microscope (FFM) in 1987. It becomes possible to observe the atomic friction processes for a tip sliding over graphite [74], [75]. Later, Tomanek *et al.* proposed an accurate description of the microscopic mechanism of energy dissipation in the friction force microscope [76]. On the atomic scale, several experiments confirm that the friction force on the nanometer scale exhibits a sawtooth behavior, commonly known as atomic stick-slip [77]. As a result, the Prandtl-Tomlinson model is proposed to explain the frictional stick-slip motion on the atomic scale [78], [79]. Socoliuc *el at.* confirmed that the atomic stick-slip motion can be eliminated under a normal mechanical oscillation [80], [81]. A comparison of different friction laws is shown in Table 1.2.

Name	Equations	Described friction characteristics
Coulomb friction law [36]	$F = F_d \, \text{sgn}(v),$ slip $F \in [-F_s, F_s],$ stick	Stick-slip
Dahl model [65]	$\dfrac{dz}{dt} = v - \dfrac{\sigma_0}{F_c}|v|z$ $F = \sigma_0 z$	Hysteresis
LuGre model [67]	$\dfrac{dz}{dt} = v - \sigma_0 \dfrac{|v|}{g(v)} z$ $g(v) = F_d + (F_s - F_d)\exp\left(-|v/v_s|^\alpha\right)$ $F = \sigma_0 z + \sigma_1 z + f(v)$	Stribeck effect Hysteresis Stick-slip
Prandtl-Tomlinson model [78]	$m\ddot{z} = F - \sigma_1 \dot{z} - F_d \sin(\lambda_0 z)$	Atom stick-slip

Table 1.2: Different friction laws

1.1.3 Creep groan

It is well accepted that creep groan is caused by the stick-slip-effect [27]-[30], [82]-[89]. Some works focus on the experimental study of creep groan. Jang *et al.* investigated creep groan propensity of different friction materials, and proposed that the creep groan can be eliminated by employing the friction material with less difference between the static and dynamic friction coefficient [82]. Fuadi *et al.* studied a fundamental mechanism for creep groan generation by adopting a caliper-slider experimental model, where a map that shows the necessary condition for avoiding creep groan was introduced [83], [84].

Other literature works on the fundamental mechanism of creep groan noise generation as well as the corresponding suppression methods. Brecht *et al.* [29], [30] measured the vibration characteristics of creep groan and studied the stick-slip limit cycle of creep groan. Jung *et al.* measured the interior noise in the event of creep groan noise by using a chassis dynamometer, and the way to reduce creep groan noise was studied experimentally [85]. Vadari *et al.* stated the stiffness as one of the most important parameters in brake creep groan generation [86], and Donley *et al.* through experimental observations demonstrated that the structure of the McPherson's suspension system is the key to damp creep groan [87]. Zhang *at el.* studied the conditions leading to creep groan noise through road tests, as well as objective characteristics of creep groan noise [88]. Neis *et al.* combined in-vehicle tests and laboratory-scaled tribometer tests to seek the conditions of creep groan noise occurrences [89]. Bettella *et al.* focused on the transmission of the vibration from the brake component regions to the cockpit during creep groan, and showed that the airborne transmission can be neglected compared to structure-borne path [90]. Gauterin *et al.* studied creep groan of disk brakes of cars and explained how creep groan originates and permitted the assessment of corrective measures [91].

With respect to modeling, the stick-slip-effect has in general been modeled by corresponding dynamic systems coupled with Coulomb's friction law. Crowther *et al.* investigated the brake creep groan prob-

lem by formulating the issues in terms of two dynamic sub-systems coupled with Coulomb's friction law [92], [93]. Hegde *et al.* focused on the nonlinear dynamic transient analysis of brake vibration with a multi-body dynamic simulation [94]. Brecht *et al.* [29], [30] studied the stick-slip limit cycle of creep groan with 3 DOFs minimal model coupling with Coulomb's friction law as well as with finite element model. However, the model using Coulomb's friction law cannot explain several effects during creep groan. Hetzler *et al.* [95]-[99] presented an analytical investigation on stability and bifurcation behavior of a friction oscillator, where a friction model is described by Coulomb's friction law coupled with the Stribeck effect.

Some works of the author referring to creep groan have been published in [31]-[33]. A comparison study of the creep groan models with Coulomb's friction law and the bristle friction law is proposed in [31]. Furthermore, a 1 DOF model in [32] and a 2 DOFs model in [33] with the bristle friction law are investigated to describe the fundamental mechanism of creep groan. The simulation results are compared with the experimental results measured in the test rig with an idealized brake in [31]-[33], and in [33] the experimental results in a test rig with a real brake is also analyzed.

1.2 Objective of the work

Motivated by the aforementioned observations, the main objective of this thesis is to study the fundamental mechanism of creep groan on brake systems, as well as the suppression methods of creep groan. To be specific, the tasks of this thesis are stated as follows:

- Design and set up test rigs with an idealized brake and a real brake. Creep groan should be generated in both test rigs. The fundamental mechanism of creep groan should be investigated based on the experimental results.

- Investigation of minimal models of creep groan, so that the friction induced stick-slip motion will be carefully studied for a deeper understanding of creep groan.

- Investigation of the multiple degrees of freedom model to describe creep groan of a real brake. A reduced-order model will be studied to improve calculation efficiency.

- Search for methods against creep groan. The feasibility and effectiveness of the methods should be confirmed through experiments.

1.3 Outline of the work

The organization of this thesis is described as follows. According to the general introduction on creep groan and NVH issues of brake system given in Chapter 1, Chapter 2 first presents the construction of test rigs with an idealized brake and with a real brake. Then, the experimental results during creep groan from both test rigs are shown to give a first impression of creep groan.

In Chapter 3, based on the experimental results, minimal models of creep groan for an idealized brake are investigated. Both Coulomb's friction law and the bristle friction law are employed to describe the friction force. By coupling the minimal model with different friction laws, the stability of the equilibrium solution as well as the stick-slip limit cycle of the nonlinear system is studied. According to that, the system has different parameter regions with different types of motion.

Chapter 4 focuses on the study of the parameter identification for different friction models. After parameter identification, the theoretical and experimental results are compared with each other quantitatively. Experimental results confirm the existence of three different parameter regions. In addition, a friction force observer is designed and the observed friction force is compared with the simulated friction force.

The study of creep groan on the test rig with a real brake is presented in Chapter 5. A large number of degrees of freedom model and a corresponding reduced-order model are set up to describe the brake system. Numerical simulation shows that the reduced-order model can describe creep groan with high calculation efficiency and limited error.

Countermeasures against creep groan are finally discussed in Chapter 6. A pad, which contains piezo-ceramic staple actuators, is successfully used to suppress creep groan by exciting a high frequency oscillation of the system. Besides, the risk of the generation of creep groan can also be reduced by increasing the damping of the shaft. Another method to shorten the time of creep groan is an optimal brake technique, through that the system can leave the regions with creep groan rapidly. By integrating this optimal brake technique into an anti-lock braking system (ABS), the ABS can perform the optimal braking process through a simple control loop to avoid creep groan.

Chapter 7 concludes the thesis and discusses the future scope.

2 Experimental Investigations of Creep Groan

In this chapter, the test rigs and the experimental results are presented to give a first impression of creep groan. In order to understand creep groan step by step, a test rig with an idealized brake was designed and assembled at MMD TU Berlin. Subsequently, a test rig with a real brake was set up as a comparison study with that of an idealized brake. The stick-slip limit cycle can be measured in both test rigs. According to the measurements, the mechanism of creep groan will be explained in this chapter.

2.1 Test rig with an idealized brake

Creep groan of brake systems is a well-known low frequency vibration noise caused by the stick-slip-effect, which describes the brake pad's total or partial, alternating adhesion and sliding on the disk [27]-[30], [83]-[94]. The phenomenon may take place whenever light pressure is exerted by the driver on the brake pedal and some forces are acting on the vehicle, such as an idling engine through an automatic transmission, or gravity due to the vehicle on a slope.

The structure a front-wheel drive vehicle is shown in Fig. 2.1, where a suspension is hung in a chassis, and a brake system is attached to the suspension. A drive shaft driven by motor is connected to the disk, while a wheel is connected to the other side of the disk with wheel bolts. If a car is an automatic car, the motor-disk-pad sub-system is the prime part relevant to creep groan.
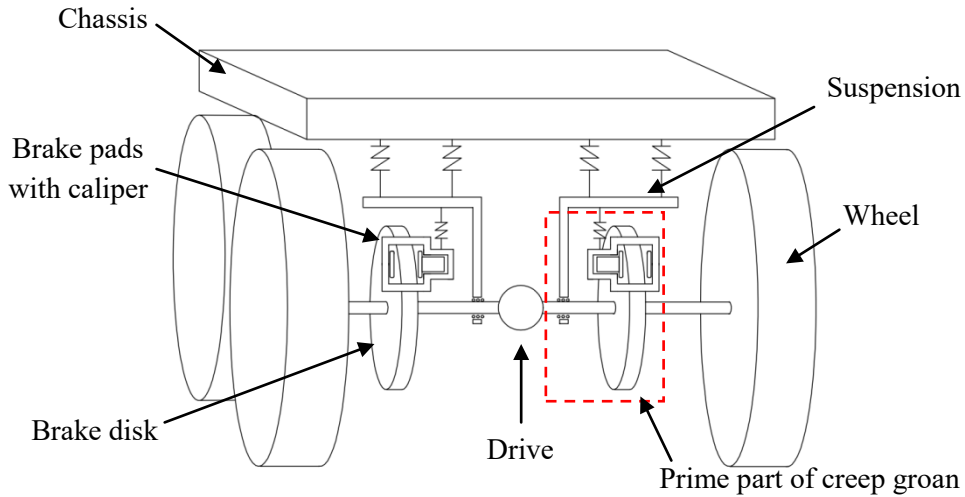

Fig. 2.1: Structure of a front-wheel drive vehicle in front view

In order to concentrate on the investigation of the frictional contact, a test rig with an idealized brake has been designed and assembled. The intention of designing this set-up is to concentrate on the pad-disk contact. Therefore, the brake disk, the drive shaft, the brake pads, the brake caliper, and the brake carrier are taken out from a real vehicle to constitute the test rig; but the difficult-to-model parts, such as the complicated structure of the carrier and the rubber coated pins on the carrier, are replaced by an idealized carrier, which consists of two L-shaped steel plates. This idealized carrier has high stiffness in the in-plane direction and low stiffness in the out-of-plane direction. To make sure that the stiffness

of the carrier has comparable order of stiffness similar to the real brake carrier, a finite element (FE) analysis is performed to calculate the stiffness of a real carrier in the in-plane direction. In the FE analysis, the screw hole of the caliper is set as fixed position, while a lateral force is acting on the both pads. Fig. 2.2 shows the FE analysis results, where the stiffness in the in-plane direction is $8.21 \cdot 10^7 \, \text{N/m}$ in the piston side and $2.33 \cdot 10^7 \, \text{N/m}$ in the other side. Those two steel plates are designed according to the calculated stiffness.
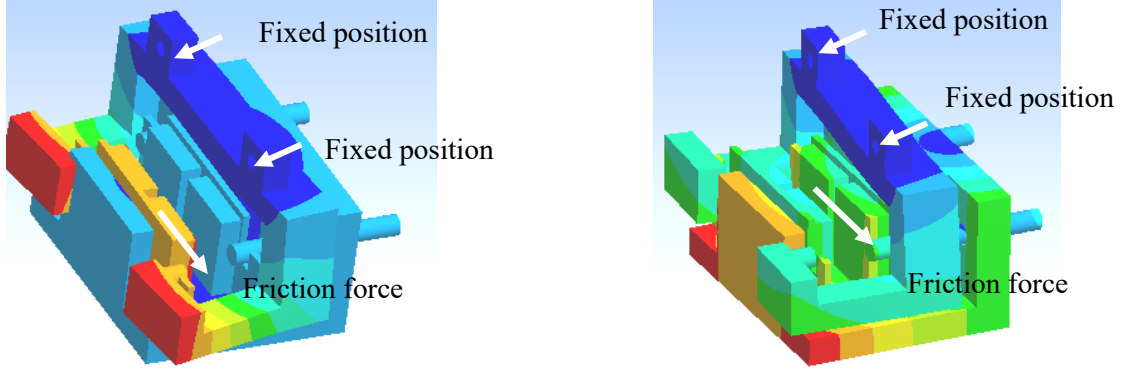

Fig. 2.2: FE analysis of the brake carrier

An AC motor coupled with a reduction gear box is used as drive, which can provide a low revolution speed with high moment. A shaft is assembled between the reduction gear box and a brake disk. Brake pads are fixed on the long edges of the steel plate, and the short edges are fixed on the frame. The brake caliper is hung on the long edges of the steel plates, and provides the brake pressure with a hydraulic system. The CAD model of the test rig is sketched in Fig. 2.3. The test rig has some advantages for the experimental investigation of creep groan, such as:

1. The test rig is similar with the brake system of a real car, since the pads, the disk, the shaft and the caliper of the test rig come from a real car;

2. The test rig has simple structure of the components and therefore the parameters are easy to identify and there is less uncertainty in dynamics;

3. The test rig is easy to equip with different types of sensors.

In order to observe creep groan in the test rig, sensors have been fitted in suitable positions, shown in Fig 2.4. An accelerometer is attached to the carrier, which measures the acceleration of the pad. A turning angle transmitter is connected to the disk by which the absolute angle and angular velocity of the disk can be measured. The pressure of the brake can be read from a pressure meter. Strain sensors are placed in the middle of the drive shaft. Once the shaft has a torsional deformation, the change of the electrical resistance of the strain sensor can be measured by a Wheatstone bridge, which is related to the strain. The calibration of the strain sensor is performed by a static measurement and its relationship to the torsional angle $\Delta\theta$ is identified [100]. Information on sensors is given in Table 2.1.
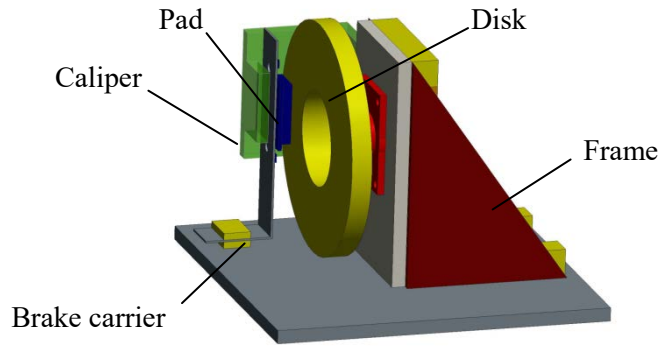
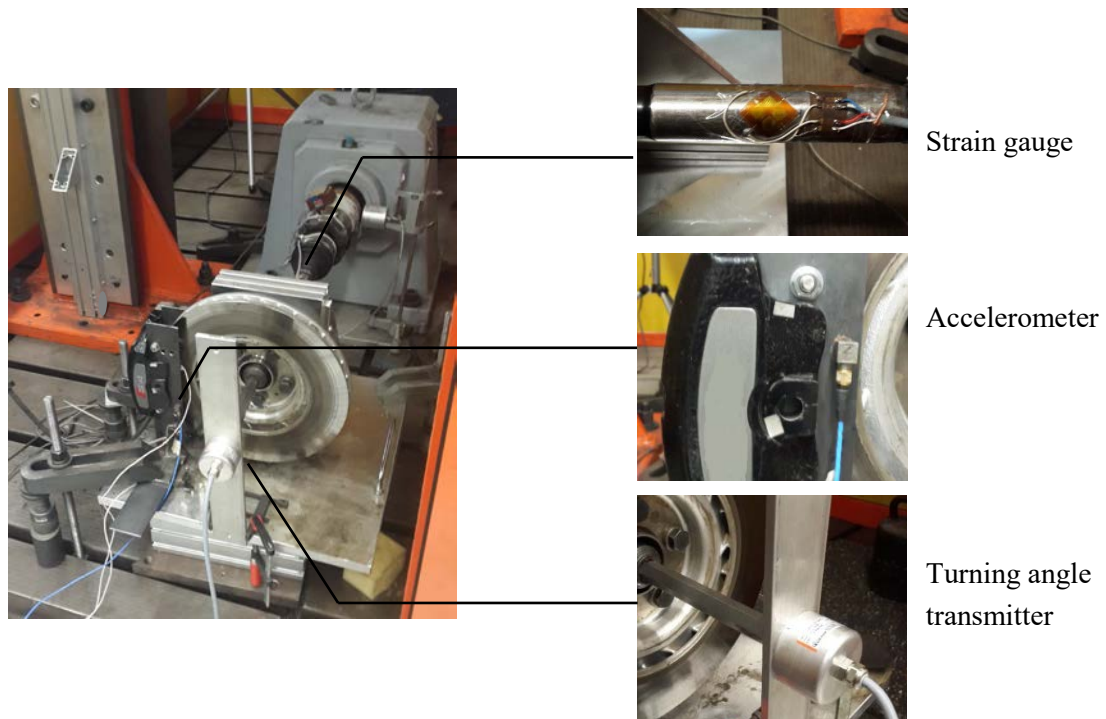Fig. 2.3: CAD drawing of the test rig with an idealized brake

Fig. 2.4: Test rig with an idealized brake and the corresponding sensors

Before applying an experimental investigation, modal analysis is performed [101]. The eigenfrequencies and corresponding eigenmodes are presented in Table 2.2 [100]. The disk has eigenfrequencies at 1400 Hz, 1871 Hz and 3148 Hz (with free-free boundary condition), while the L-shaped steel plate has eigenfrequencies at 16 Hz, 174 Hz and 300 Hz (with fix-free boundary condition). The torsional eigenfrequency of the shaft is at 36.5 Hz (with fix-free boundary condition). Since creep groan is lower than 500 Hz, it will be more related to the components with lower eingenfrequencies, such as the L-shaped steel plate and the shaft.

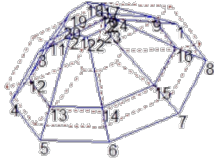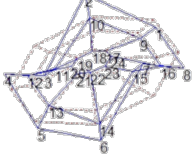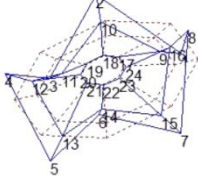| Sensor	Parameters
Accelerometer	PCB 4507 ICP accelerometers, frequency range 0.3 Hz–6 kHz, sensitivity 101.2 mV/g
Turning angle transmitter	Power supply 5 V DC, maximum sample rate 40 kHz, resolution 14 bit
Data acquisition module	Featuring four 24-bit simultaneously sampled A/D channels, maximum sample rate 80 kHz, and analogue anti-aliasing filter

Table 2.1: Information of sensors
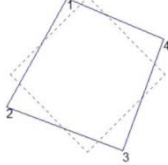
	1400 Hz	1871 Hz	3148 Hz
Disk			
	16 Hz	174 Hz	300 Hz
L-shaped steel plate			
Shaft	36.5 Hz		

Table 2.2. Eigenfrequencies and eigenmodes of the components [100]

The experiment is performed at the speed 0.2 rad/s with brake pressure 9 bar. The measured torsional angle and acceleration are displayed in Fig. 2.5 without creep groan, where only small vibration can be observed in the torsional angle and acceleration signals. Fig. 2.6 (a) and (b) show the torsional angle of the shaft $\Delta\theta$ measured from the strain sensors on the drive shaft and its time derivative $\Delta\dot{\theta}$ (torsional velocity) during creep groan. In the experimental results, the typical stick-slip motion can be observed: in the stick region, $\Delta\dot{\theta}$ is approximately constant and $\Delta\theta$ increases linearly; in the slip region, $\Delta\dot{\theta}$ changes with time. The acceleration of the brake pad is given in Fig. 2.6 (c) measured from the accelerometer on the brake carrier. There is a large impulse when the system is shifting from stick to slip, which is caused by sudden change of the friction.
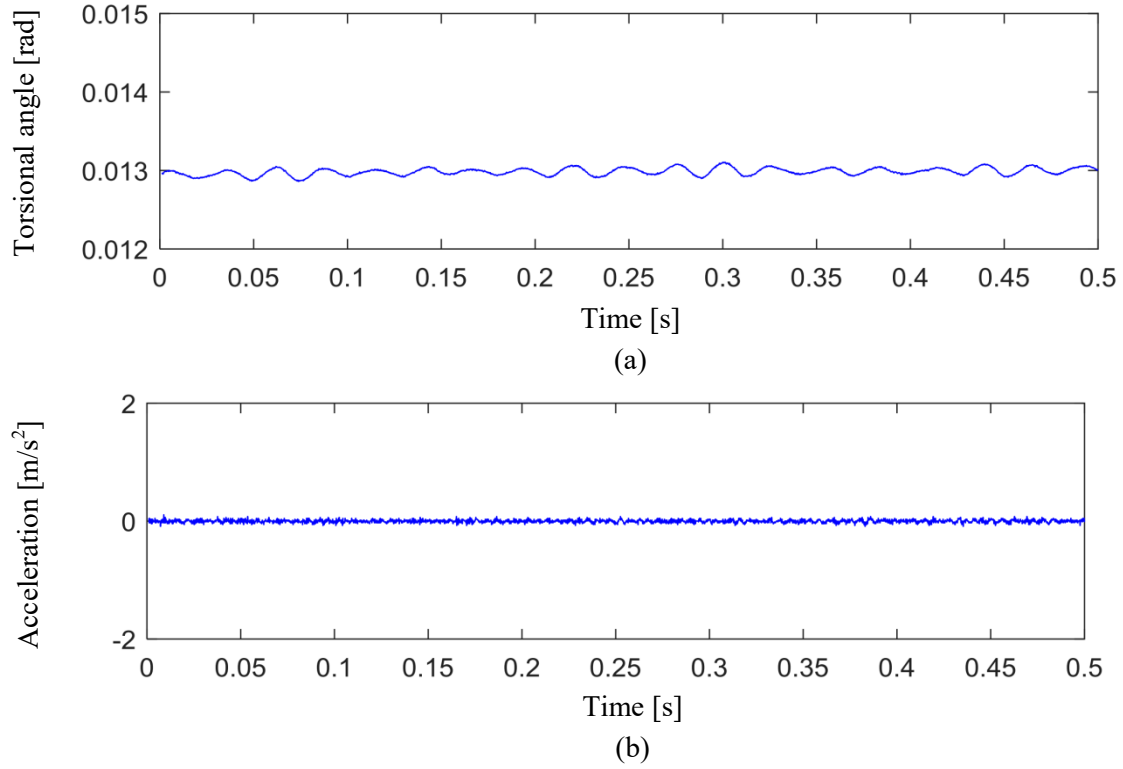
Fig. 2.5: Torsional angle of the shaft (a) and acceleration of the pad (b) without creep groan

The frequency spectra of the torsional velocity and the acceleration during creep groan are exhibited in Fig. 2.7 by pursuing Discrete Fast Fourier Transformation (DFFT). The spectrum of the torsional angle shows a single peak at 36.25 Hz, which is the frequency of the stick-slip motion. It is noticed that this frequency is close to the eigenfrequency of the shaft, which implies that the shaft may be the primary part related to creep groan. The spectrum of the pad oscillation shows a lot of peaks, which are much higher than the frequency of the stick-slip motion, such as 146 Hz, 256 Hz and 292 Hz. These frequencies are approached to the eigenfrequencies of the L-shaped steel plate, which are heard felt by the human during creep groan. The measured frequencies are lower than the first eigenfrequency of the disk, so that it is possible to consider the disk as a rigid body during the study of creep groan.
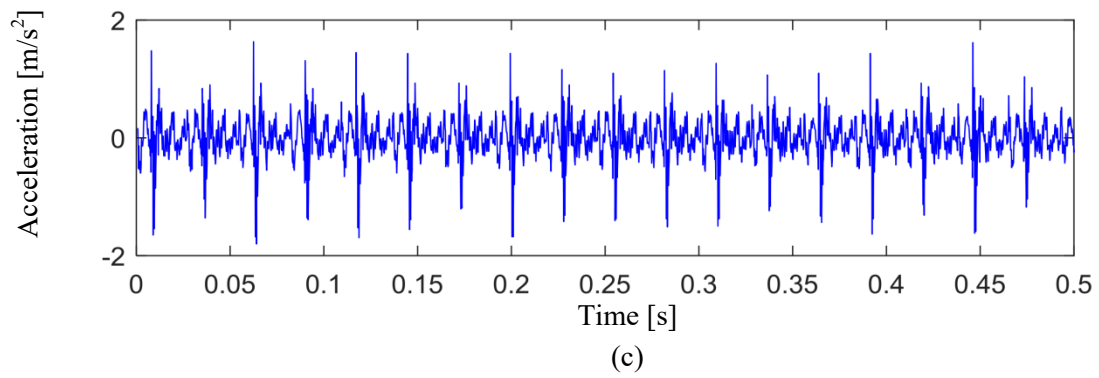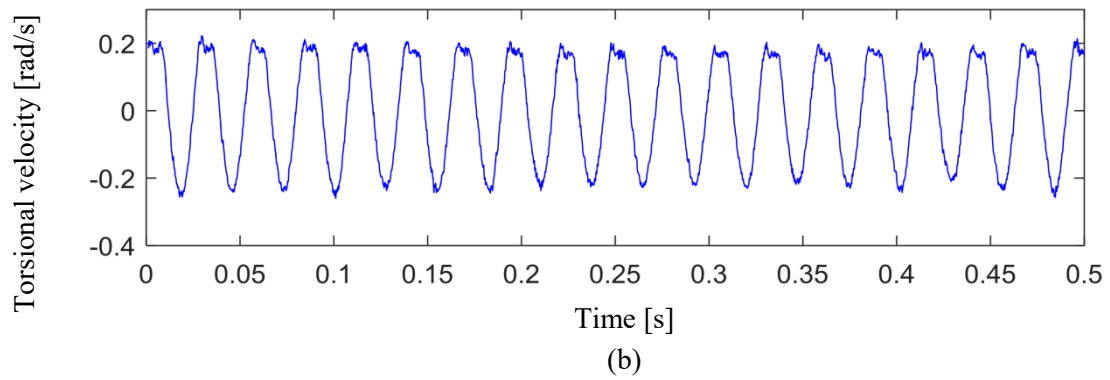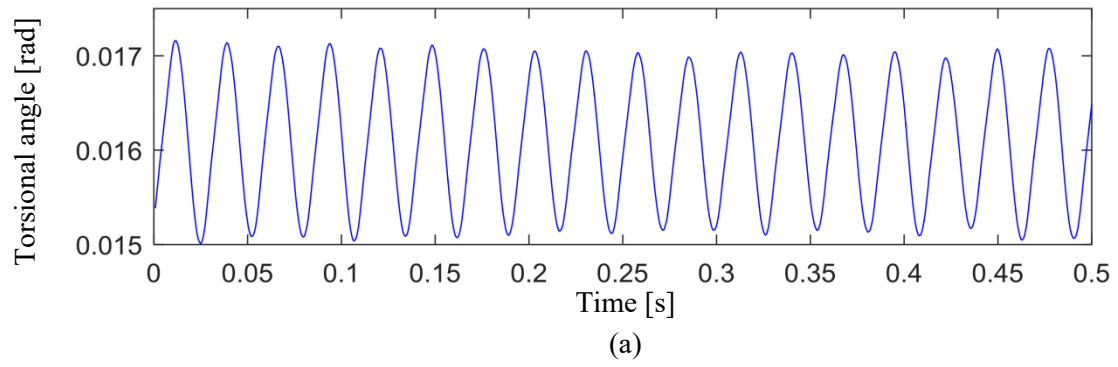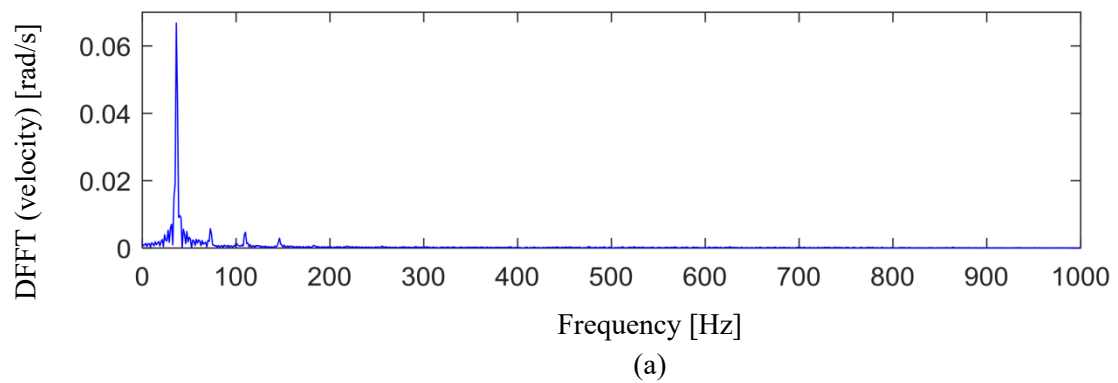
Fig. 2.6: Torsional angle (a) and torsional velocity (b) of the shaft and acceleration (c) of brake pad during creep groan
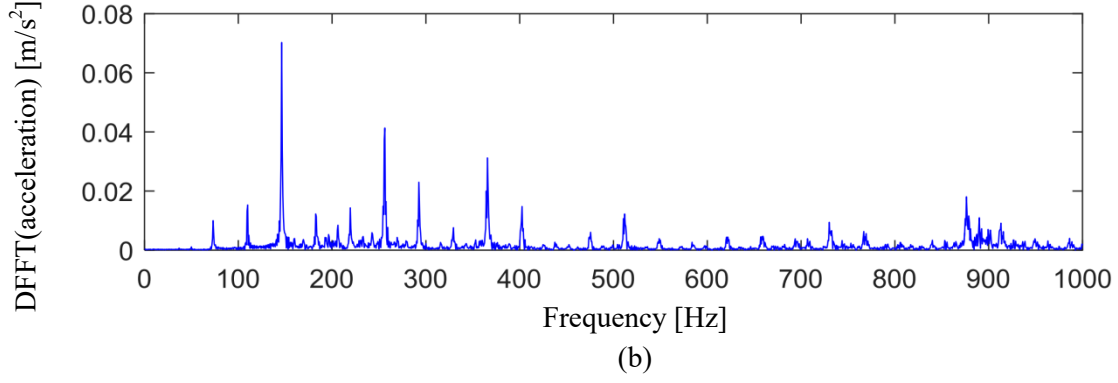
Fig. 2.7: Frequency spectra of torsional velocity of the shaft (a) and acceleration of the pad (b)

Fig. 2.8 shows the measured stick-slip limit cycles with the pressure at 5, 7, 9 and 11 bar, where its horizontal axis is $\Delta\theta$ and the vertical axis is $\Delta\dot{\theta}$. It is clear that the amplitude of the limit cycle increases with the pressure. Experimental results confirm that the stick-slip happens during creep groan. As a result, the friction force is switched between the static and dynamic friction forces, and the vibrations in the brake pad and the brake carrier are excited by the varied friction force. Creep groan is the resulting vibrations that can be heard or felt by humans.
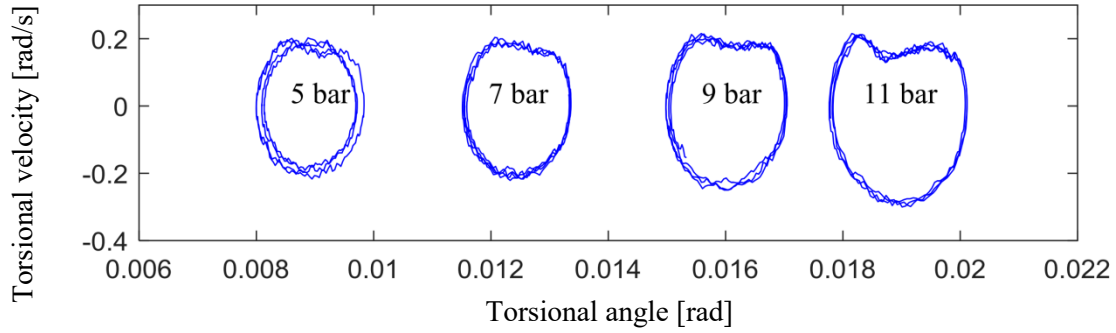
Fig. 2.8: Stick-slip limit cycles under different brake pressure

2.2 Test rig with a real brake

As a comparison study, a test rig with a real brake was assembled, which constitutes the brake disk, the brake pads, the shaft, the caliper, the carrier and the suspension system. The brake carrier is assembled on the suspension, with two brake pads fixed in it. The structure of the test rig with a real brake is shown in Fig. 2.9.

Sensors are assembled in the test rig. A 3D motion and deformation sensor is used to measure the dynamic motion of the pad, the caliper and the carrier. The 3D motion and deformation sensor is a non-contact and material-independent measuring system based on digital image correlation. It offers a stable solution for point-based analyses of test objects of just a few millimeters in size [102]. The torsional angle of the drive shaft is measured by the strain sensors, and the accelerations of the pad can be measured by accelerometers. Fig. 2.10 shows the positions of the sensors.
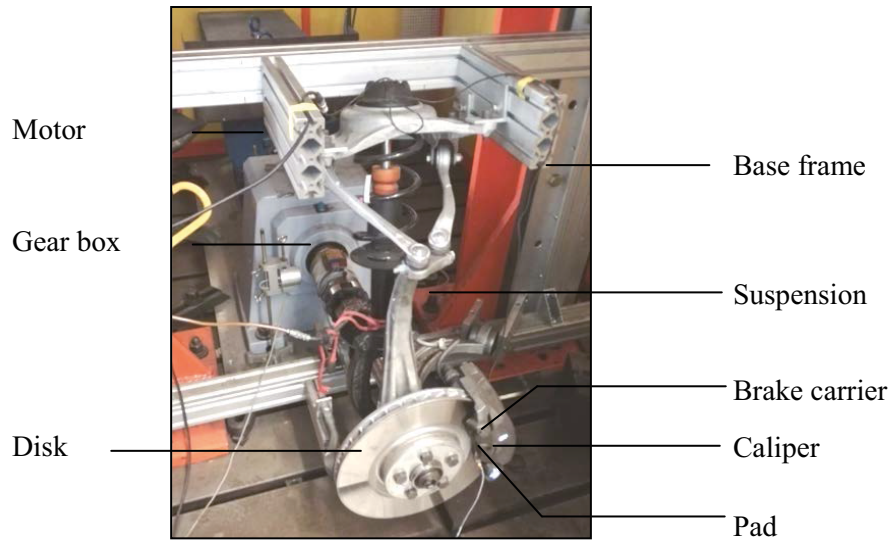
Fig. 2.9: Test rig with a real brake

3D Motion and Deformation Sensor   Strain sensor   Accelerometers

Fig. 2.10: 3D motion and deformation sensor, strain sensor, and accelerometers

The experiment was performed under the speed at 0.31 rad/s with brake pressure at 8 bar. The results from 3D motion and deformation sensor are shown in Fig. 2.11, which is measured together with Dr. Gräbner and staffs from GOM GmbH. Actually, the 3D motion and deformation sensor can measure the vibration of the brake in both in-plane and out-of-plane directions. The measurement results from our brake indicate that the out-of-plane motion can be ignored compared to the in-plane vibration during creep groan. Fig. 2.11 shows the in-plane displacements of the pad, the caliper and the carrier. It is apparent that they move almost synchronously during creep groan.
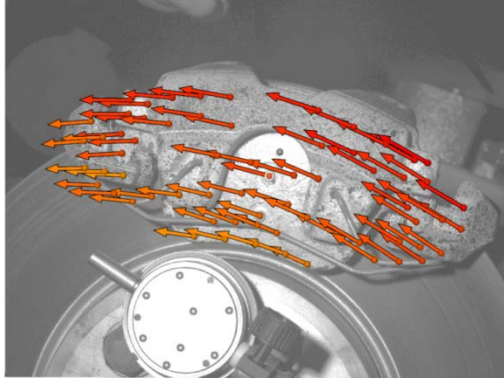
<div style="display:flex; justify-content:space-between;">
Displacements during stick
Displacements during slip
</div>
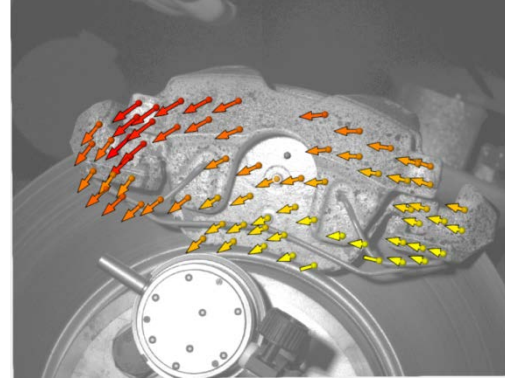
Fig. 2.11: In-plane displacements of the pad, the caliper and the carrier during creep groan, the arrows shows the relative displacement vector reference to the static position.

Fig. 2.12 (a) and (b) shows the torsional angle $\Delta\theta$ of the shaft measured from the strain sensors and the torsional angle velocity $\Delta\dot{\theta}$, which is the time derivative of $\Delta\theta$. Compared to the measurements from the test rig with an idealized brake, the similar stick-slip motion can be observed at the real brake. The acceleration of the brake pad is given in Fig. 2.12 (c) measured from the accelerometer on the brake pad. Differing from the measured acceleration at the idealized brake shown in Fig. 2.6 (c), there are double impulse signals in one stick-slip period, which are the impulse signals from stick to slip transition and from slip to stick transition.

The frequency spectra of the signals during creep groan are exhibited in Fig. 2.13 by pursuing Discrete Fast Fourier Transformation (DFFT). The spectrum of the torsional angular velocity shows double peaks, where the dominant frequency is at 30 Hz and the second frequency appears at 60 Hz. The double peaks indicate the nonlinear characteristic of the stick-slip motion. The spectrum of the acceleration of the pad is shown in Fig. 2.13 (b). Its first three peak frequencies (30 Hz, 60 Hz and 90 Hz) are the frequency of the stick-slip motion and its double and triple frequencies. The higher frequencies such as 152 Hz, 243 Hz, 366 Hz and 518 Hz are the excited vibration of the carrier by the varied friction. It is obvious that the real brake system has more high frequencies of peak than the idealized brake. Fig. 2.14 shows the experimental limit cycles with pressure at 4, 6, 8 and 10 bar. Comparing Fig. 2.8 with Fig. 2.14, similar stick-slip limit cycles can be observed in both set-ups. Besides, both results show that the size of the limit cycle increases with the brake pressure. On the other hand, the exited vibrations of pads have different frequencies in different test rigs as shown in Fig. 2.7 (b) and Fig. 2.13 (b). If a real vehicle is considered, the vibration of a chassis can also be excited by the suddenly changed friction during creep groan.
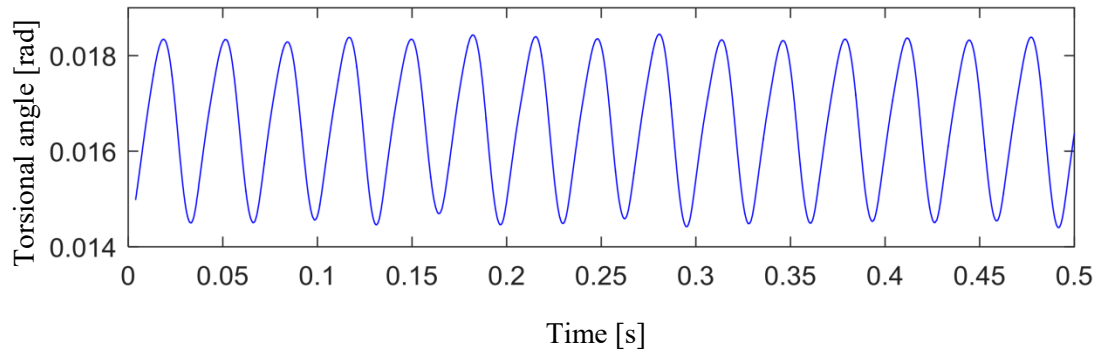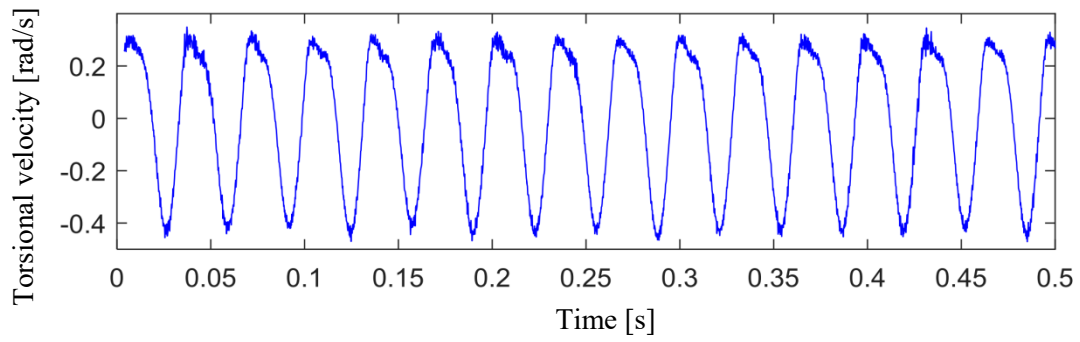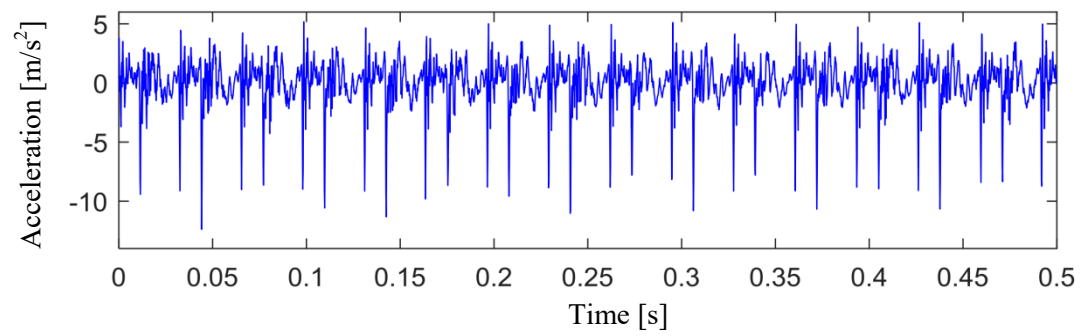
Fig. 2.12: Torsional angle (a) and torsional velocity (b) of the shaft and acceleration of brake pad during creep groan
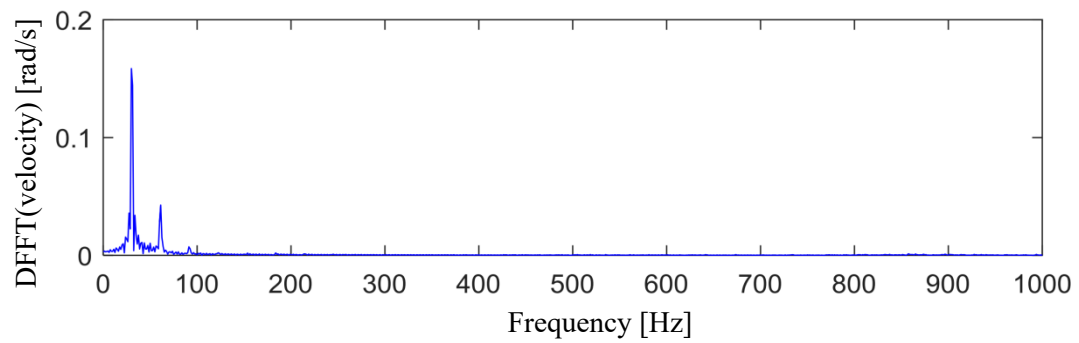
(a)
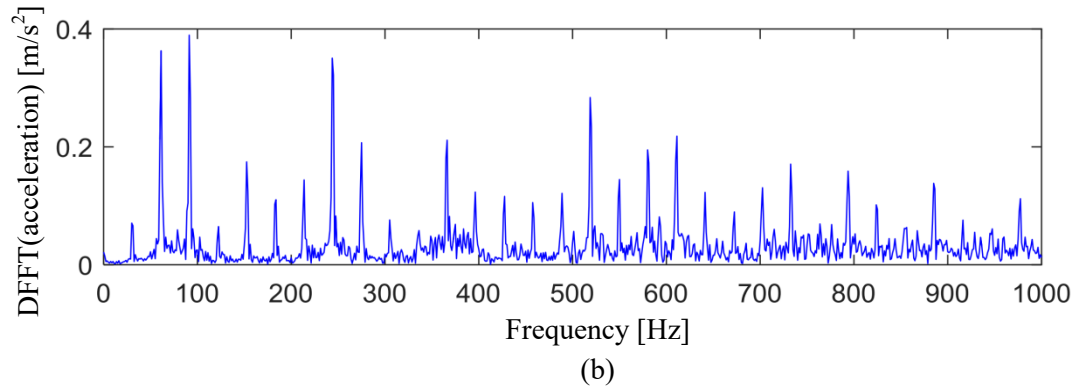
Fig. 2.13: Frequency spectra of torsional velocity (a) and acceleration of the pad (b)
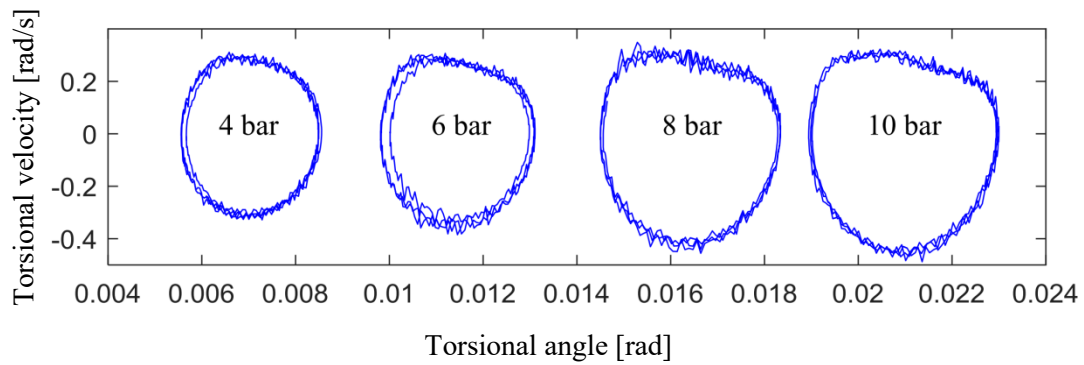
Fig. 2.14: Stick-slip limit cycles under different brake pressure

2.3   Summary

In this chapter, the design of a test rig with an idealized brake and a test rig with a real brake has been presented. In both test rigs, creep groan was measured under low velocity with high brake pressure (>4 bar). Compared the measured signals to the eigenfrequencies of each component, it implies that creep groan may relate to the shaft and brake carrier. During creep groan, stick-slip limit cycles (around 30 Hz) as well as the vibration of the carrier (between 0~500 Hz) are measured through the strain sensor and accelerometer. The stick-slip limit cycles from both test rigs are qualitatively similar with each other, but the exited vibrations of pads have different frequencies in different test rigs. Based on the measurements, models considering the motion of the shaft and the carrier, as well as friction laws including the stick-slip effect will be studied in the following chapters.

3 Theoretical Investigations of Creep Groan on the Test Rig with an Idealized Brake

In this chapter, different minimal models will be proposed to study creep groan. Compared to finite element methods with large numbers of degrees of freedom, nonlinear models with a low number of degrees of freedom are more convenient to study the basic excitation mechanism of creep groan. At first, models with Coulomb's friction law are investigated and the stick-slip limit cycle can be simulated. Subsequently, models with the bristle friction law are proposed to improve the modeling. Different models will be compared with each other. Parts of the results in this section have already been described in [31]-[33].

3.1 Minimal model with Coulomb's friction law

3.1.1 One DOF model with Coulomb's friction law
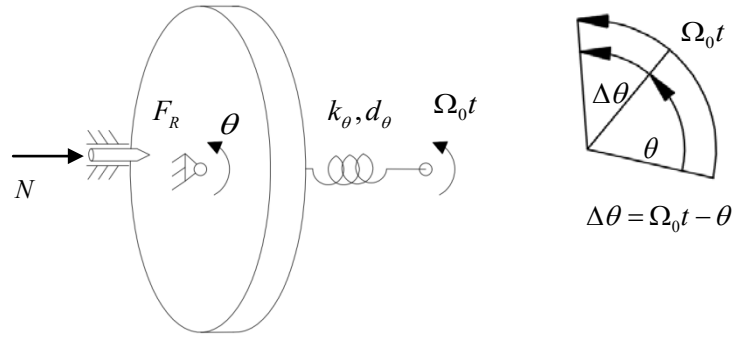
Fig. 3.1: Model of the test rig with an idealized brake with 1 DOF [31]

The model of the test rig with an idealized test rig is shown in Fig. 3.1. In this test rig, the disk is considered as a rigid body and connected to the motor by the drive shaft. The pads are fixed on the frame through the carrier. As the disk can perform only rotation but no wobbling motion, the number of pads in the subsequent model is reduced from two to one without any influence on the qualitative behavior of the system. The drive shaft is considered as a rotational spring with stiffness k_θ and damping d_θ. In this test rig, the stiffness of the drive shaft is much lower than the stiffness of the brake carrier. Therefore, only the vibration of the disk is considered for the simulation of creep groan firstly. The equation of motion for this one degree of freedom system is described by

$$I\ddot{\theta} + d_\theta\left(\dot{\theta} - \Omega_0\right) + k_\theta\left(\theta - \Omega_0 t\right) = -F_R r, \tag{3.1}$$

Replace $\Omega_0 t - \theta$ by $\Delta\theta$

$$I\Delta\ddot{\theta} + d_\theta\Delta\dot{\theta} + k_\theta\Delta\theta = F_R r, \tag{3.2}$$

where I is the moment of inertia of the disk; r is the radius of the point where the pad acts; k_θ and d_θ are the stiffness and damping of the drive shaft; $\Delta\theta$ is the torsional angle of the drive shaft superposed to the disk rotation with angle θ, $\Delta\theta$ is equal to $\Omega_0 t - \theta$, Ω_0 is the rotating speed of motor which assumed as a constant, and F_R is the friction force in the contact between the disk and pad.

In Coulomb's friction law, if the contact surfaces are at rest relative to each other, the friction force works as the static friction force, which prevent any relative motion up until a threshold force. This threshold force is characterized by the normal force times the static friction coefficient μ_s [103]. If the contact surfaces are in relative motion, the friction coefficient is the dynamic friction coefficient μ_d. μ_s is normally larger than μ_d. μ_d can be described as a constant or a velocity dependent term [43], [58], [95], [97], [104]. For the sake of simplification, μ_d is at first assumed to be constant. The contact force in the stick and slip regions is therefore given as

$$\begin{cases} F_R = N\mu_d \, \text{sgn}\left(\Omega_0 r - \Delta\dot{\theta} r\right), \text{if } \Omega_0 \neq \Delta\dot{\theta} \cup \left|N\mu_s\right| \leq \left|d_\theta \Delta\dot{\theta} + k_\theta \Delta\theta\right| \text{ (slip)} \\ F_R \in \left[-N\mu_s, N\mu_s\right], \text{if } \Omega_0 = \Delta\dot{\theta} \cap \left|N\mu_s\right| > \left|d_\theta \Delta\dot{\theta} + k_\theta \Delta\theta\right| \text{ (stick)} \end{cases} \tag{3.3}$$

where sgn means sign function, N is normal force. Note that the force law from Eq. (3.3) is multivalued, a fact that seems to contradict a unique determination of the forces between the stick and slip regions. However, if the force law is combined with some equations of motion of a dynamical system, uniqueness can be guaranteed in many cases [51], [103]. By combining the friction law with the dynamics of the brake system, the dynamic equation in the slip region ($\Omega_0 r - \Delta\dot{\theta} r > 0$) is

$$I\Delta\ddot{\theta} + d_\theta \Delta\dot{\theta} + k_\theta \Delta\theta = N\mu_d r, \text{for } \Omega_0 \neq \Delta\dot{\theta} \cup \left|N\mu_s\right| \leq \left|d_\theta \Delta\dot{\theta} + k_\theta \Delta\theta\right| \tag{3.4}$$

while the dynamic equation in the stick region is

$$\Delta\theta = \Delta\theta_0 + \Omega_0 t, \text{ for } \Omega_0 = \Delta\dot{\theta} \cap \left|N\mu_s\right| > \left|d_\theta \Delta\dot{\theta} + k_\theta \Delta\theta\right| \tag{3.5}$$

The system is then a piecewise linear system. It can be analytically solved in each region. On the one hand, the solution in the slip region is

$$\Delta\theta = \exp\left(-\frac{d_\theta}{2I}(t - t_{l0})\right)\left[C_1 \cos\left(\omega_\theta(t - t_{l0})\right) + C_2 \sin\left(\omega_\theta(t - t_{l0})\right)\right] + \Delta\theta_e, \tag{3.6}$$

$$\Delta\dot{\theta} = \left[\left(\omega_\theta C_2 - \frac{d_\theta}{2I}C_1\right)\cos\left(\omega_\theta(t - t_{l0})\right) - \left(\omega_\theta C_1 - \frac{d_\theta}{2I}C_2\right)\sin\left(\omega_\theta(t - t_{l0})\right)\right]\exp\left(-\frac{d_\theta}{2I}(t - t_{l0})\right),$$

where

$$\omega_\theta = \sqrt{\frac{k_\theta}{I} - \left(\frac{d_\theta}{2I}\right)^2}, \Delta\theta_e = Nr\mu_d / k_\theta, C_1 = \Delta\theta_{l0} - \Delta\theta_e, C_2 = \frac{1}{\omega_\theta}\left(\Delta\dot{\theta}_{l0} + \frac{d_\theta}{2I}C_1\right).$$

where t is current time, t_{l0} is the time when the system just enters the slip region, $\Delta\theta_e$ is the equilibrium position, and $\Delta\theta_{l0}$ and $\Delta\dot{\theta}_{l0}$ are the initial torsional angle and angle velocity at time t_{l0}.

On the other hand, the solution in the stick region is

$$\Delta\theta = \Omega_0(t - t_{t0}) + \Delta\theta_0,$$ (3.7)

$$\Delta\dot{\theta} = \Omega_0,$$

where t_{t0} is the time when the system just enters the stick region, and $\Delta\theta_{t0}$ is the initial torsional angle at time t_{t0}. Eqs. (3.6) and (3.7) shows that a unique solution exists when initial conditions are given.

If the brake system falls into the attractor of the stick region, its motion is described by Eq. (3.7). In contrast, its motion is described by Eq. (3.6) in the slip region. If the system is always switched between those two solutions, a stick-slip limit cycle can be observed as shown in Fig. 3.2, with the friction law shown in Fig. 3.3. In the stick region, the disk adheres to the pads, leading to the increased torsional angle of the drive shaft, and energy is stored in the drive shaft. In the slip region, the disk is separated with the pads and moves under a dynamic friction. In this region, the kinematic energy converts into heat. There is a non-smooth behavior from slip to stick or from stick to slip.
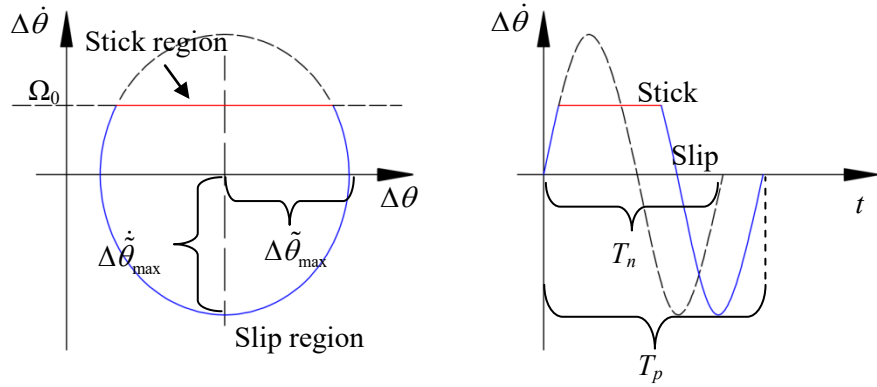
Fig. 3.2: Stick-slip motion

It should be noted that the period of the stick-slip motion T_p is larger than T_n, where T_n is the harmonic period of the system without stick-slip (dashed line in Fig. 3.2). The period of stick-slip motion is equal to the stick time plus the slip time

$$T_p = T_{st} + T_{sl},$$ (3.8)

Assuming that the damping of the system is ignored, the amplitude of the stick-slip limit cycle $\Delta\tilde{\theta}_{max}$ are approximately calculated as

$$\Delta\dot{\tilde{\theta}}_{max} = \sqrt{\Omega_0^2 + \omega_0^2 N^2 (\mu_s - \mu_d)^2 r^2}, \Delta\tilde{\theta}_{max} = \sqrt{\frac{\Omega_0^2}{\omega_0^2} + N^2(\mu_s - \mu_d)^2 r^2},$$ (3.9)

where $\Delta\tilde{\theta}_{max}$ is the amplitude of the stick-slip vibration, $\Delta\tilde{\theta}_{max} = \Delta\theta_{max} - \Delta\theta_{eq}$. Then, the slip time T_{sl} can be calculated as

$$T_{sl} = \frac{2}{\omega_0}\arcsin\left(\frac{\Omega_0}{\Delta\dot{\theta}_{max}}\right) + \frac{\pi}{\omega_0},$$ (3.10)

and the stick time T_{st} can be expressed as

$$T_{st} = \frac{2N(\mu_s - \mu_d)r}{\Omega_0 k_\theta}. \tag{3.11}$$

As a result, the period of stick-slip motion is given as

$$T_p = \frac{2N(\mu_s - \mu_d)r}{\Omega_0 k_\theta} + \frac{2}{\omega_0}\arcsin\left(\frac{\Omega_0}{\Delta\dot{\theta}_{max}}\right) + \frac{\pi}{\omega_0}. \tag{3.12}$$

Therefore, some conclusions based on the simple model can be drawn as:

- A stick-slip limit cycle can be observed during the stick-slip motion;

- The period of the stick-slip motion is larger than the harmonic periods of the system without stick-slip;

- The period of the stick-slip motion increases with increasing normal force or decreasing motor speed;

- The amplitude of the stick-slip vibration increases with the normal force or the motor speed.

The aim of the remaining part of this section is to find out the existence conditions of stick-slip motions. In nonlinear dynamics, a limit cycle is an isolated periodic solution in a self-excited system [104]. Therefore, the existence of a stick-slip limit cycle can be judged by: if a system leaves the stick region and can return to the attractor of the stick region again under isolated environment, the system has a stable stick-slip motion. Since Eqs. (3.6) and (3.7) are the analytical solution of the piecewise differentiable Eqs. (3.4) and (3.5), substituting an initial condition in the stick region into Eq. (3.6) and (3.7), its solution, whether a stick-slip limit cycle or equilibrium solution, can be directly obtained.
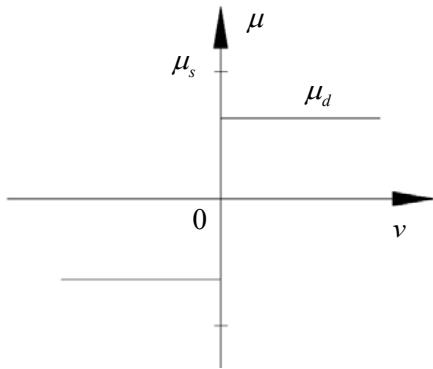
Fig. 3.3: Friction coefficient of Coulomb's friction law, where μ_s is assumed larger than μ_d, and μ_d is constant, v is the relative velocity
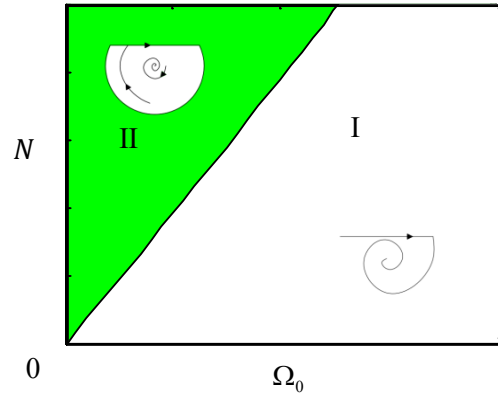
Fig. 3.4: Existence condition of the stick-slip motion, region I: without stick-slip limit cycle but with a stable equilibrium solution, region II: with stable stick-slip limit cycle and stable equilibrium solution

When the damping d_θ is larger than 0, the system has always a stable equilibrium solution in the slip region according to Lyapunov stability theory [104]. In contrast, the conditions for the existence of the stick-slip limit cycle depends on the parameters such as N and Ω_0. With varied parameters, the system

has two regions as sketched in the Fig. 3.4, i.e. a region with stable stick-slip limit cycle and equilibrium solution, named as region II; a region without the stick-slip limit cycle but with a stable equilibrium solution, named as region I. It should be noticed that in region II the system has two stable solutions so that the occurrence and absence of the stick-slip motion depends on its initial condition.

It is interesting to know under which initial conditions creep groan will occur in region II. There is a boundary between the attractors of the equilibrium solution and that of the limit cycle. In order to find this boundary, a critical point is defined as $\Delta\theta_{b,0} = \Delta\theta_e$, $\Delta\dot{\theta}_{b,0} = \Omega_0$ as shown in Fig. 3.5 marked with the red point. If a trajectory is lower than this critical point, this trajectory cannot reach the stick region anymore and goes to the equilibrium solution. Therefore, it is possible to find a trajectory which can just pass through the critical point, and this trajectory is nothing else but the boundary between two attractors. When the initial condition is outside the critical trajectory, the solution is the limit cycle solution. Otherwise, the resulting solution is the equilibrium solution.
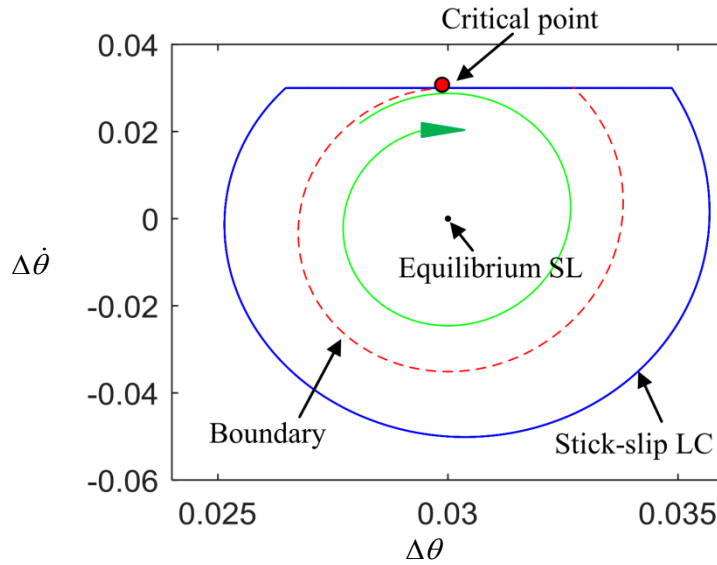
Fig. 3.5: The boundary between the attractors of the equilibrium solution and stick-slip limit cycle. The red point is the critical point defined as $\Delta\theta_{b,0} = \Delta\theta_e$, $\Delta\dot{\theta}_{b,0} = \Omega_0$. If a given trajectory is lower than this point, the system cannot reach the stick region (shown with green curve). The red dash line shows the boundary between the attractors.

In should be noticed that the system in the slip region has a linear behavior, and only a unique trajectory can pass through this critical point. As a result, it is possible to use negative time integration to calculate this trajectory based on the critical point (substituting $t_{neg} = -t\,t$ into Eq. (3.6)). The critical trajectory is calculated as

$$\Delta\theta_b = \exp\left(\frac{d_\theta}{2I}t_{neg}\right)\left(C_1\cos(-\omega_d t_{neg}) + C_2\sin(-\omega_d t_{neg})\right) + \Delta\theta_e, \tag{3.13}$$

$$\Delta\dot{\theta}_b = \exp\left(\frac{d_\theta}{2I}t_{neg}\right)\left(\left(\omega_d C_2 - \frac{d_\theta}{2I}C_1\right)\cos(-\omega_d t_{neg}) - \left(\omega_d C_1 - \frac{d_\theta}{2I}C_2\right)\sin(-\omega_d t_{neg})\right),$$

with

$$t_{\text{neg}} = -t, C_1 = 0, C_2 = \frac{\Omega_0}{\omega_d}, t_{\text{neg}} \in [0, t_{i+1}], \Delta\dot{\theta}_b\left(t_{i+1}\right) = \Omega_0,$$

where the calculated the critical trajectory is shown in Fig. 3.5 with the red dash line. This trajectory is the boundary between the attractors of the equilibrium solution and stick-slip limit cycle.

3.1.2   Two DOFs model with Coulomb's friction law

If both the vibrations of the disk and the pad are considered in the model, the test rig with an idealized brake can be treated as two sub-system coupled by the friction force. There are rotating parts i.e. disk-shaft sub-system, and non-rotating parts i.e. pad-carrier sub-system. Two pads are considered as one rigid body connecting to the base frame with a spring, since the two pads move simultaneously during creep groan. The disk is treated as a rigid body connecting to the motor with a torsional spring. If the system is in the slip region, the dynamics of the two sub-systems can be described as

$$I\Delta\ddot{\theta} + d_\theta\Delta\dot{\theta} + k_\theta\Delta\theta = Nr\mu_d \, \text{sgn}\left(\Omega_0 r - \Delta\dot{\theta}r - \dot{x}\right), \tag{3.14}$$

$$m\ddot{x} + d_x\dot{x} + k_x x = N\mu_d \, \text{sgn}\left(\Omega_0 r - \Delta\dot{\theta}r - \dot{x}\right),$$

where m is the mass of the pad; k_x and d_x are the stiffness and damping of the carrier; x is the displacement in vertical direction of the pad, the model is given in Fig. 3.6.
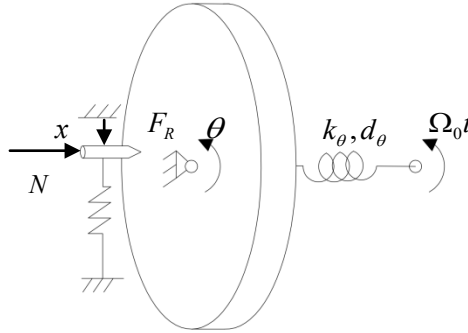
Fig. 3.6: Model of the test rig with an idealized brake with 2 DOFs

In contrast, the pad and disk are adhered with each other in the stick region, the dynamic equation is

$$\left(m + I/r^2\right)\ddot{x} + d_x\dot{x} + k_x x = -k_\theta\Delta\theta - d_\theta\Delta\dot{\theta}, \tag{3.15}$$

$$x = \Omega_0 rt - \Delta\theta r, \dot{x} = \Omega_0 r - \Delta\dot{\theta}r.$$

The system is in the stick region when the following conditions are fulfilled: The disk and pad have no relative motion; meanwhile the maximal static friction force is large enough to make the pad and disk to adhere,

$$\text{stick condition:} \dot{\theta}r - \dot{x} = 0 \cap N\mu_s \geq \left\|m\ddot{x} + d_x\dot{x} + k_x x\right\|. \tag{3.16}$$

Otherwise, the system is in the slip region.

The system is a piecewise linear system. It can be separately solved in each region. In the slip region, the motion of the shaft and the pad are

$$
\begin{cases}
\Delta\theta = \exp\left(-\dfrac{d_\theta}{2I}(t-t_{l0})\right)\left[C_1\cos\left(\omega_\theta(t-t_{l0})\right)+C_2\sin\left(\omega_\theta(t-t_{l0})\right)\right]+\Delta\theta_e \\
\Delta\dot{\theta} = \left[\left(\omega_\theta C_2 - \dfrac{d_\theta}{2I}C_1\right)\cos\left(\omega_\theta(t-t_{l0})\right)-\left(\omega_\theta C_1 - \dfrac{d_\theta}{2I}C_2\right)\sin\left(\omega_\theta(t-t_{l0})\right)\right]\exp\left(-\dfrac{d_\theta}{2I}(t-t_{l0})\right)
\end{cases}
\tag{3.17}
$$

$$
\begin{cases}
x = \exp\left(-\dfrac{d_x}{2m}(t-t_{l0})\right)\left[D_1\cos\left(\omega_x(t-t_{l0})\right)+D_2\sin\left(\omega_x(t-t_{l0})\right)\right]+x_d \\
\dot{x} = \left[\left(\omega_x D_2 - \dfrac{d_x}{2m}D_1\right)\cos\left(\omega_x(t-t_{l0})\right)-\left(\omega_x D_1 - \dfrac{d_x}{2m}D_2\right)\sin\left(\omega_x(t-t_{l0})\right)\right]\exp\left(-\dfrac{d_x}{2m}(t-t_{l0})\right)
\end{cases}
$$

where

$$
\omega_\theta = \sqrt{\dfrac{k_\theta}{I}-\left(\dfrac{d_\theta}{2I}\right)^2},\ \Delta\theta_e = Nr\mu_d/k_\theta,\ C_1 = \Delta\theta_{l0}-\Delta\theta_e,\ C_2 = \dfrac{1}{\omega_\theta}\left(\Delta\dot{\theta}_{l0}+\dfrac{d_\theta}{2I}C_1\right),
\tag{3.18}
$$

$$
\omega_x = \sqrt{\dfrac{k_x}{m}-\left(\dfrac{d_x}{2m}\right)^2},\ x_e = N\mu_d/k_x,\ D_1 = x_{l0}-x_e,\ D_2 = \dfrac{1}{\omega_x}\left(\dot{x}_{l0}+\dfrac{d_x}{2m}D_1\right),
$$

where t_{l0} is the time when the system just enters in the slip region, t is the current time, and $\Delta\theta_{l0}$, $\Delta\dot{\theta}_{l0}$ are the initial torsional angle and torsional velocity of the shaft at t_{l0}, x_{l0} and $\dot{x}_{l0}$ are the initial displacement and velocity of the pad at t_{l0}.

On the other hand, the solution in the stick region can be calculated by numerical integration

$$
\ddot{x}(t) = -\dfrac{1}{m+I/r^2}\left(-d_x\dot{x}-k_x x+k_\theta\Delta\theta+d_\theta\Delta\dot{\theta}\right),
\tag{3.19}
$$

$$
\dot{x}(t) = \int_{t_{l0}}^{t}\ddot{x}(\tau)d\tau+\dot{x}_{l0},\ x(t) = \int_{t_{l0}}^{t}\dot{x}(\tau)d\tau+x_{l0},
$$

$$
\Delta\dot{\theta} = \Omega_0 - \dot{x}/r,
$$

$$
\Delta\theta(t) = \int_{t_{l0}}^{t}\Delta\dot{\theta}(\tau)d\tau+\Delta\theta_{l0},
$$

where t_{l0} is the time when the system just enters in the stick region, t is the current time, and $\Delta\theta_{l0}$, x_{l0}, $\dot{x}_{l0}$ are the initial state variables at time t_{l0}.
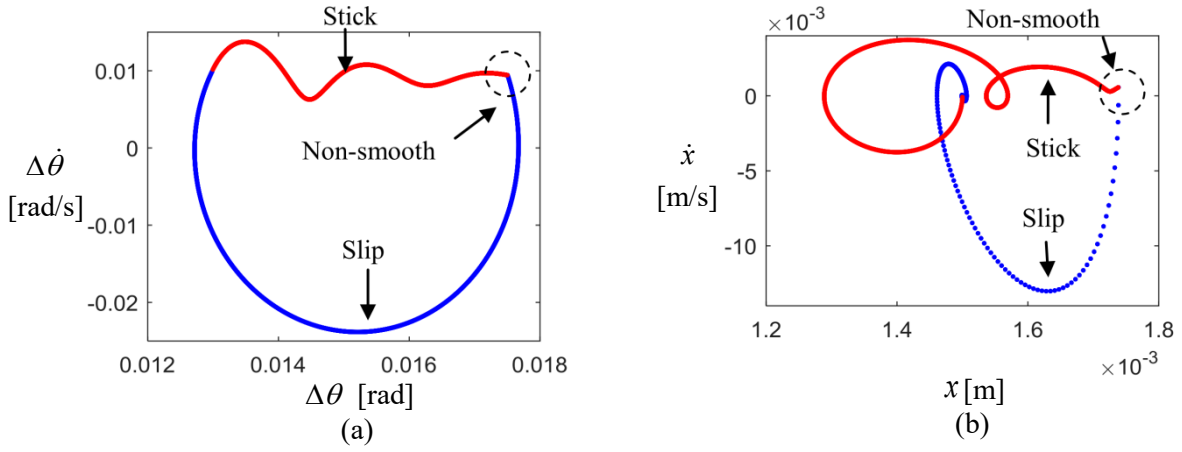
Fig. 3.7: Stick-slip limit cycle of the shaft (a) and the pad (b)
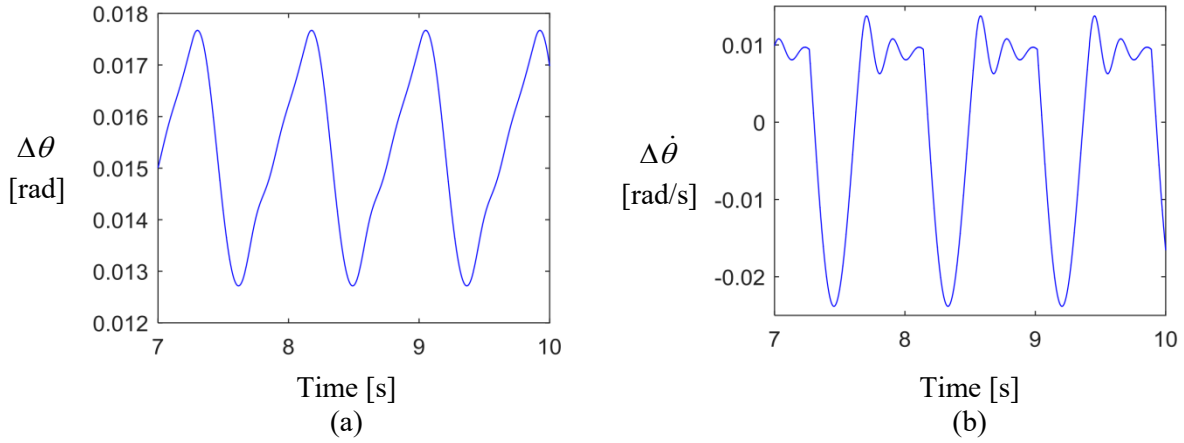
Fig. 3.8: Simulation torsional angle $\Delta\theta$ (a) and torsional velocity $\Delta\dot{\theta}$ (b) of the disk
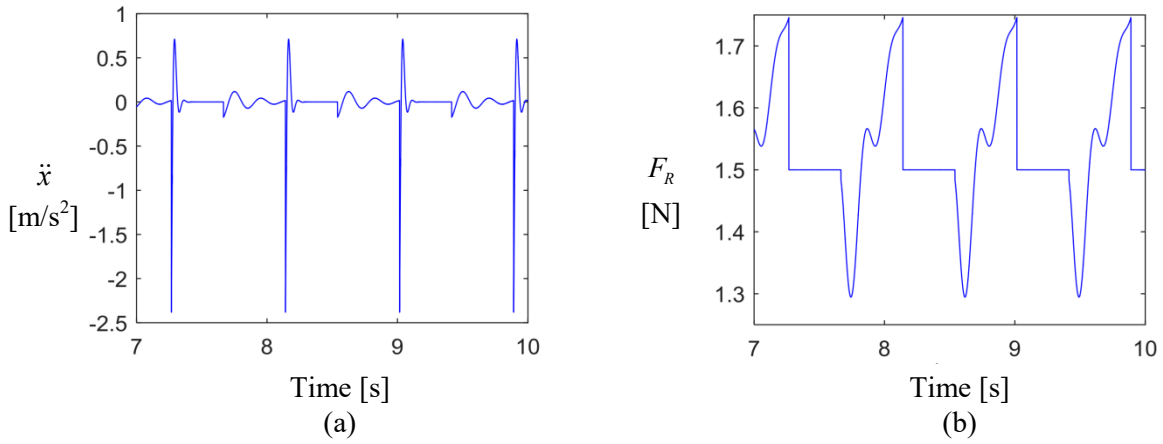
Fig. 3.9: Acceleration of the pad (a) and friction force (b)

Numerical simulation is carried out to study the stick-slip limit cycle of the system. The parameters of the system are arbitrarily chosen by the author and given in Table 3.1. A stick-slip limit cycle can be observed in the phase diagram $\Delta\dot{\theta}$ as a function of $\Delta\theta$, shown in Fig. 3.7. In order to differ the stick region from the slip region, the red line denotes the stick region and blue line denotes the slip region. One can see that there are non-smooth regions between the stick motion and slip motion in the simulation results [103], [104]. The simulated torsional angle $\Delta\theta$ and torsional velocity $\Delta\dot{\theta}$ are exhibited in

Fig. 3.8. The simulated acceleration of the pad $\ddot{x}$ and friction force F_R are shown in Fig. 3.9. The advantages of the model with Coulomb's friction law are that the stick and slip regions can be separated clearly, and the stick and slip motion can be analyzed separately. The disadvantage is that the non-smooth problem appears between the stick and slip regions. The non-smooth nature of Coulomb's model makes the difficulty of the numerical integration. Therefore, instead of Coulomb's friction law, the bristle friction law will be studied in the later section to improve the simulation results.

Parameters	Values	Parameters	Values
I	1kgm^2	m	0.1kg
k_θ	100 Nm	k_x	1000 N/m
d_θ	1 Nms	d_x	10 Ns/m
μ_s	0.3	r	1 m
μ_d	0.35	N	5 N
Ω_0	0.01 rad/s		

Table 3.1: Parameters of the system

If the damping of the drive shaft is increased to 0.4 Nms and the damping of the carrier is decreased to 0.01 Ns/m, different things will happen as shown in Fig. 3.10. Fig. 3.10 (a) shows the friction force and (b) shows the stick-slip limit cycle of the pad. It is noticed that the stick-slip limit cycle is related to the damping of the system. If the damping of the shaft is low, a stick-slip limit cycle is observed in the disk-shaft sub-system. In contrast, if the damping of the carrier is low, the stick-slip limit cycle is obtained in the pad-carrier sub-system.
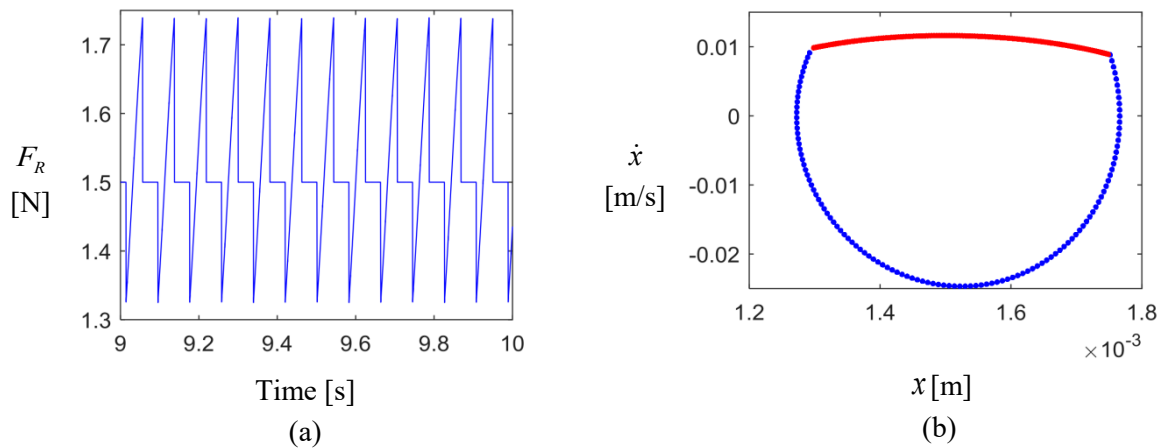

Fig. 3.10: Friction force (a), stick-slip limit cycle of the pad (b) with $d_\theta = 0.4$ Nms, $d_x = 0.01$ Ns/m

3.2   Minimal model with the bristle friction law

Even though the model with Coulomb's friction law can help us to understand the mechanism of the stick-slip motion, it is too simple to explain several effects of creep groan in a brake system. In order to make our simulation close to the experimental results, the bristle friction law is chosen for modeling creep groan in this section [67]-[70].
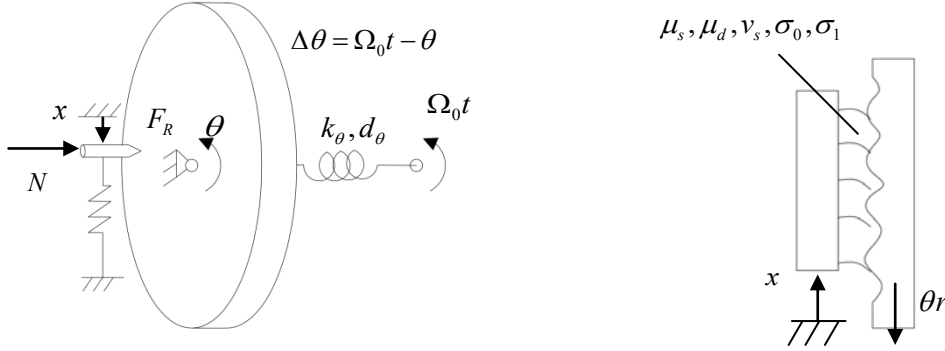
Fig. 3.11: Model of the brake test rig with an idealized brake with the bristle friction law

3.2.1   One DOF model with the bristle friction law

The model of the test rig is given in Fig. 3.11. The disk is considered as a rigid body and connected with the motor by the drive shaft, while the drive shaft is considered as a rotational spring. This model and corresponding simulation results compared with the experimental results have been published in [32]. At first, only the vibration of the disk is considered in the model. The equation of motion of the one degree of freedom system is described by

$$I\Delta\ddot{\theta} + d_\theta\Delta\dot{\theta} + k_\theta\Delta\theta = F_R r, \tag{3.20}$$

where I is the moment of inertia of the disk; r is the radius of the point where the pad acts; k_θ and d_θ are the stiffness and damping of the drive shaft; $\Delta\theta$ is the torsional angle of the drive shaft superposed to the disk rotation with angle θ, $\Delta\theta$ is equal to $\Omega_0 t - \theta$, Ω_0 is the rotating speed of motor, and F_R is the friction force in the contact between the disk and pad.

The bristle friction law, which is proposed by Canudas de Wit *et al.* [67]-[70], is used to calculate F_R. This theory is based on the imagination that two rigid bodies are in contact through visco-elastic bristle surfaces. When a tangential force is applied, the bristles will deflect like springs which give rise to the friction force. If the force is sufficiently large to make some of the bristles deflect then slip occurs. The dynamic friction force can be expressed as

$$F_R = \sigma_0 z + \sigma_1 \dot{z}, \tag{3.21}$$

where z is the average deflection of the bristles, σ_0 is their stiffness, σ_1 is their damping, and $\dot{z}$ is a nonlinear function of $\Delta\dot{\theta}$ and z

$$\dot{z} = \phi(\Delta\dot{\theta}, z) = \Omega_0 r - \Delta\dot{\theta}r - \frac{z}{g_0}|\Omega_0 r - \Delta\dot{\theta}r|. \tag{3.22}$$

Here g_0 is given as

$$g_0 = \frac{1}{\sigma_0}\left(N\mu_d + N(\mu_s - \mu_d)\exp\left(-\left|\frac{(\Omega_0 - \Delta\dot{\theta})r}{v_s}\right|^{\alpha}\right)\right), \tag{3.23}$$

where v_s is the Stribeck velocity, N is the brake normal force, μ_s is the static friction coefficient, μ_d is the dynamic friction coefficient, α is an empirical parameter which can be measured in experiments. The value $\alpha = 1$ is suggested for the dry contact while $\alpha = 2$ is preferred for the lubrication contact [105]. The friction coefficients for $\alpha = 1$ and $\alpha = 2$ are given in Fig. 3.12.
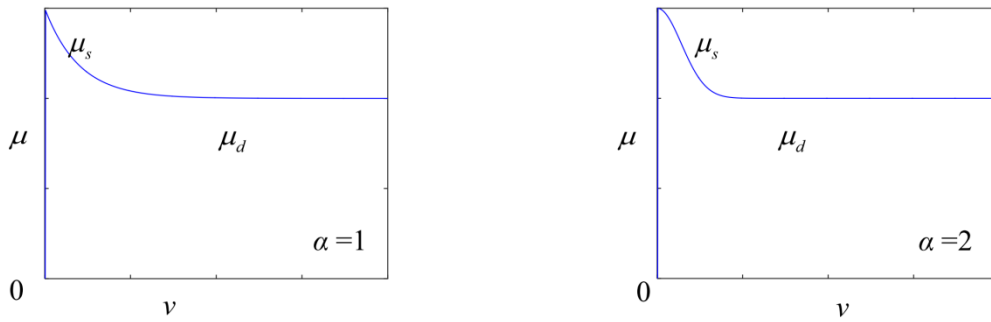
Fig. 3.12: Friction coefficient of $\alpha = 1$ and $\alpha = 2$, v is the relative velocity

This bristle friction law can describe pre-sliding and hysteresis characteristics of friction. The complete dynamic equations can be written as a set of first order differential equations

$$\dot{\boldsymbol{Y}} = \begin{bmatrix} \Delta\dot{\theta} \\ -\frac{d_\theta}{I}\Delta\dot{\theta} - \frac{k_\theta}{I}\Delta\theta + \frac{r}{I}\sigma_0 z + \frac{r}{I}\sigma_1\phi(\Delta\dot{\theta}, z) \\ \phi(\Delta\dot{\theta}, z) \end{bmatrix}, \tag{3.24}$$

$$\boldsymbol{Y} = \begin{bmatrix} \Delta\theta & \Delta\dot{\theta} & z \end{bmatrix}^{\mathrm{T}}, \phi(\Delta\dot{\theta}, z) = \Omega_0 r - \Delta\dot{\theta}r - \frac{z}{g_0}|\Omega_0 r - \Delta\dot{\theta}r|,$$

where $\boldsymbol{Y}$ is the vector of state variables of the system. The equilibrium solution of Eq. (3.24) is expressed as

$$\dot{\boldsymbol{Y}}_{eq} = 0, \boldsymbol{Y}_{eq} = \begin{bmatrix} \Delta\theta_{eq} & 0 & z_{eq} \end{bmatrix}^{\mathrm{T}},$$

$$\Delta\theta_{eq} = r\left(N\mu_d + N(\mu_s - \mu_d)\exp\left(-\left|\frac{\Omega_0 r}{v_s}\right|^{\alpha}\right)\right)/k_\theta, z_{eq} = \left(N\mu_d + N(\mu_s - \mu_d)\exp\left(-\left|\frac{\Omega_0 r}{v_s}\right|^{\alpha}\right)\right)/\sigma_0.$$

Linearizing Eq. (3.24) about its equilibrium position

$$\dot{Y} = AY, \tag{3.25}$$

$$A = \begin{bmatrix} 0 & 1 & 0 \\ -\dfrac{k_\theta}{I} & -\dfrac{d_\theta}{I} + \dfrac{r\sigma_1}{I}\dfrac{\partial\phi(\Delta\dot\theta,z)}{\partial\Delta\dot\theta} & \dfrac{r\sigma_0}{I} + \dfrac{r\sigma_1}{I}\dfrac{\partial\phi(\Delta\dot\theta,z)}{\partial z} \\ 0 & \dfrac{\partial\phi(\Delta\dot\theta,z)}{\partial\Delta\dot\theta} & \dfrac{\partial\phi(\Delta\dot\theta,z)}{\partial z} \end{bmatrix}.$$

In the case of $\alpha = 1$

$$\frac{\partial\phi(\Delta\dot\theta,z)}{\partial\Delta\dot\theta} = \frac{(\mu_s - \mu_d)r^2\Omega_0}{v_s(\mu_s - \mu_d + \mu_d\exp(\Omega_0 r/v_s))},$$

$$\frac{\partial\phi(\Delta\dot\theta,z)}{\partial z} = \frac{-r\sigma_0\Omega_0}{N\mu_d + N(\mu_s - \mu_d)\exp(-\Omega_0 r/v_s)},$$

and in the case of $\alpha = 2$

$$\frac{\partial\phi(\Delta\dot\theta,z)}{\partial\Delta\dot\theta} = \frac{2(\mu_s - \mu_d)r^3\Omega_0^2}{v_s^2(\mu_s - \mu_d + \mu_d\exp(r^2\Omega_0^2/v_s^2))},$$

$$\frac{\partial\phi(\Delta\dot\theta,z)}{\partial z} = \frac{-r\sigma_0\Omega_0}{N\mu_d + N(\mu_s - \mu_d)\exp(-r^2\Omega_0^2/v_s^2)},$$

where A is the corresponding system matrix. The stability of the equilibrium solution can be obtained by analyzing the eigenvalues of A. If the real parts of all eigenvalues are negative, the equilibrium solution is asymptotically stable. If any of the real parts of eigenvalues is positive, the equilibrium solution is unstable, and the solution will show increasing amplitudes. On the other hand, the limit cycle of Eq. (3.24) can be determined by transient analysis using numerical integration.
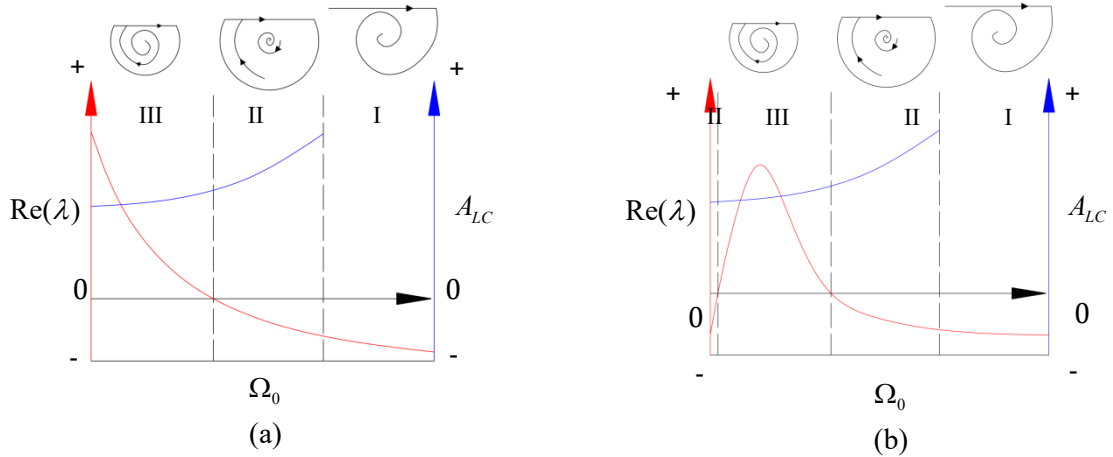
Fig. 3.13: Three regions and the possible phase plots with variation of driving speed (a) $\alpha =1$, (b) $\alpha = 2$, the red line is the maximum real part of eigenvalues of the equilibrium solution, and the blue line gives the amplitude of the stick-slip limit cycle.

In the following, possible parameter regions of solutions of the system are discussed qualitatively. According to the existence conditions of the stick-slip limit cycle and the stability of the equilibrium solution, the system shows three different regions with different types of solutions. When the system

31

has no stick-slip limit cycle and has a stable equilibrium solution, creep groan cannot occur in this parameter region which is labeled as region I. When the system has a stable stick-slip limit cycle and stable equilibrium solution (and an unstable limit cycle solution in between), the system may have creep groan or not, which depends on its initial conditions. This region is labeled as region II. When the system has a stable stick-slip limit cycle and an unstable equilibrium solution, creep groan will always occur and this region is labeled as region III. Fig. 3.13 exhibits the three regions qualitatively and the possible phase plots with the variation of the motor speed, where the red line is the maximum real part of eigenvalues of the equilibrium solution, and the blue line gives the amplitude of the stick-slip limit cycle. With the increase of driving speed, the system for $\alpha = 1$ goes through region III, II and I, respectively, while the system for $\alpha = 2$ goes through region II, III, II and I, respectively.

If the driving speed and brake pressure are both varied, the three parameter regions I-III are qualitatively sketched in Fig. 3.14. The distribution of parameter regions are named as map of creep groan, since it can show the condition of generating creep groan. The boundary between regions II and III is defined as a curve, where the largest real part of the eigenvalues of the system matrix A is equal to 0. The way to determine the boundary between regions I and II is given as follows: For varying brake pressure and speed, the solution of the nonlinear system can be calculated by a numerical time integration of Eq. (3.24) with initial conditions in the stick region. If the solution is still the stick-slip limit cycle after a while, the stick-slip limit cycle is considered to exist and be stable. In addition, its equilibrium solution is asymptotically stable and the system is in region II. If the solution converges to the equilibrium solution, a stable stick-slip limit cycle is considered not to exist, i.e. the system is in region I. By varying the brake pressure and driving speed, the regions I and II, as well as the boundary between them can be determined.

(a)

(b)
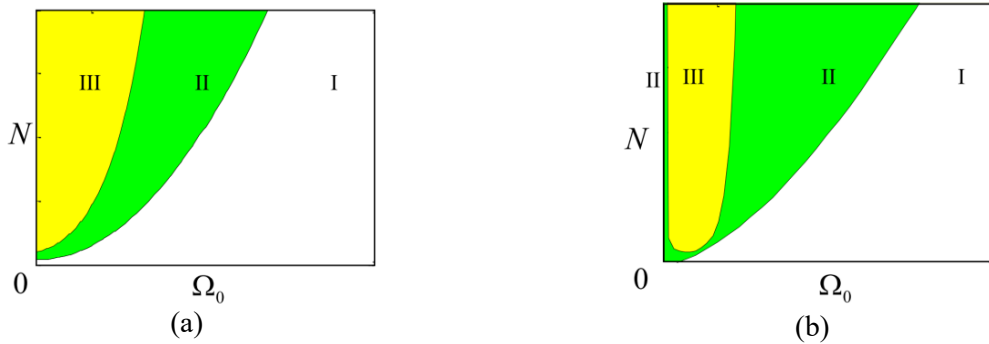
Fig. 3.14: Map of creep groan, (a) $\alpha = 1$, (b) $\alpha = 2$, region I: the system has no stick-slip limit cycle and has a stable equilibrium solution; region II: the system has a stable stick-slip limit cycle and stable equilibrium solution; region III: the system has a stable stick-slip limit cycle and an unstable equilibrium solution

There are some differences between the cases $\alpha = 1$ and $\alpha = 2$. For the case $\alpha = 2$, the system is under region II with very low velocity, which is not the case when $\alpha = 1$. This difference is shown in Fig. 3.14. The stable equilibrium solution and the stick-slip limit cycle solution in regions I to III are sketched in Fig. 3.15 for $\alpha = 1$ and in Fig. 3.16 for $\alpha = 2$. Simulation results prove that the stable equilibrium solution and the stick-slip limit cycle solution exist simultaneously in region II. In region I, even though the initial condition is in the stick region, the system returns the equilibrium solution after finite time. In region III, even though the initial condition is in the equilibrium solution, the amplitude of the system increases until it reaches the stick-slip limit cycle. The limit cycles are similar with each

other in the cases of $\alpha = 1$ and $\alpha = 2$. According to the experimental results shown in the chapter 5, $\alpha = 1$ is a more reasonable choice for our test rig. For the later modeling, only $\alpha = 1$ is considered.

The map of creep groan indicates the necessary conditions for generating creep groan, which can be used to evaluate the brake system with respect to creep groan. If the area of regions II and III is large, the brake system has a high probability to show creep groan, and vice versa.

Compared to the system with Coulomb's friction law, the system using the bristle friction law has an additional region, i.e. region III. Besides, since the pre-sliding effect includes in the bristle friction law, there is no sudden change between the stick region and slip region anymore.
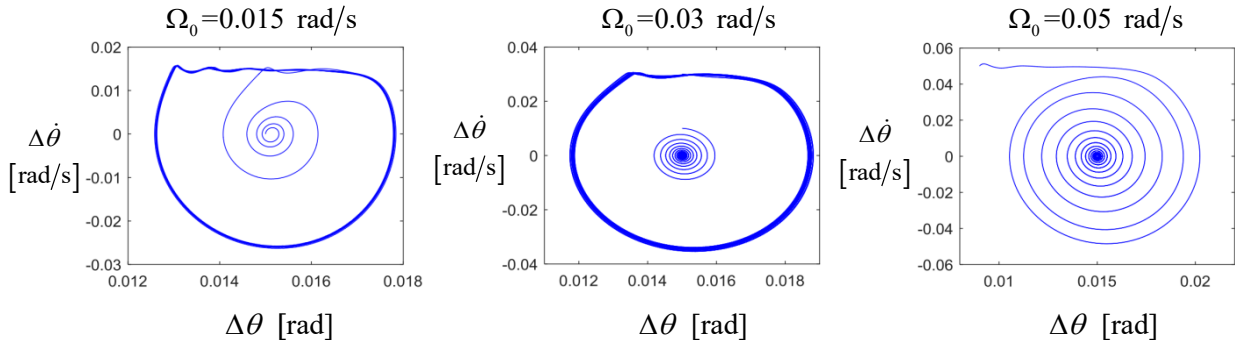
Fig. 3.15: Equilibrium solution and the stick-slip limit cycle solution $\alpha = 1$
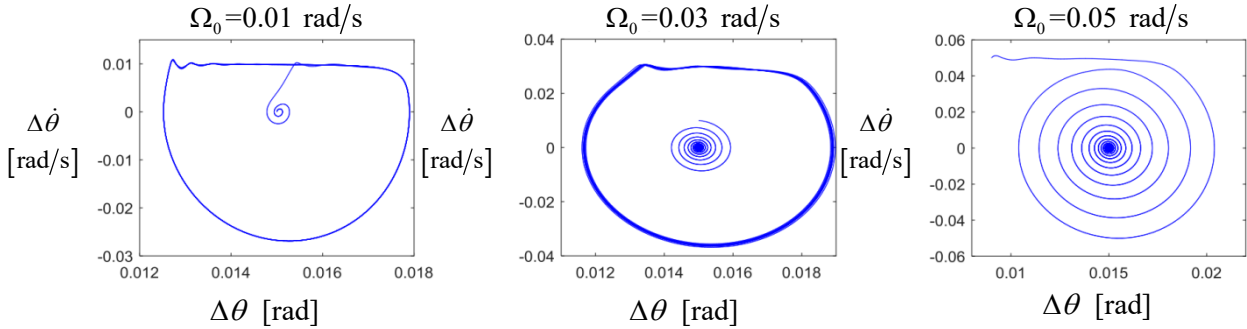
Fig. 3.16: Equilibrium solution and the stick-slip limit cycle solution $\alpha = 2$

In the following part of this section, the bifurcation behavior of the system will be studied. Fig. 3.14 already shows the bifurcation behavior, and its property will be further studied by analytical method in this part. In order to simplify the analysis, it is assumed that σ_0 is approximate to infinite and $\dot{z}$ is approximate to 0, Eqs. (3.20)-(3.23) can be written as in slip region and stick region separately. In the slip region, the dynamic equation is given as

$$I\Delta\ddot{\theta}_b + d_\theta\Delta\dot{\theta}_b + k_\theta\Delta\theta_b = r\left(N\mu_d + N\Delta\mu\exp\left(-\frac{(\Omega_0 - \Delta\dot{\theta})r}{v_s}\right)\right),$$ (3.26)

with $\Delta\mu = \mu_s - \mu_d$.

In the stick region, the disk will stick with the pad and the friction force between $\left[-N\mu_s, +N\mu_s\right]$ will balance the force of the torsional spring.

At first, the analytical study is given in the slip region. A similar case has been studied by Hetzler *et al.* in [95] with the same method. By introducing the coordinate transformation

$$\Delta\theta = \Delta\tilde{\theta} + \frac{1}{k_\theta} rN\left(\mu_d + \Delta\mu\exp\left(-\Omega_0 r / v_s\right)\right)$$

$$\Delta\ddot{\tilde{\theta}} + \frac{d_\theta}{I}\Delta\dot{\tilde{\theta}} + \frac{k_\theta}{I}\Delta\tilde{\theta} = \frac{rN\Delta\mu}{I}\exp\left(-\frac{(\Omega_0 - \Delta\dot{\tilde{\theta}})r}{v_s}\right) - \frac{rN\Delta\mu}{I}\exp\left(-\frac{\Omega_0 r}{v_s}\right). \tag{3.27}$$

Rewriting Eq. (3.27) into

$$\Delta\ddot{\tilde{\theta}} + \omega_0^2\Delta\tilde{\theta} = -2D\omega_0\Delta\dot{\tilde{\theta}} + \gamma\exp\left(\beta\Delta\dot{\tilde{\theta}}\right) - \gamma, \tag{3.28}$$

with

$$\omega_0^2 = \frac{k_\theta}{I}, D = \frac{d_\theta}{2I\omega_0}, \gamma = \frac{rN\Delta\mu}{I}\exp\left(-\frac{\Omega_0 r}{v_s}\right), \beta = \frac{r}{v_s}.$$

Then, with the assumptions $D\omega_0^2 \ll 1$ and $\gamma \ll 1$, the state variables can be described by sine or cosine functions approximately

$$\Delta\tilde{\theta} = A\sin\varphi = AS(\varphi) \tag{3.29}$$
$$\Delta\dot{\tilde{\theta}} = A\omega_0\cos\varphi = \omega_0 AC(\varphi)$$
$$\Delta\ddot{\tilde{\theta}} = -A\omega_0^2\sin\varphi = -\omega_0^2 AS(\varphi)$$

where S denotes sine function and C denotes cosine function. Eq. (3.29) can be interpreted as the transformation to polar coordinate from state space. Substituting Eq. (3.29) into Eq. (3.28)

$$\Delta\ddot{\tilde{\theta}} + \omega_0^2\Delta\tilde{\theta} = -2D\omega_0^2 AC(\varphi) + \gamma\exp\left(\beta\omega_0 AC(\varphi)\right) - \gamma. \tag{3.30}$$

The right-hand side of the equation can be written as

$$f = -2D\omega_0^2 AC(\varphi) + \gamma\exp\left(\beta\omega_0 AC(\varphi)\right) - \gamma. \tag{3.31}$$

According to the slowly changed amplitude and phase method [104], the amplitude is obtained by averaging f over one period

$$A' = \frac{1}{2\pi}\int_0^{2\pi} f\cos\varphi d\varphi \tag{3.32}$$
$$= -\frac{1}{\pi}D\omega_0^2 A\langle C^2\rangle + \gamma\left[\langle\exp\left(\beta\omega_0 AC(\varphi)\right)\rangle - \langle C\rangle\right],$$

where $\langle.\rangle$ denotes the average of a function over one period. In order to calculate A', Eq. (3.32) is rewritten as a series representation of the exponential functions, yielding

$$A' = -\frac{1}{\pi} D\omega_0^2 A \langle C^2 \rangle + \frac{\gamma}{2\pi} \left[\int_0^{2\pi} \sum_{n=1}^{\infty} \frac{\beta^n \omega_0^n A^n C^n}{n!} C d\varphi - 2\pi \langle C \rangle \right] \tag{3.33}$$

$$= -D\omega_0^2 A + \gamma \sum_{k=1}^{\infty} \frac{\beta^{2k-1} \omega_0^{2k-1}}{(2k-1)!} \frac{\langle C^{2k} \rangle}{2\pi} A^{2k-1}.$$

As a result, a constant A can be calculated with $A'=0$

$$-D\omega_0^2 A + \gamma \sum_{k=1}^{\infty} \frac{\beta^{2k-1} \omega_0^{2k-1}}{(2k-1)!} \frac{\langle C^{2k} \rangle}{2\pi} A^{2k-1} = 0. \tag{3.34}$$

It is obvious that $A = 0$ is one of the solutions in the system, which is the equilibrium solution. Another approximate solution, which is the limit cycle solution, has been calculated by Hetzler *et al.* in [95] by chosen k as 1 and 2 (3rd order approximation). Here, it is possible to get a better approximate result with high orders approximation

$$-D\omega_0^2 A + \gamma \frac{\beta \, \omega_0 \langle C^2 \rangle}{2\pi} A + \gamma \frac{\beta^3 \omega_0^3 \langle C^4 \rangle}{12\pi} A^3 + \gamma \frac{\beta^5 \omega_0^5 \langle C^6 \rangle}{240\pi} A^5 + ... + \gamma \frac{\beta^{2k-1} \omega_0^{2k-1}}{(2k-1)!} \frac{\langle C^{2k} \rangle}{2\pi} A^{2k-1} = 0. \tag{3.35}$$

In order to distinguish the stick-slip limit cycle, the no zero solution of Eq. (3.35) is called slip limit cycle, since it occurs in slip region. Hetzler *et al.* [95] provided that this solution is an unstable limit cycle.

If stick-slip occurs in the system, by assuming the system with low damping, the amplitude to the stick-slip limit cycle can be calculated as

$$\Delta \tilde{\theta}_{max} = \sqrt{\frac{I\Omega_0^2}{k_\theta} + \left(N(\mu_s - \mu_d)r - d_\theta \Omega_0 \right)^2}. \tag{3.36}$$

Fig. 3.17 shows the equilibrium solution, stick-slip limit cycle and slip limit cycle with different order approximation. In this figure, regions I, II and III are calculated by numerical integration. The boundary between regions II and III is coincided with the Hopf-bifurcation. With increasing of the speed, the amplitude of stick-slip limit cycle will go across that of the slip limit cycle. By increasing the order of approximation, the cross point will be approximate to the boundary between regions II and I. Therefore, it is possible to use this cross point to determine the boundary between regions II and I.

In region II, the slip limit cycle is nothing else than the boundary between the attractors of the stick-slip limit cycle and the equilibrium solution, shown in Fig. 3.18 (a). When the initial condition lies inside of the slip limit cycle, the system goes to an equilibrium solution. When the initial condition lies outside the slip limit cycle, the amplitude of the system will increase until it reaches the stick region [95].
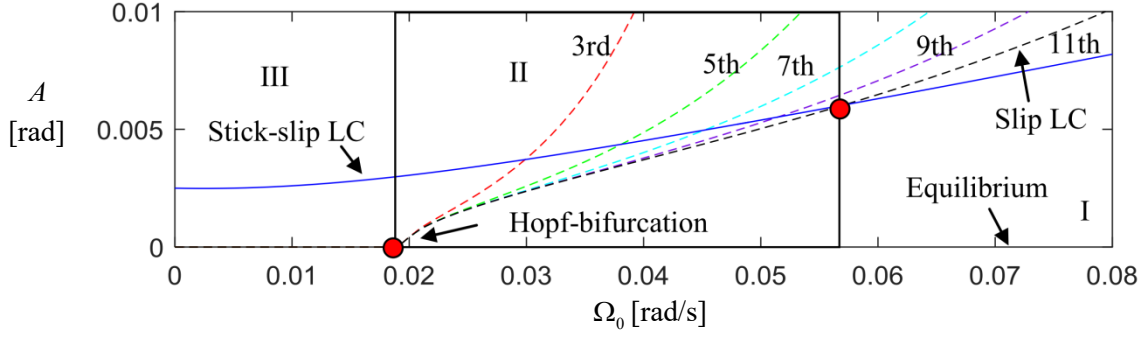
Fig. 3.17: Amplitude of stick-slip limit cycle and slip limit cycle with 3rd, 5th, 7th, 9th and 11th order approximation, the red points are the boundaries between regions I, II and III calculated by the numerical integration
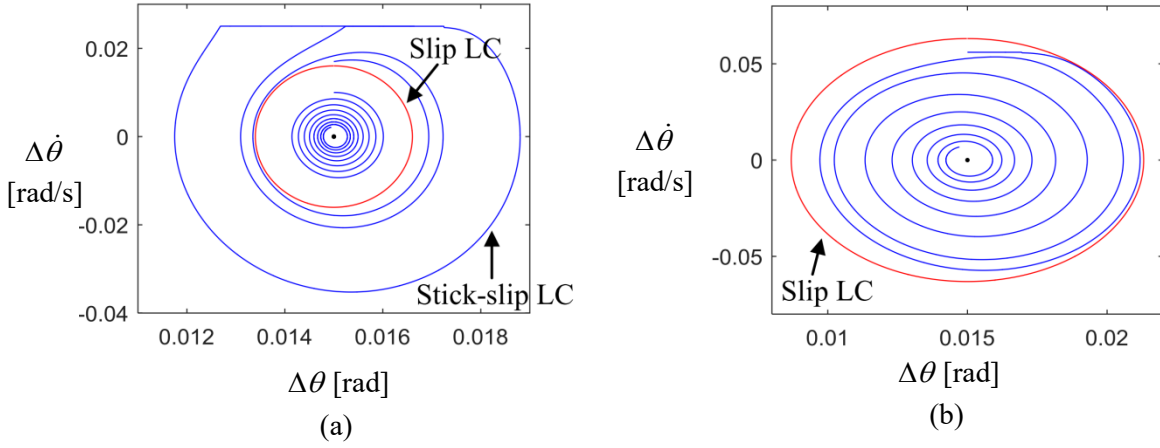

(a)

(b)

Fig. 3.18: (a) Equilibrium solution, slip limit cycle solution and stick-slip limit cycle solution in region II. (b) The system has no stick-slip limit cycle when the amplitude of slip limit cycle is larger than that of the stick-slip limit cycle.

At a critical speed, the amplitude of stick-slip limit cycle and that of the slip limit cycle go across with each other. It is interesting to know the physical meaning of this cross point. When the stick-slip limit cycle is larger than the slip limit cycle, the system will always have stick-slip motion if the initial condition is given in the stick region. Therefore, the stick-slip limit cycle larger than the slip limit cycle is a condition that a system has a stick-slip limit cycle. Fig. 3.18 (b) shows that the stick-slip will not happen when the amplitude of the slip limit cycle is larger than that of the stick-slip limit cycle. Therefore, it is possible to use this cross point to approximate the boundary between regions I and II.

If the order of approximation is chosen as 5, the amplitude of the slip limit cycle can be calculated through Eq. (3.35)

$$
A = \sqrt{\dfrac{-\dfrac{\beta^3 \omega_0^3 \gamma}{16} + \sqrt{\dfrac{\beta^6 \omega_0^6 \gamma^2}{256} - 4 \dfrac{\beta^5 \omega_0^5 \gamma}{384}\left(\dfrac{\beta \; \omega_0 \gamma}{2} - D\omega_0^2\right)}}{\dfrac{\beta^5 \omega_0^5 \gamma}{192}}}.
$$

(3.37)

36

Making the amplitude of the slip limit cycle to be equal to that of the stick-slip limit cycle, i.e. substituting Eq. (3.36) into Eq. (3.37), it is obtained that

$$\left(\frac{I\Omega_0^2}{k_\theta}+\frac{\left(N(\mu_s-\mu_d)r-d_\theta\Omega_0\right)^2}{k_\theta^2}\right)\frac{\beta^5\omega_0^5\gamma}{192}=-\frac{\beta^3\omega_0^3\gamma}{16}+\sqrt{\frac{\beta^6\omega_0^6\gamma^2}{256}-4\frac{\beta^5\omega_0^5\gamma}{384}\left(\frac{\beta\;\omega_0\gamma}{2}-D\omega_0^2\right)}.$$ (3.38)

By solving this equation, the boundary between regions I and II can be approximately solved. The map of creep groan obtained with analytical method is given in Fig. 3.19 (a). On the other hand, the map can also be solved by numerical integration as shown in Fig. 3.19 (b). The error between the analytical and the numerical maps increases with the brake force. In the following parts of this thesis, all maps are obtained through numerical analysis to guarantee the accuracy.
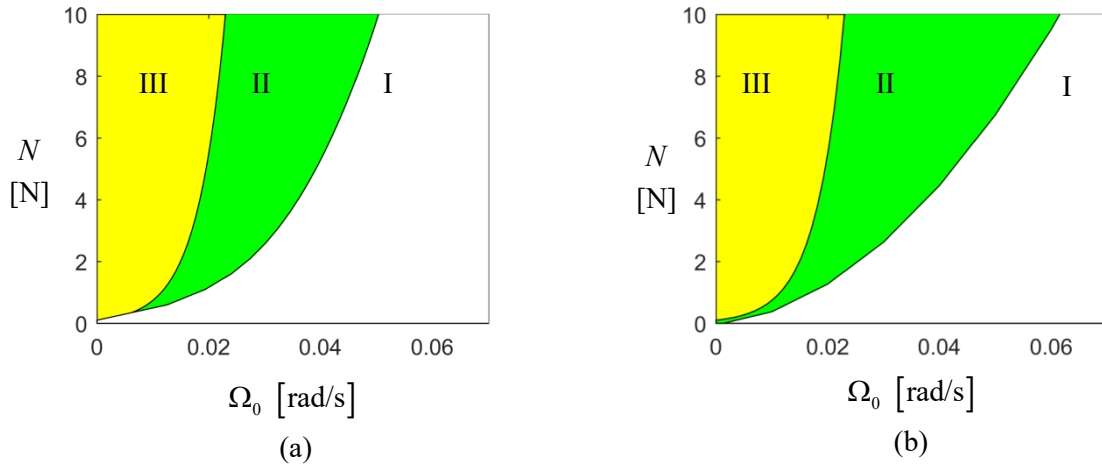
Fig. 3.19: Map of creep groan calculated by the analytical method (a), and the numerical method (b)

3.2.2 Two DOFs model with the bristle friction law

In order to study the noise generation of creep groan, the vibration of the pad should also be considered. The brake system consists of rotating parts i.e. disk-shaft sub-system and non-rotating parts i.e. pad-carrier sub-system. This model and corresponding simulation results compared with the experimental results are also described in [33]. The dynamics of the two sub-systems can be described by

$$I\Delta\ddot{\theta}+d_\theta\Delta\dot{\theta}+k_\theta\Delta\theta=F_Rr,$$ (3.39)
$$m\ddot{x}+d_x\dot{x}+k_xx=F_R.$$

where m is the mass of the pad; k_x and d_x are the stiffness and damping of the carrier; x is the displacement in vertical direction of the pad.

Suppose that two rigid bodies are in contact with the elastic bristle surfaces [67] and the friction force F_R is generated by the deformation of the bristle. The dynamic friction force F_R can in general be expressed as

$$F_R=\sigma_0z+\sigma_1\dot{z},$$ (3.40)

and $\dot{z}$ is a nonlinear function of $\Delta\dot{\theta}$, x and z

$$\dot{z} = \phi(\Delta\dot{\theta}, \dot{y}, z) = \Omega_0 r - \Delta\dot{\theta} r - \dot{x} - \frac{z}{g_0}|\Omega_0 r - \Delta\dot{\theta} r - \dot{x}|, \tag{3.41}$$

where g_0 is a scale which includes the Stribeck effect. Here g_0 is given as

$$g_0 = \frac{1}{\sigma_0}\left(N\mu_d + N(\mu_s - \mu_d)\exp\left(-\left|\frac{(\Omega_0 - \Delta\dot{\theta})r - \dot{x}}{v_s}\right|\right)\right). \tag{3.42}$$

The complete dynamic equations can be written as a set of first order differential equations

$$\dot{Y} = \begin{bmatrix} \Delta\dot{\theta} \\ \dot{x} \\ -\dfrac{d_\theta}{I}\Delta\dot{\theta} - \dfrac{k_\theta}{I}\Delta\theta + \dfrac{r}{I}\sigma_0 z + \dfrac{r}{I}\sigma_1\phi(\Delta\dot{\theta}, \dot{x}, z) \\ -\dfrac{d_x}{m}\dot{x} - \dfrac{k_x}{m}x + \dfrac{1}{m}\sigma_0 z + \dfrac{1}{m}\sigma_1\phi(\Delta\dot{\theta}, \dot{x}, z) \\ \phi(\Delta\dot{\theta}, \dot{x}, z) \end{bmatrix}, \tag{3.43}$$

$$Y = \begin{bmatrix} \Delta\theta & x & \Delta\dot{\theta} & \dot{x} & z \end{bmatrix}^{\mathrm{T}},$$

$$\phi(\Delta\dot{\theta}, \dot{x}, z) = \Omega_0 r - \Delta\dot{\theta} r - \dot{x} - \frac{z}{g_0}|\Omega_0 r - \Delta\dot{\theta} r - \dot{x}|,$$

where Y is the vector of state variables of the system.

Numerical simulation is carried out to study the stick-slip limit cycle of the system. The system parameters are arbitrarily chosen by the author and given in Table 3.2. A stick-slip limit cycle can be observed in the torsional angle in Fig. 3.20. This limit cycle is qualitatively similar to the limit cycle shown in Fig. 3.10 but without non-smooth part, so that it can describe the experimental results better. The pre-sliding effect between the stick region and slip region can be observed in the simulated result. The simulated torsional angle and torsional velocity are exhibited in Fig. 3.21. Besides, the acceleration of the pad and the friction force are shown in Fig. 3.22. In the stick region, the friction force increases linearly, while in the slip region the friction force is almost constant.

Parameters	Values	Parameters	Values
I	$1\,\mathrm{kgm}^2$	m	0.1kg
k_θ	100 Nm	k_x	1000 N/m
d_θ	1 Nms	d_x	10 Ns/m
μ_s	0.3	v_s	0.005 m/s
μ_d	0.35	σ_0	50000 N/m
r	1 m	σ_1	100 Ns/m
N	5 N	Ω_0	0.01 rad/s

Table 3.2: Parameters of the system
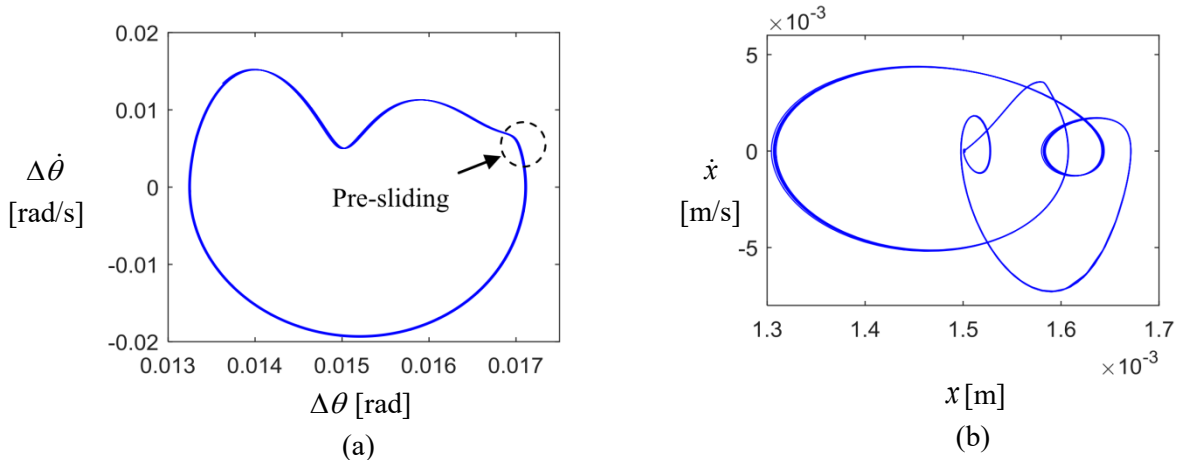
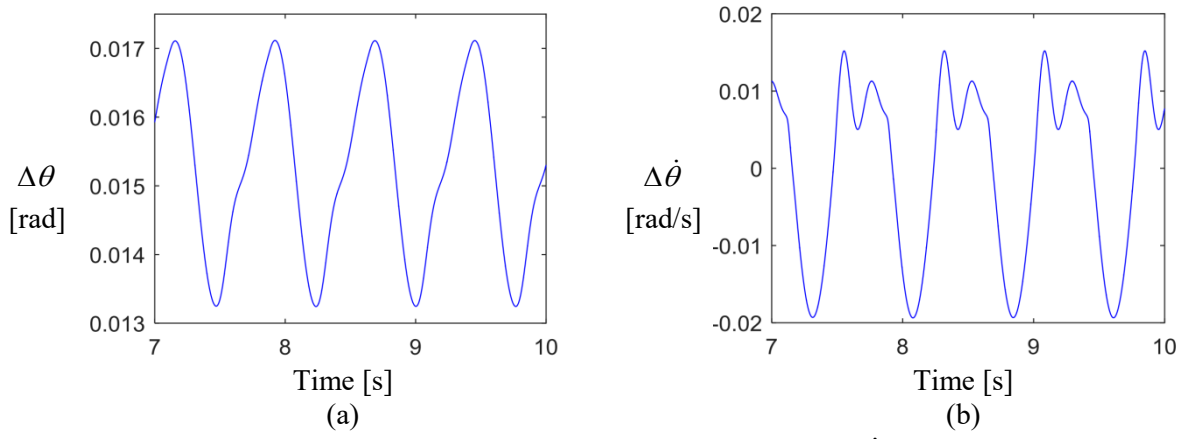Fig. 3.20: Limit cycle of the drive shaft (a), and the pad (b)

Fig. 3.21: Torsional angle $\Delta\theta$ (a) and torsional velocity of the shaft $\Delta\dot\theta$ (b)
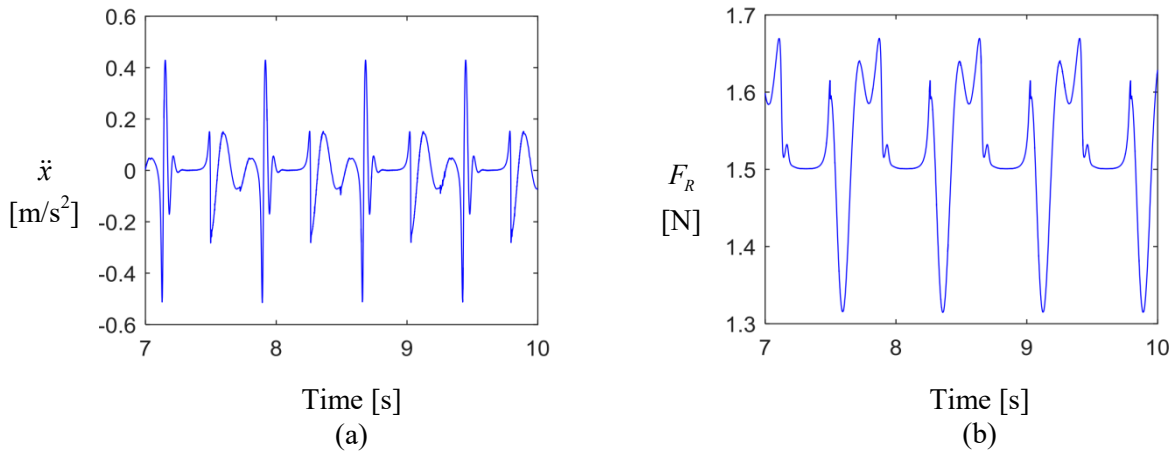

Fig. 3.22: Acceleration of the pad (a) and friction force (b) during the stick-slip motion

In the following, the stability of the system is analyzed. The equilibrium position of Eq. (3.43) is expressed as

$$\boldsymbol{Y}_{eq} = \begin{bmatrix} \Delta\theta_{eq} & 0 & x_{eq} & 0 & z_{eq} \end{bmatrix}^{\mathrm{T}}, \tag{3.44}$$

$$\Delta\theta_{eq} = r\left(N\mu_d + N(\mu_s - \mu_d)e^{-\Omega_0 r/v_s}\right)/k_\theta,$$

$$x_{eq} = \left(N\mu_d + N(\mu_s - \mu_d)e^{-\Omega_0 r/v_s}\right)/k_x, z_{eq} = \left(N\mu_d + N(\mu_s - \mu_d)e^{-\Omega_0 r/v_s}\right)/\sigma_0.$$

Linearizing Eq. (3.43) under its equilibrium position

$$\dot{\boldsymbol{Y}} = \boldsymbol{A}\boldsymbol{Y}, \tag{3.45}$$

$$\boldsymbol{A} =$$

$$\begin{bmatrix} 0 & 1 & 0 & 0 & 0 \\ -\dfrac{k_\theta}{I} & -\dfrac{d_\theta}{I} + \dfrac{r\sigma_1}{I}\dfrac{\partial\phi(\Delta\dot{\theta},\dot{x},z)}{\partial\Delta\dot{\theta}} & 0 & \dfrac{r\sigma_1}{I}\dfrac{\partial\phi(\Delta\dot{\theta},\dot{x},z)}{\partial\dot{x}} & \dfrac{r\sigma_0}{I} + \dfrac{r\sigma_1}{I}\dfrac{\partial\phi(\Delta\dot{\theta},\dot{x},z)}{\partial z} \\ 0 & 0 & 0 & 1 & 0 \\ 0 & \dfrac{\sigma_1}{m}\dfrac{\partial\phi(\Delta\dot{\theta},\dot{x},z)}{\partial\Delta\dot{\theta}} & -\dfrac{k_x}{m} & -\dfrac{d_x}{m} + \dfrac{\sigma_1}{m}\dfrac{\partial\phi(\Delta\dot{\theta},\dot{x},z)}{\partial\dot{x}} & \dfrac{\sigma_0}{m} + \dfrac{\sigma_1}{m}\dfrac{\partial\phi(\Delta\dot{\theta},\dot{x},z)}{\partial z} \\ 0 & \dfrac{\partial\phi(\Delta\dot{\theta},\dot{x},z)}{\partial\Delta\dot{\theta}} & 0 & \dfrac{\partial\phi(\Delta\dot{\theta},\dot{x},z)}{\partial\dot{x}} & \dfrac{\partial\phi(\Delta\dot{\theta},\dot{x},z)}{\partial z} \end{bmatrix}.$$

with

$$\frac{\partial\phi(\Delta\dot{\theta},\dot{x},z)}{\partial\Delta\dot{\theta}} = \frac{(\mu_s - \mu_d)r^2\Omega_0}{v_s(\mu_s - \mu_d + \mu_d e^{\Omega_0 r/v_s})}, \frac{\partial\phi(\Delta\dot{\theta},\dot{x},z)}{\partial\dot{x}} = \frac{(\mu_s - \mu_d)r\,\Omega_0}{v_s(\mu_s - \mu_d + \mu_d e^{\Omega_0 r/v_s})},$$

$$\frac{\partial\phi(\Delta\dot{\theta},\dot{x},z)}{\partial z} = \frac{-r\,\sigma_0\Omega_0}{N\mu_d + N(\mu_s - \mu_d)e^{-\Omega_0 r/v_s}},$$

where $\boldsymbol{A}$ is the corresponding system matrix. The stability of the equilibrium solution can be analyzed by the eigenvalues of $\boldsymbol{A}$. If the real parts of all eigenvalues are negative, the equilibrium solution is asymptotically stable. If any of the real parts of eigenvalues is positive, the equilibrium solution is unstable, and the solution will show increasing amplitudes. The stick-slip limit cycle of Eq. (3.43) can be determined by transient analysis using numerical integration.

Three different regions with different types of solutions are shown in Fig. 3.23. The white region is region I, where the system has no stick-slip limit cycle and has a stable equilibrium solution. The green region represents region II, where the system has a stable stick-slip limit cycle and a stable equilibrium solution. The yellow region denotes region III, where the system has a stable stick-slip limit cycle and an unstable equilibrium solution.
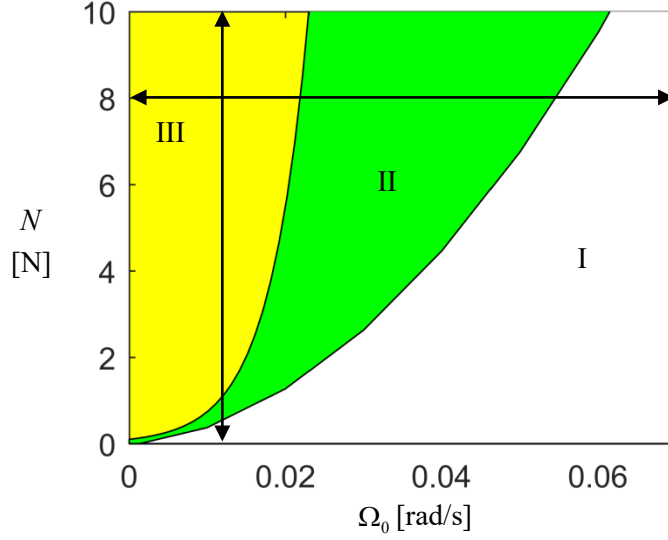
Fig. 3.23: Map of creep groan

Two simulations are given to explain the map of creep groan. At first, the normal force is increased from 0 N to 10 N under a constant driving speed. Simulation results are shown in Fig. 3.24 (a), where the blue line presents the vibration of the torsional angle ($\Delta\tilde{\theta} = \Delta\theta - \Delta\theta_{eq}$) and the red line denotes the normal force. It can be seen that the stick-slip motion occurs when the normal brake force is larger than a critical force N_{c23}. The reason is that the stick-slip limit cycle is the only stable solution when the system is in region III. The amplitude of the stick-slip vibration increases with the brake force. After that, the normal brake force is decreased from 10 N to 0 N. The stick-slip vibration will always exist until the normal brake force is lower than another critical force N_{c12}. The stick-slip vibration will vanish since the stick-slip solution does not exist in region I. N_{c23} is larger than N_{c12}, this can confirm the existence of region II. The critical forces obtained by the simulation with the continuously changed normal force are the same with the critical forces read from the map in Fig. 3.23. By applying short time Fourier transformation (using Hamming window with window size 6.2s) to the simulated torsional angle, the frequency of the stick-slip motion decreases with the brake force, shown in Fig. 3.24 (b).

Then, the driving speed is increased slowly under a constant brake normal force. The simulation results show in Fig. 3.25. At the beginning, the system is under low speed and in region III, the stick-slip limit cycle is the only stable solution of the system. The stick-slip motion exists until the speed is larger than a critical speed Ω_{c12}. When the speed is larger than Ω_{c12}, the stick-slip motion does not exist and the system will return to the equilibrium solution (in region I). After that, the speed is decreased slowly. The stick-slip motion appears once again when the speed is lower than a critical speed Ω_{c23}, which is smaller than Ω_{c12}. By applying short time Fourier transformation to the simulated torsional angle, it is clear that the frequency of the stick-slip motion increases with the speed, and approaches to the eigenfrequency of the system before the critical speed Ω_{c12} is reached.

Fig. 3.24: The stick-slip vibration with increasing and decreasing normal brake force (a) and their short time Fourier transformation using Hamming window with window size 6.3s, where bright color means the frequency with large amplitude (b)
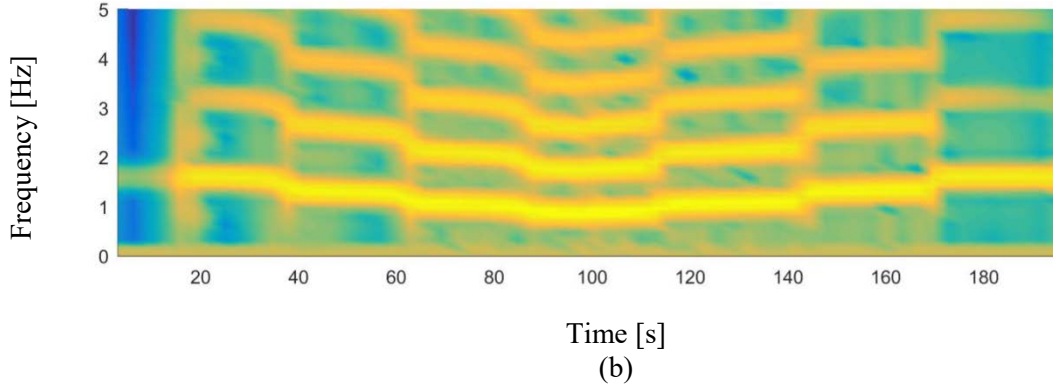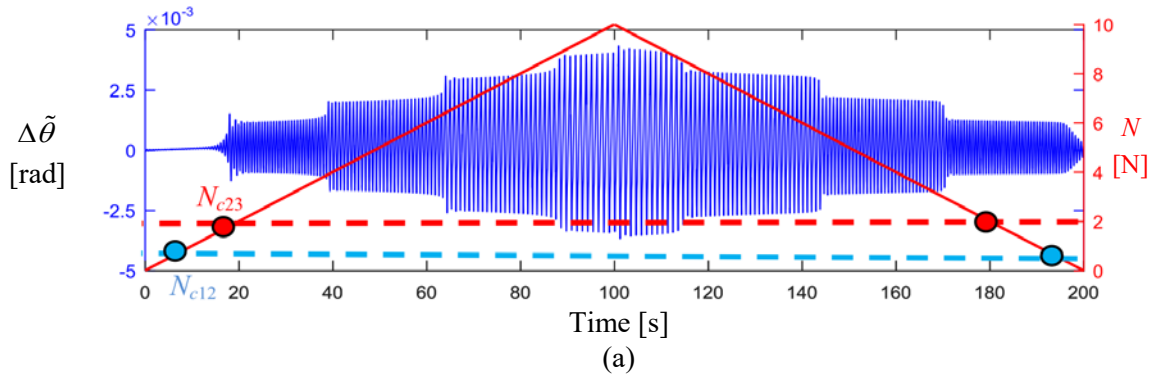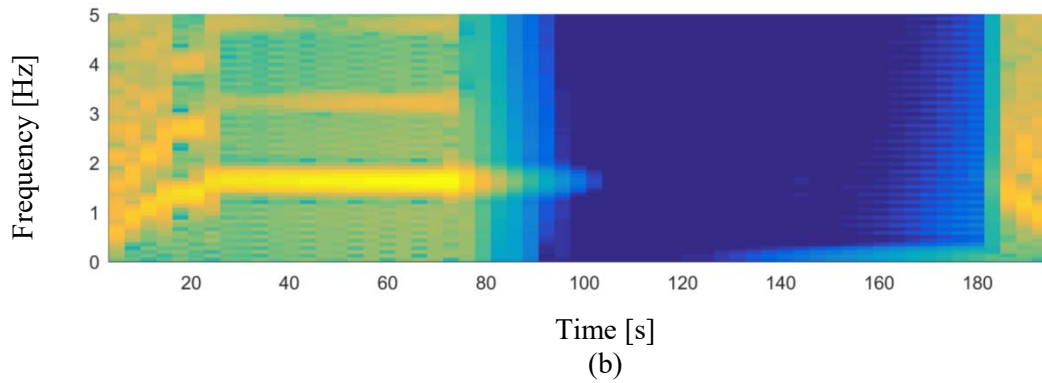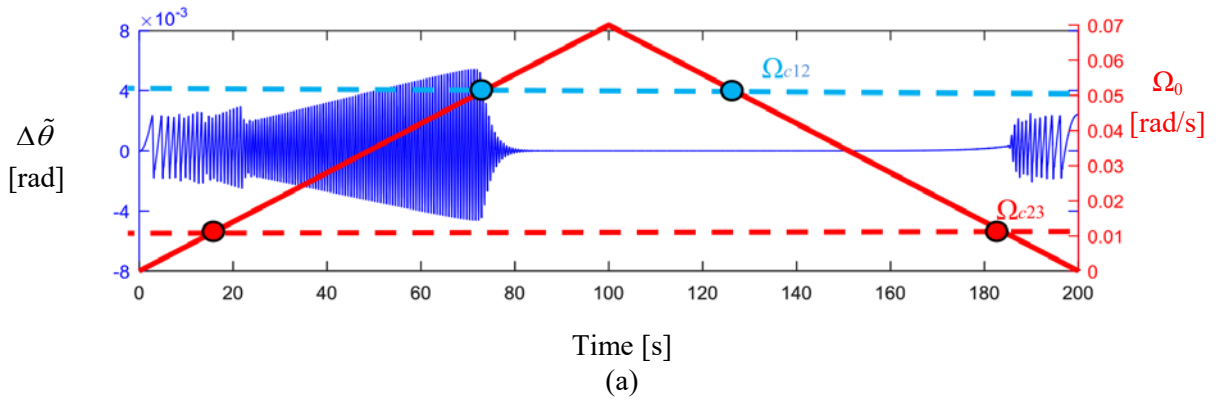

Fig. 3.25: The stick-slip vibration with increasing and decreasing motor speed (a) and their short time Fourier transformation using Hamming window with window size 6.3s (b)

3.3 Summary

In this chapter, different friction laws i.e. Coulomb's friction law and the bristle friction law are used to simulate creep groan of the test rig with an idealized brake. The disk is considered as a rigid body connected to the motor with a rotational spring. The two pads are treated as one rigid body connected to the based frame through a linear spring. The stick-slip limit cycle is firstly obtained by coupling the system model with Coulomb's friction law, in which the static friction coefficient is larger than the dynamic friction coefficient. However, the non-smooth characteristic appears between the stick and slip regions due to the switch function in Coulomb's friction law. As an improvement of the modeling, the bristle friction law, including the Stribeck velocity, pre-sliding effect and hysteresis, is used to describe the friction between the contact surfaces.

According to the stability of the equilibrium solution and existence of the stick-slip limit cycle, the system with Coulomb's friction has two parameters regions. A region with a stable equilibrium solution and no stick-slip limit cycle named as region I and a region with a stable equilibrium solution and a stick-slip limit cycle named as region II. In contrast, the model with the bristle friction law has three parameter regions. Except for regions I and II, there is an additional region with unstable equilibrium solution and a stable stick-slip limit cycle, which is named as region III. Table 3.3 exhibits the limit cycles and parameter regions of the system with different friction laws. Since different friction laws lead to different dynamic characteristics, one should be careful to choose the suitable friction law to describe creep groan of brake system.
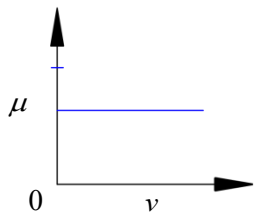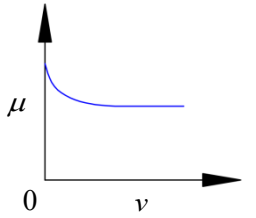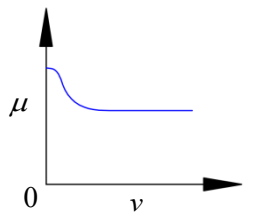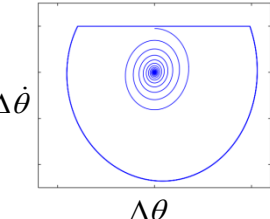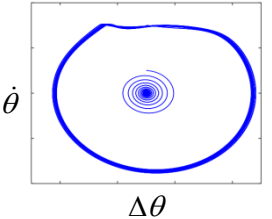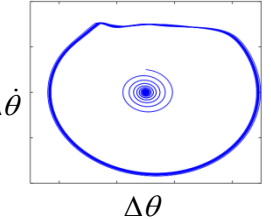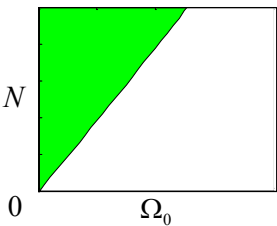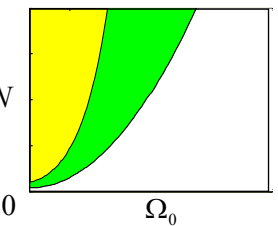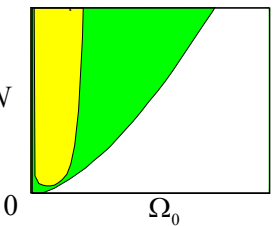
Friction law	Coulomb's model	Bristle model	
	(Switch function)	($\alpha = 1$)	($\alpha = 2$)

Table 3.3: Comparison of different models

4 Comparison study of experimental and theoretical results on the idealized brake

In this chapter, the parameters of the models with different friction laws will be identified. Then, the simulation will be quantitatively compared with the experimental results, which are measured from the test rig with an idealized brake. A friction observer will be designed at the end, to show an alternative way to obtain the friction force.

4.1 Parameter identification for the system with Coulomb's friction law

Considering the two DOFs model with Coulomb's friction law, the dynamic equations are given in Eqs. (3.14) and (3.15). Due to the simple structure of the test rig with an idealized brake, its parameters are easy to identify compared to the test rig with a real brake. The unknown parameters of the test rig with an idealized brake include the mass of the disk and pads, the stiffness, the damping of the shaft and the carrier, as well as the static and dynamic friction coefficients. The mass of the disk and the brake pads is measured by a weighing device. The stiffness and damping of the drive shaft and the carrier can be measured through modal analysis. The measured parameters are given in Table 4.1.

Parameters	Values	Parameters	Values
I	0.2025 kgm^2	k_x	$9.87 \cdot 10^6 \text{ N/m}$
k_θ	$1.036 \cdot 10^4 \text{ Nm}$	d_x	$3 \cdot 10^3 \text{ Ns/m}$
d_θ	2 Nms	r	0.15 m

Table 4.1: Parameters of the system

However, the static and dynamic friction coefficients cannot be directly measured. There is a simple way to identify those parameters from the measured stick-slip limit cycle. Assume that the system has low damping ratio, the shape of the limit cycle will be approximately symmetrical. As a result, the displacement during the stick region is approximate to $2Nr(\mu_s - \mu_d)/k_\theta$, and the symmetrical axis of the limit cycle lies in $Nr\mu_d/k_\theta$, shown in Fig. 4.1. Therefore, it is possible to measure the displacement of the stick region in the limit cycle and calculate the corresponding static and dynamic friction coefficients

$$\mu_s - \mu_d = (\Delta\theta_2 - \Delta\theta_1)k_\theta/(2Nr), \tag{4.1}$$
$$\mu_d = (\Delta\theta_2 + \Delta\theta_1)k_\theta/(2Nr),$$

where $\Delta\theta_1$ is the torsional angle when the system just enters the stick region, $\Delta\theta_2$ is the torsional angle when the system leaves the stick region.
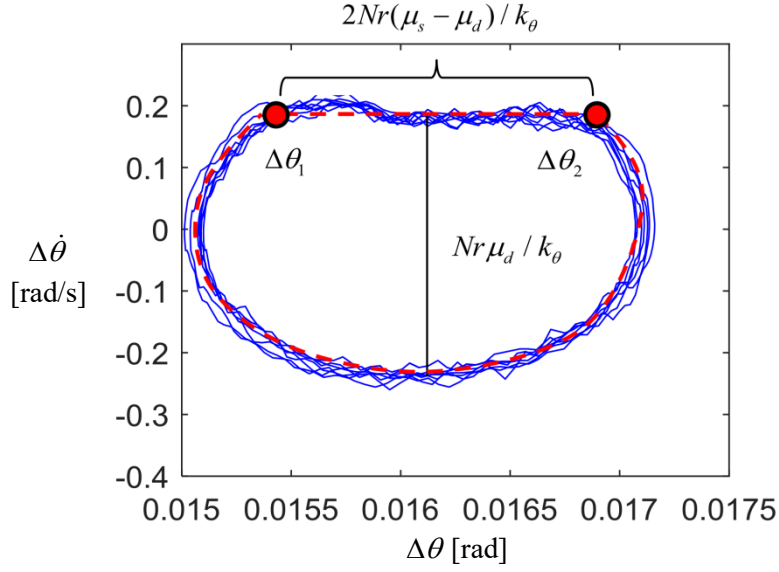
Fig. 4.1: Identification of the friction characteristic according to the limit cycle, $\Delta\theta_1$ is the torsional angle when the system just enters the stick region, $\Delta\theta_2$ is the torsional angle when the system leaves the stick region

According to Eq. (4.1), μ_d is equal to 0.325, $\mu_s - \mu_d$ is equal to 0.0125. With the parameters to hand, the torsional angle, torsional velocity as well as the friction force can be calculated through Eqs. (3.14) and (3.15). Fig. 4.2 shows the measured and simulated torsional angle and torsional velocity of the drive shaft, where the simulated results are presented with the red line and the experimental results are plotted with the blue line. The simulated acceleration of the brake pad is presented in Fig. 4.3 (a). A large impulse appears when the system converts to the slip region from the stick region due to the sudden change of the friction force as shown in Fig. 4.3 (b).
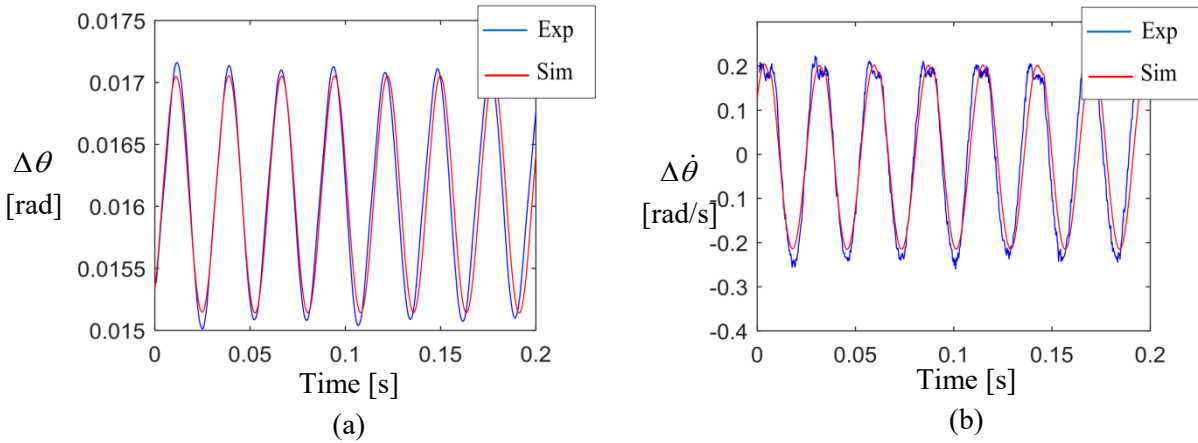
Fig. 4.2: Experimental and simulation torsional angle (a) and torsional velocity (b) of the shaft
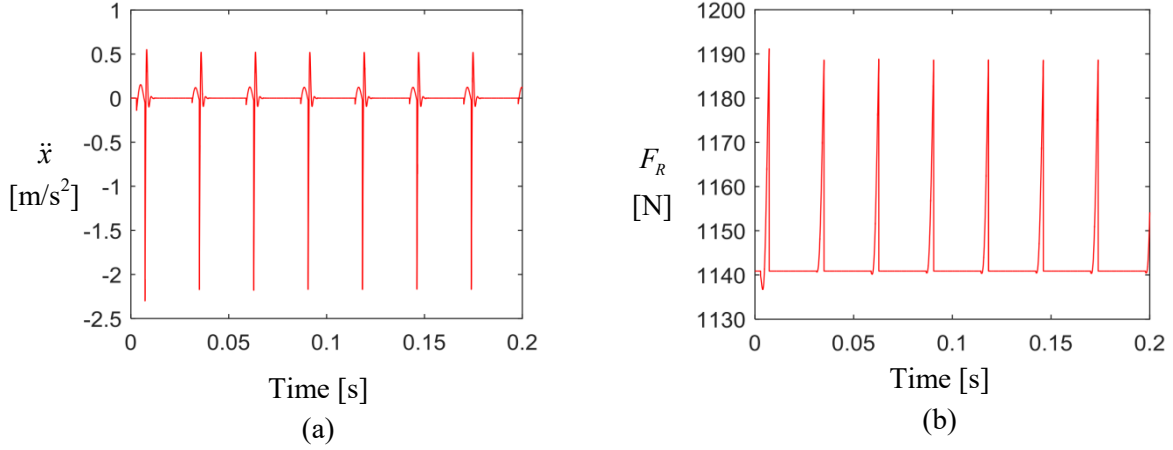
Fig. 4.3: Simulated acceleration of the pad (a) and friction force (b)

4.2 Parameter identification for the system with the bristle friction law

Parts of the experimental results in this section have already been described in [32], [33]. In order to describe the dynamic behaviors of the friction force, the bristle friction law is used to describe the friction contact between the pads and disk. Five parameters are employed to describe the friction force, in term of the static friction coefficient, the dynamic friction coefficient, the Stribeck velocity, the contact stiffness and the contact damping. Since they are difficult to measure, it is possible to estimate them through some parameter identification techniques. An objective function is identified by comparing the experimental results with the simulation results, which is defined as

$$W(X) = \sqrt{\sum_{i=1}^{n} e_i^2} = \sqrt{\sum_{i=1}^{n} (\Delta\theta_{\exp,i} - \Delta\theta_{\text{sim},i})^2 \omega_0^2 + (\Delta\dot{\theta}_{\exp,i} - \Delta\dot{\theta}_{\text{sim},i})^2}, \tag{4.2}$$

where i is the subscript of the sample points from 1 to n, n is maximal sample number, $\Delta\theta_{\exp,i}$ and $\Delta\theta_{\text{sim},i}$ are the measured and simulated torsional angles, $\Delta\dot{\theta}_{\exp,i}$ and $\Delta\dot{\theta}_{\text{sim},i}$ are the corresponding torsional velocities, $\omega_0^2 = k_\theta / I$. The objective function approaching the minimum value means that the simulation results have the best fit to the experimental results. The $\Delta\theta_{\text{sim},i}$ is calculated by Eq. (3.43) with given initial conditions in the stick region

$$\Delta\theta_0 = \Delta\theta_{\exp,0}, \Delta\dot{\theta}_0 = \Delta\dot{\theta}_{\exp,0}, x_0 = \frac{\Delta\theta_{\exp,0}k_\theta}{rk_x}, \dot{x}_0 = 0, z_0 = \frac{\Delta\theta_{\exp,0}k_\theta}{r\sigma_0}. \tag{4.3}$$

Classical optimization methods (such as gradient-based algorithms) are normally suitable for the parameter identification of a linear model [106]. The bristle friction model has high nonlinear characteristics and its optimization problem is not convex. Therefore, a binary genetic algorithm is used to find the minimum value of the objective function $W(X)$. A genetic algorithm is a metaheuristic inspired by the process of natural selection, which is commonly used to generate high-quality solutions to optimization problems by relying on bio-inspired operators such as mutation, crossover and selection. The genetic algorithm has the advantage to find the global minimum of non-convex optimization problems. The algorithm is given in the MATLAB genetic algorithm toolbox with its parameters shown in Table 4.2. After 200 generations, the objective function approaches the minimum value, and the optimized parameters are presented in Table 4.3. Fig. 4.4 shows the values of parame-

ters and the value of the objective function over each generation. In order to present the parameters with different physical units in one figure, they have been divided by their maximum optimal boundary. Once the parameters are obtained, the experimental and simulation results are compared with each other. Fig. 4.5 shows the measured and simulated torsional angle and torsional velocity of the drive shaft, while the simulated acceleration of the brake pads and the simulated friction force are presented in Fig. 4.6. When the system converts to the slip region from the stick region, a large impulse appears. Meanwhile, the simulated friction force changes suddenly.

Parameters	Values	Parameters	Values
Maximum generations number	200	Generation gap	0.8
Numbers of individual	10	Mutation probability	0.7

Table 4.2: Parameters of the genetic algorithm

Parameters	Values	Parameters	Values
μ_d	0.325	σ_1	$3.84 \cdot 10^5$ Ns/m
$\mu_s - \mu_d$	0.009	v_s	0.025 m/s
σ_0	$3.97 \cdot 10^8$ N/m		

Table 4.3: Parameters of the friction law
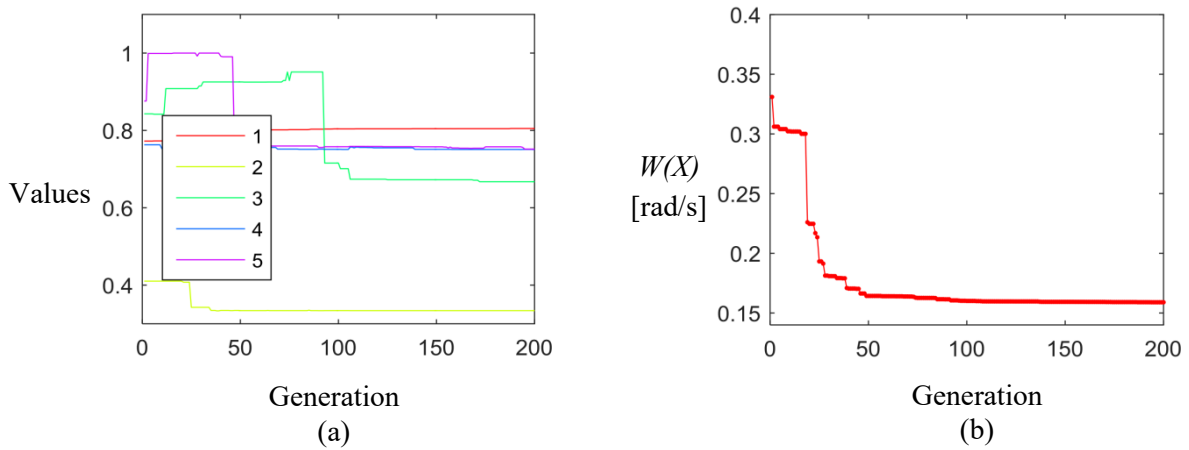
Fig. 4.4: Paramter values (a) and the value of $W(X)$ (b) in each generation

Fig. 4.7 exhibits the simulated stick-slip limit cycle by Coulomb's friction law compared to experimental results, while Fig. 4.8 exhibits the simulated stick-slip limit cycle by the bristle friction law compared to experimental results. Both simulated limit cycles are coincided with the measured limit cycle. It is clear that both friction laws have the ability to describe the stick-slip limit cycle [67], [68]. However, the bristle friction law can describe the pre-sliding effect between the stick and slip regions. In the later discussion, it can be found that the unstable equilibrium solution of the system under low speed will show up if the bristle friction law is used.

47
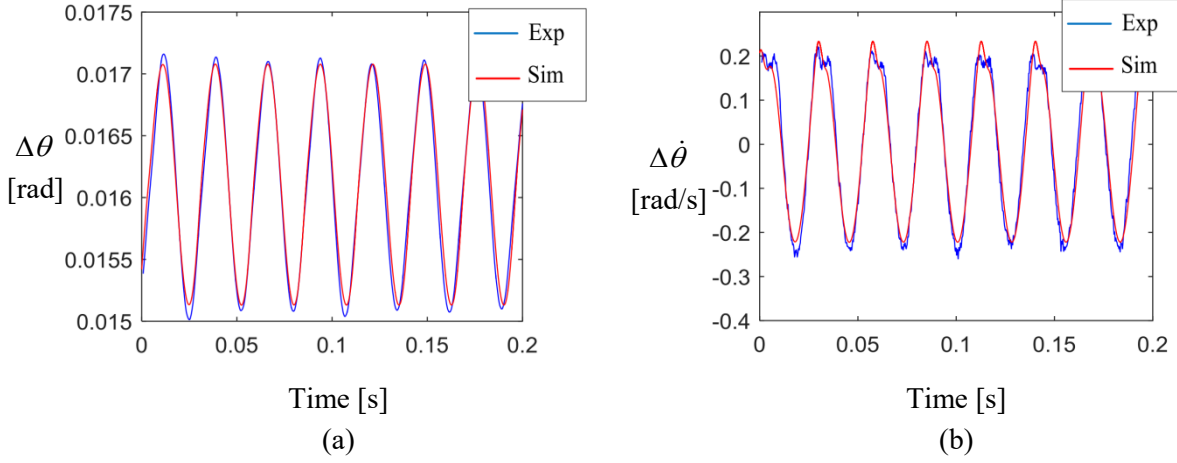
Fig. 4.5: Torsional angle (a) and torsional velocity (b) of the shaft
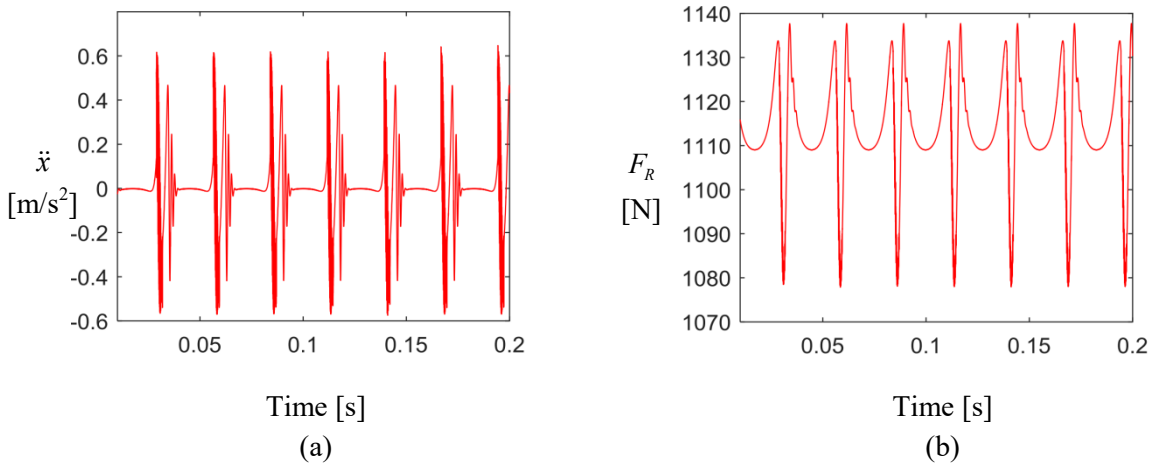
Fig. 4.6: Acceleration of the brake pads (a), and the simulated friction force (b).
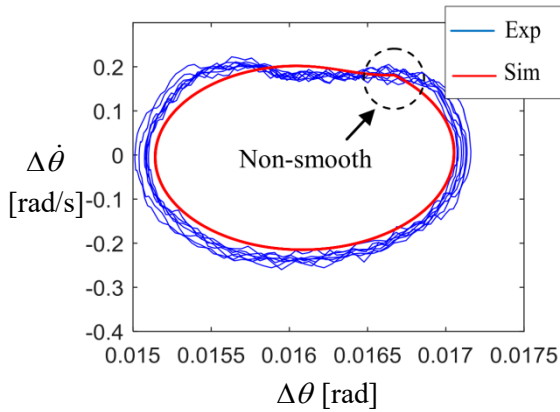
Fig. 4.7: Simulated stick-slip limit cycle by Coulomb's friction law compared to experiments
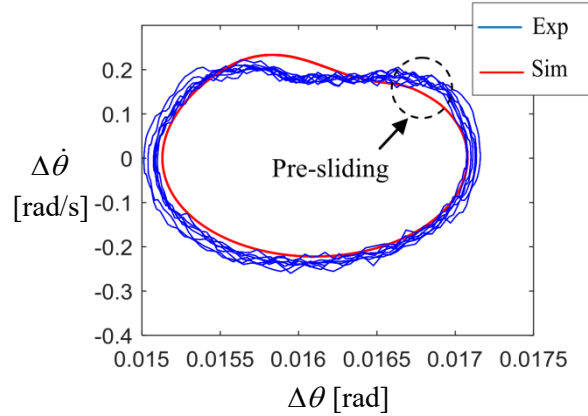
Fig. 4.8: Simulated stick-slip limit cycle by the bristle friction law compared to experiments

With the identified parameters of the system, the map of creep groan can be calculated through the method proposed in section 3.2, shown in Fig. 4.9, whose horizontal axis is the driving speed and the vertical axis is the brake pressure which is proportional to the brake normal force. According to the analysis of section 3.2, the system has three parameter regions if the bristle friction law is used. Region I means that the system has a stable equilibrium solution but no stick-slip limit cycle. Region II means that the system has a stable stick-slip limit cycle and equilibrium solution (and an unstable limit

cycle solution in between). Region III means that the system has a stable stick-slip limit cycle and an unstable equilibrium solution.

This map can be used to study creep groan during the accelerating and decelerating processes. If the operation starts with parameters in region III, creep groan must occur, as the limit cycle is the only stable solution. If then the parameter region of type II is entered from region III (i.e. with creep groan), creep groan will proceed until region I is entered. This is usually the case when the vehicle is accelerating. Different things will happen if the vehicle is decelerating. In region I the silent solution without creep groan is the only stable solution. The system will stay in the attractor of the silent solution when entering region II from region I and no creep groan occurs. Creep groan will then occur unless region III is entered.
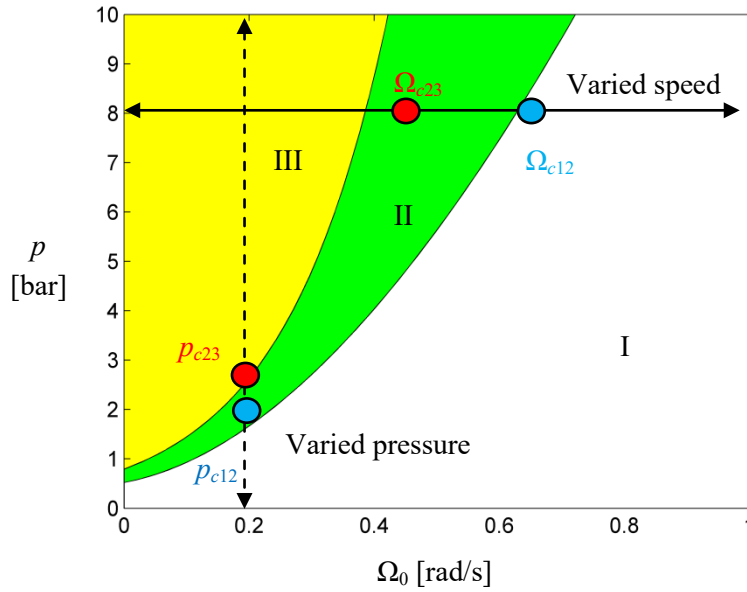
Fig. 4.9: Map of creep groan with identified parameters, the red points represent the measured boundary points between regions II and III, while the blue points represent the measured boundary points between regions I and II

Experiments are carried out to confirm the existence of the different critical conditions of creep groan during accelerating and decelerating of a vehicle, and the approach is shown in Fig. 4.9 with the solid line. The brake pressure is constant (8 bar) and the driving speed of the motor is varied. Corresponding experimental results are shown in Fig. 4.10. The red line describes the driving speed, while the blue line presents the torsional vibration angle $\Delta\tilde{\theta}$ ($\Delta\tilde{\theta} = \Delta\theta - \Delta\theta_{eq}$) of the drive shaft. The torsional vibration of the drive shaft becomes large when creep groan appears. At first, the speed is slowly increased from 0 rad/s to 0.7 rad/s, the system has creep groan at low speed, but creep groan disappears when the speed is higher than a critical speed Ω_{c12} (0.62 rad/s, marked with a red point in Fig. 4.9). After that, the speed is slowly decreased from 0.7 rad/s. Creep groan doesn't occur at high speed and appears when the speed is lower than another critical pressure Ω_{c23} (0.42 rad/s, marked with a blue point in Fig. 4.9). Therefore, the both critical speeds during accelerating and decelerating are found out, and the measured critical speeds are near the simulated boundary of regions. The difference between these two limit speeds in fact proofs the existence of region II with both stable equilibrium solution and limit cycle.

Fig. 4.11 shows the equilibrium solution and the limit cycle of the brake system with different speeds in the phase plot with $\Delta\dot{\tilde{\theta}}$ as a function of $\Delta\tilde{\theta}$. When the driving speed is higher than Ω_{c12}, only the equilibrium solution can be measured both in the accelerating and decelerating process, meaning that the system is in region I and creep groan cannot occur. When the speed is lower than Ω_{c23}, creep groan is measured in both processes, meaning that the system is in region III and creep groan always occurs in this region. When the speed is higher than Ω_{c23} but lower than Ω_{c12}, creep groan is measured in the accelerating process, but not in the decelerating process, meaning that the system is in region II. In the decelerating process, the system begins with the equilibrium solution and stays in the attractor of the stable equilibrium solution. In the accelerating process, the system begins with the stick-slip state, and the system is in the attractor of the stable limit cycle. Therefore, experiments demonstrated the existence of the three regions.

Fig. 4.10: Torsional vibration angle with variation of the speed of the motor, the red and blue points represent the measured boundary speeds

Fig. 4.11: The equilibrium solution and the stick-slip limit cycle with different speeds, (a) in region I, (b) in region II with coexistence of the stable equilibrium solution and limit cycle, (c) in region III

Another possibility to show the existence of the three regions is to keep the constant driving speed but vary the brake pressure. Here, the alternative approach is shown in Fig. 4.9 with the dotted line, where the driving speed of the motor is constant (0.2 rad/s) and the brake pressure varies. Corresponding experimental results are shown in Fig. 4.12. The red line describes the brake pressure, while the blue line presents the torsional vibration angle $\Delta\tilde{\theta}$ of the drive shaft. At first, the brake pressure is slowly increased from 0 bar to 5 bar, the system has no creep groan at low pressure, but creep groan occurs when the pressure is higher than a critical pressure p_{c23} (2.9 bar, marked with a red point in Fig. 4.9). After that, the pressure is slowly decreased from 5 bar to 0 bar. Creep groan occurs at high pressure

and disappears when the pressure is lower than another critical pressure p_{c12} (2.3 bar, marked with a blue point in Fig. 4.9). It should be noticed that the measured critical pressure are around the simulated boundary between regions. The difference between these two critical pressure values also proofs the existence of region II with both stable equilibrium solution and limit cycle. Fig. 4.13 shows the equilibrium solution and the limit cycle of the brake system under different pressure in the phase plot with $\Delta\dot{\tilde{\theta}}$ as a function of $\Delta\tilde{\theta}$. When the pressure is lower than p_{c12}, only the equilibrium solution can be measured in both the pressure-increasing and pressure-decreasing processes, meaning that the system is in region I. When the pressure is higher than p_{c23}, creep groan is measured in both processes, meaning that the system is in region III. When the pressure is lower than p_{c23} but higher than p_{c12}, creep groan is measured in the pressure-decreasing process but not in the pressure-increasing process, meaning that the system is in region II. In the pressure-increasing process, the system is in the attractor of the stable equilibrium solution, so that creep groan doesn't appear. In contrast, the system is in the attractor of the stable limit cycle and creep groan occurs.
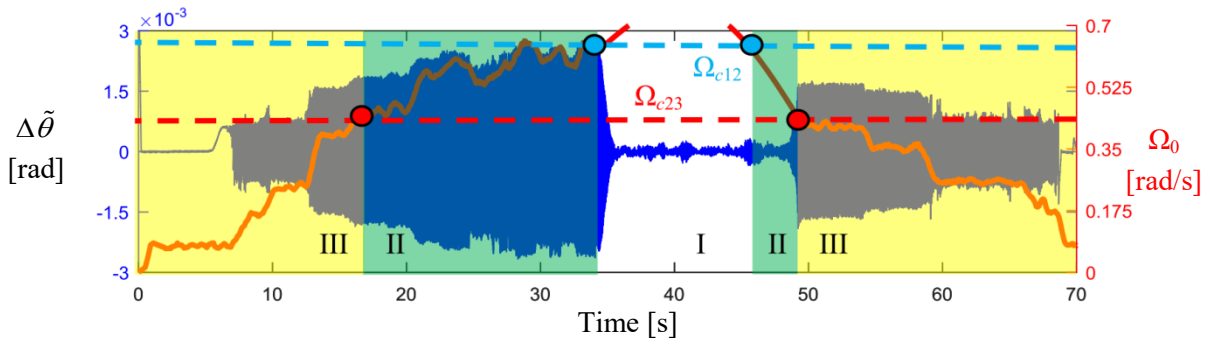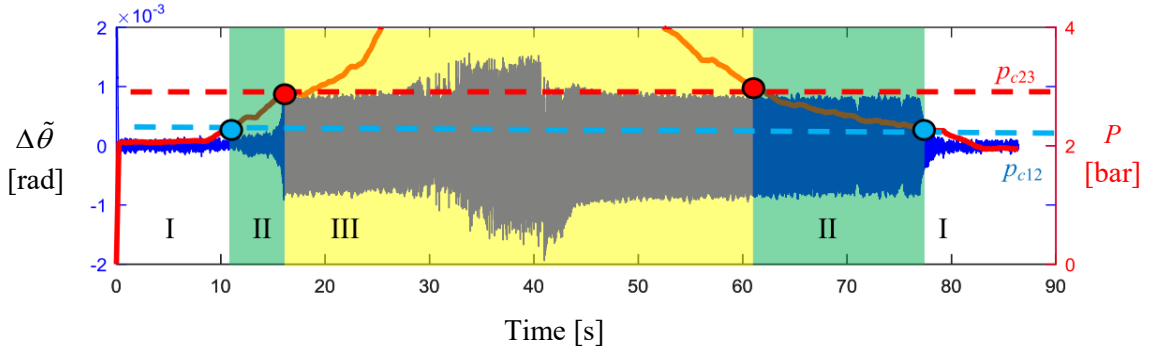

Fig. 4.12: Torsional vibration angle with variation of the brake pressure, the red and blue points represent the measured boundary pressure
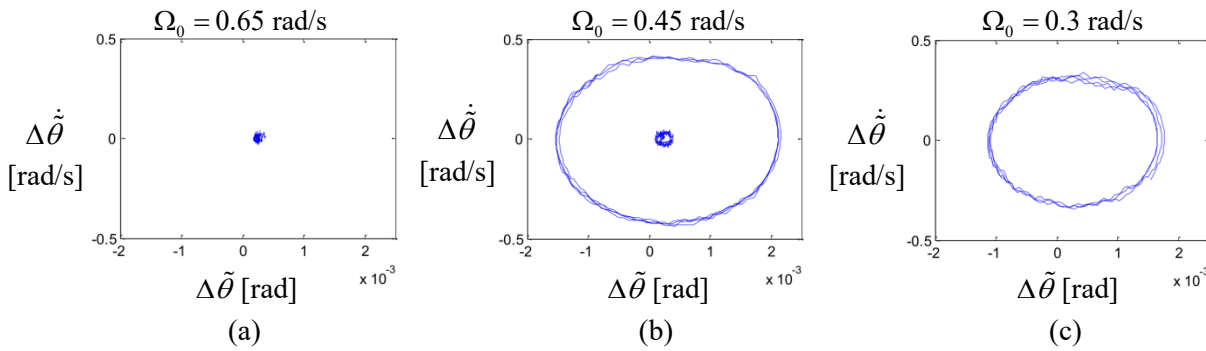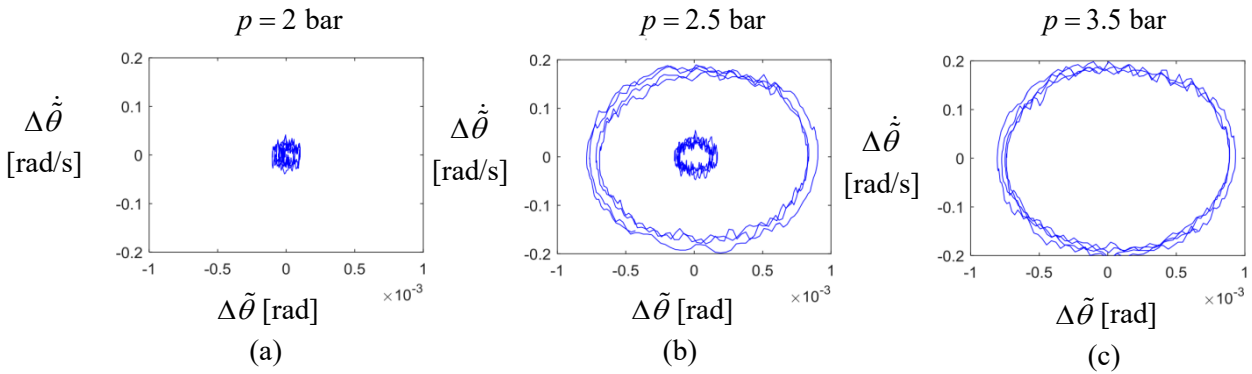

Fig. 4.13: The equilibrium solution and the stick-slip limit cycle with different pressure, (a) in region I, (b) in region II with coexistence of the stable equilibrium solution and limit cycle, (c) in region III

During the pressure-increasing process, the amplitude of the torsional angle increases with the brake pressure, shown in Fig. 4.14 (a). By applying short time Fourier transformation (SFFT) (using Hamming window with window size 0.5s) of $\Delta\dot{\tilde{\theta}}$, one can see that the frequency of the stick-slip motion decreases with increasing of the brake pressure, shown in Fig. 4.14 (b). Meanwhile, the amplitude of the acceleration of the pad $\ddot{x}$ increases with the brake pressure, shown in Fig. 4.14 (c). The reason is that the acceleration of the pad is proportional to the difference between static and dynamic friction forces, as well as the brake pressure. The SFFT of $\ddot{x}$ is presented in Fig. 4.14 (d). If the brake pressure

is large enough, some high frequency vibration of the carrier can be excited. For the low brake pressure, the frequency of peak appears at 200 Hz, while an additional peak frequency at 900 Hz appears when the brake pressure is larger than 6 bar.
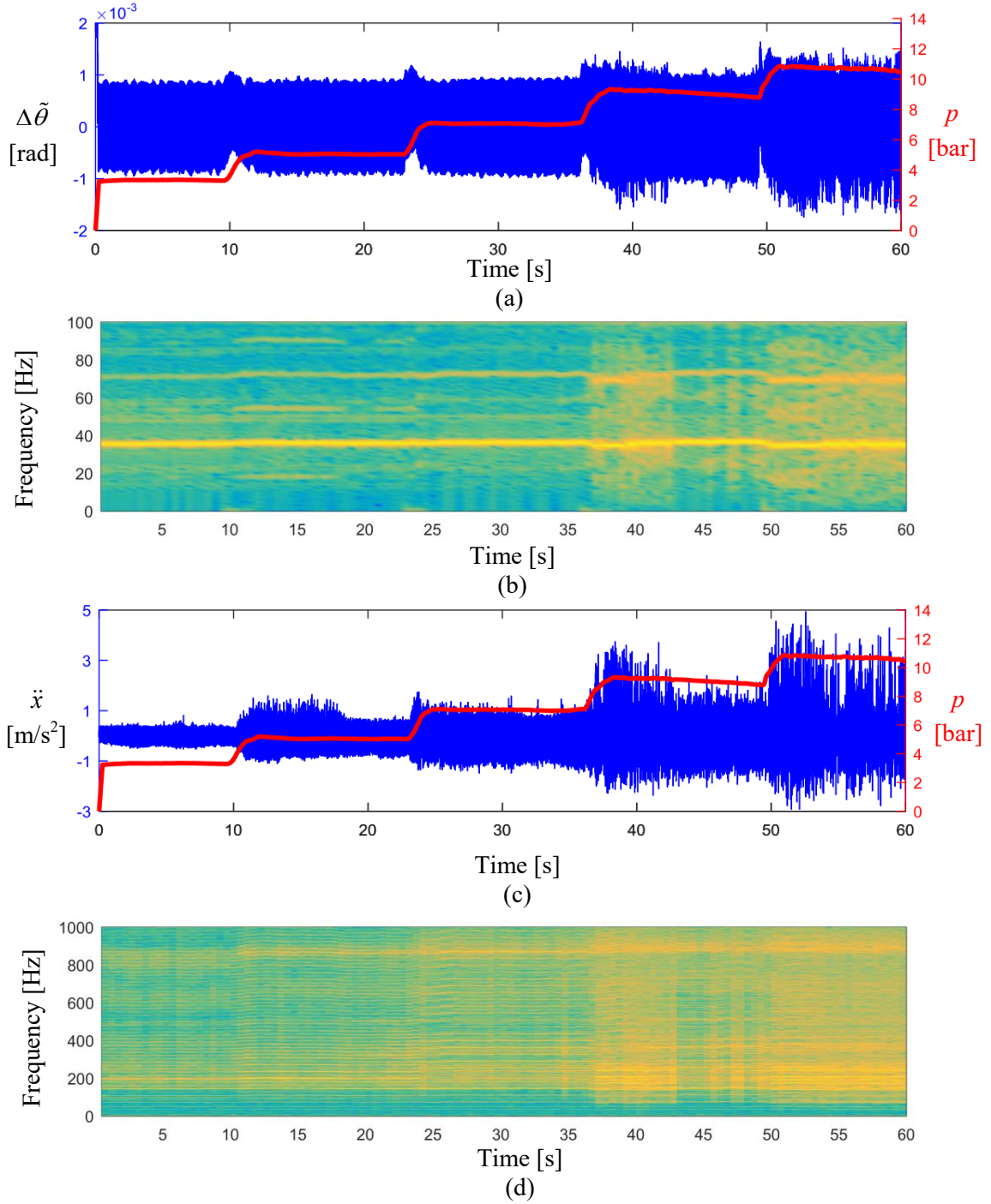
Fig. 4.14: Measured signals during pressure-increasing process, (a) vibration of the torsional angle $\Delta\tilde{\theta}$, (b) SFFT of $\Delta\dot{\tilde{\theta}}$, (c) acceleration of the pad $\ddot{x}$, (d) SFFT of $\ddot{x}$.

Similarly, the amplitude of the torsional angle increases with the speed, shown in Fig. 4.15 (a). The frequency of the stick-slip motion increases with the driving speed, and approaches the eigenfrequency of the shaft at high speed, expressed in Fig. 4.15 (b). Fig. 4.15 (c) shows that the amplitude of the acceleration of the pad, which is less influenced by the speed, since the brake pressure is constant. The SFFT of $\ddot{x}$ is presented in Fig. 4.15 (d). The speed has less influence on the vibration frequency of the pad.
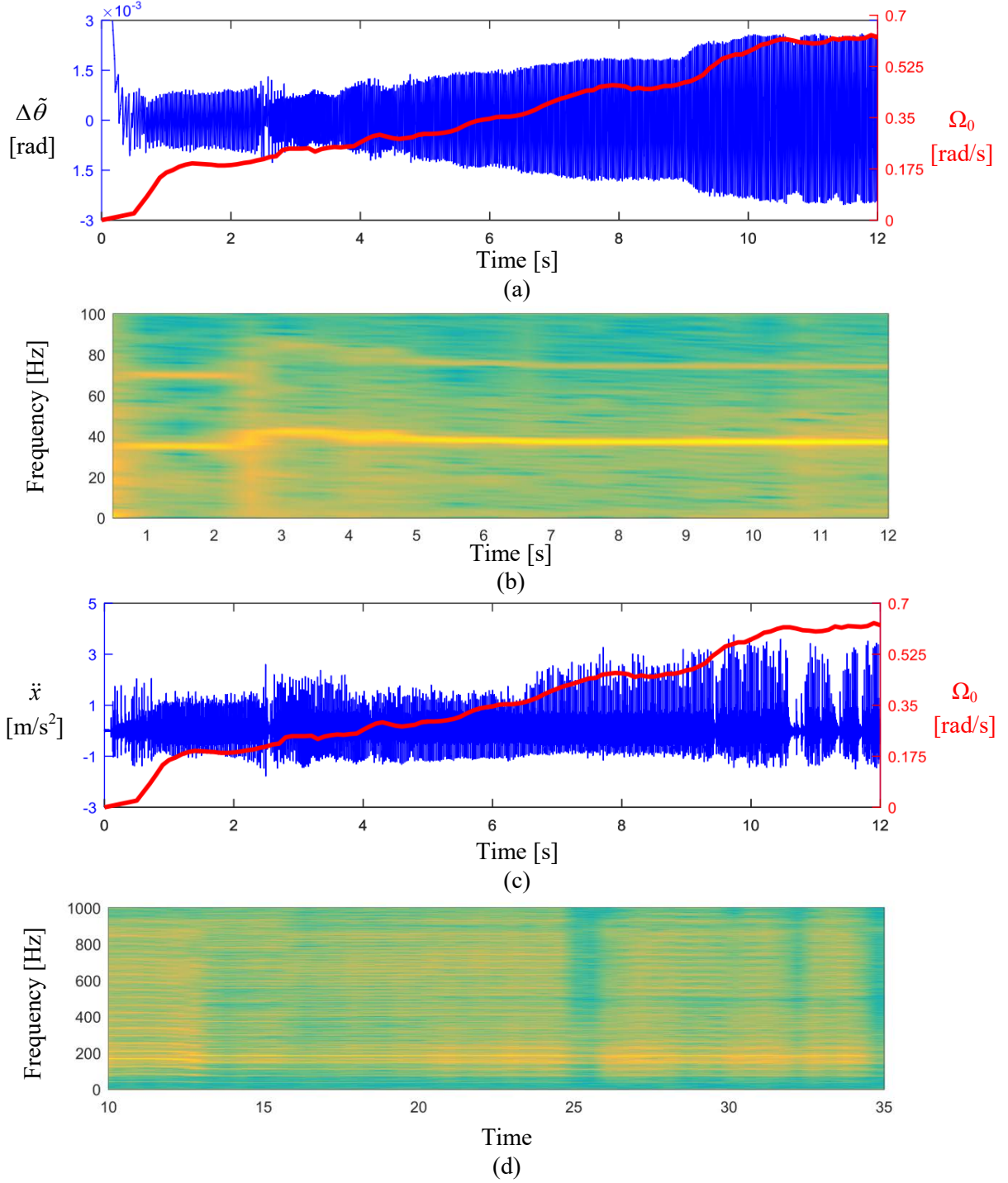
Fig. 4.15: Measured signals during accelerating process, (a) vibration of the torsional angle $\Delta\tilde{\theta}$, (b) SFFT of $\Delta\dot{\tilde{\theta}}$, (c) acceleration of the pad $\ddot{x}$, (d) SFFT of $\ddot{x}$.

4.3 Friction observer

It is possible to calculate the friction according to the abovementioned model. However, a lot of work is required for modeling and parameter identification. Therefore, in this section, an observer is designed to estimate the friction force directly from the measured signals.

In the brake system, the friction force acts on the brake disk and leads to a torsional deformation of the drive shaft. If the friction force is considered as an input of the disk-shaft sub-system, and the torsional angle and angle velocity of the drive shaft are treated as the state variables, the dynamic system is

$$\begin{bmatrix} \Delta\dot\theta \\ \Delta\ddot\theta \end{bmatrix} = \begin{bmatrix} 0 & 1 \\ -\dfrac{k_\theta}{I} & -\dfrac{d_\theta}{I} \end{bmatrix} \begin{bmatrix} \Delta\theta \\ \Delta\dot\theta \end{bmatrix} + \begin{bmatrix} 0 \\ \dfrac{r}{I} \end{bmatrix} F_R,$$

$$X = \begin{bmatrix} \Delta\theta & \Delta\dot\theta \end{bmatrix}^{\mathrm{T}},$$

(4.4)

where F_R is the input friction force, and X are the state variables. Since the state variables $\Delta\theta$ and $\Delta\dot\theta$ are known, and F_R changes slowly compared to the sample frequency, it is possible to design a Proportional-Integral observer to estimate the unknown input force F_R [107], [108]. The observer is given as

$$\begin{bmatrix} \dot{\hat X} \\ \dot{\hat F_R} \end{bmatrix} = \begin{bmatrix} A & B \\ 0 & 0 \end{bmatrix} \begin{bmatrix} \hat X \\ \hat F_R \end{bmatrix} + \begin{bmatrix} L_1 \\ L_2 \end{bmatrix} (X - \hat X),$$

$$\hat X = \begin{bmatrix} \Delta\hat\theta & \Delta\dot{\hat\theta} \end{bmatrix}^{\mathrm{T}}, A = \begin{bmatrix} 0 & 1 \\ -k_\theta/I & -d_\theta/I \end{bmatrix}, B = \begin{bmatrix} 0 & r_0/I \end{bmatrix}^{\mathrm{T}},$$

(4.5)

where L_1 and L_2 is the observer matrixes, $\Delta\hat\theta$ and $\Delta\dot{\hat\theta}$ are the estimated torsional angle and torsional velocity. If the above equations is reformed so that X is as the input and $\hat X$ and $\hat F_R$ are the state variables, then

$$\begin{bmatrix} \dot{\hat X} \\ \dot{\hat F_R} \end{bmatrix} = \begin{bmatrix} A - L_1 & B \\ -L_2 & 0 \end{bmatrix} \begin{bmatrix} \hat X \\ \hat F_R \end{bmatrix} + \begin{bmatrix} L_1 \\ L_2 \end{bmatrix} X.$$

(4.6)

After the transformation, the unknown input is considered as a state variable. The error dynamics of the observer is

$$\begin{bmatrix} \dot e \\ \Delta\dot F_R \end{bmatrix} = \begin{bmatrix} A - L_1 & B \\ -L_2 & 0 \end{bmatrix} \begin{bmatrix} \hat X \\ \Delta F_R \end{bmatrix},$$

(4.7)

where $\dot e = X - \hat X$ and $\Delta F_R = F_R - \hat F_R$. If the matrix $\begin{bmatrix} A - L_1 & B \\ -L_2 & 0 \end{bmatrix}$ has only eigenvalues with negative real part and the unknown input changes slowly (i.e. quasi-static), the estimated errors converge asymptotically to zero, and $\hat F_R \approx F_R$ after finite time. According to the convergent critical, observer matrixes are chosen as $L_1 = \begin{bmatrix} 10^3 & 0 \\ 0 & 10^3 \ 1/s \end{bmatrix}$ and $L_2 = \begin{bmatrix} 10^7 \ \mathrm{N/s} & 10^7 \ \mathrm{N} \end{bmatrix}$. Fig. 4.16 shows the flow

chart of the designed observer. The friction force can be observed through the measured state variables. Fig. 4.17 exhibits the observed friction force. After some time $\hat{F}_R$ becomes stable and is approximate to the real friction force. It is easy to distinguish the static friction force from the dynamic friction force, where the dynamic friction force approaches a constant while the static friction force varies between the minimal and maximum values (marked with blue color in Fig. 4.17 (b)). Compared to the modeling approach, designing a friction observer requires only a linear disk-shaft model, so that the parameters of the friction law don't need to be identified. However, a disadvantage is that the measurement noise will strongly influence the accuracy of the observed friction force.
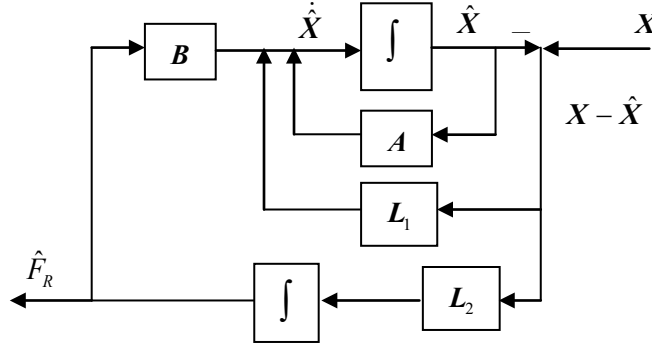
Fig. 4.16: Flow chart of the friction force observer
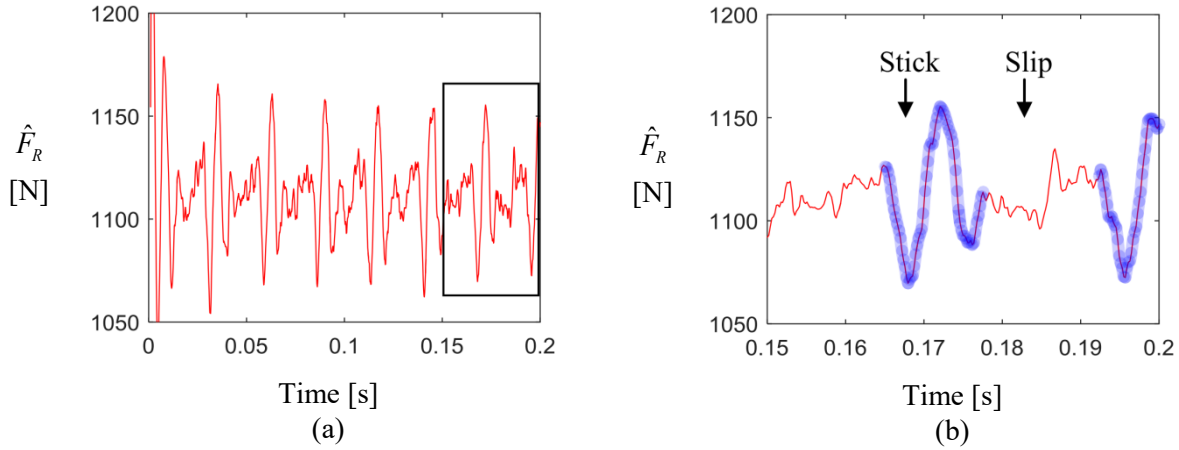
Fig. 4.17: Observed friction force (a) and it enlarged details (b), where the stick region marked with blue color

At the end, the calculated friction forces from different models are compared with the observed friction force in Table 4.4. The observed friction force is similar to the friction calculated by the model with the bristle friction law. It proves that the bristle friction law is more suitable to describe the contact interface between the disk and the pads. In contrast, Coulomb's friction law cannot describe the full dynamics of the friction.

Modeled friction by Coulomb's friction law	Modeled friction by the bristle friction law	Observed friction
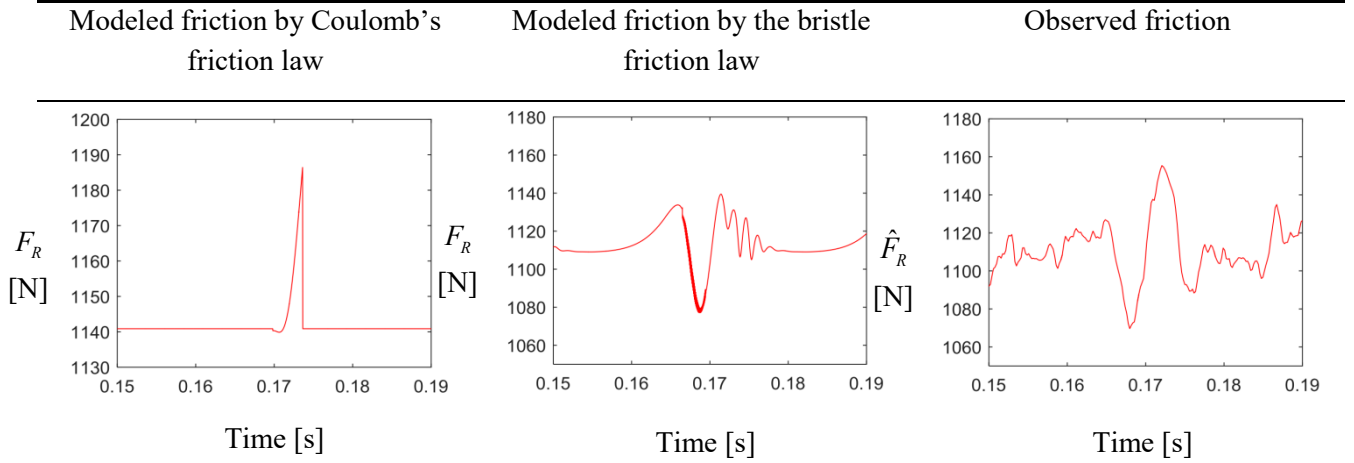
Table 4.4: Simulated friction force and the observed friction force

4.4 Summary

In this chapter, parameter identification methods are proposed for the models with different friction laws. For the model with Coulomb's friction law, its static and dynamic friction coefficients can be identified by analyzing the geometric shape of the stick-slip limit cycle. For the model with the bristle friction law, their parameters, including the static friction coefficient, the dynamic friction coefficient, the Stribeck velocity, the contact stiffness, and the contact damping, are estimated by comparing the simulated and measured results. A genetic algorithm is assisted to find the optimized parameter set.

The model with the bristle friction law indicated that the brake system has three regions of parameters according to the stability of the equilibrium solution and the existence of the stick-slip limit cycle. Two possible methods are employed to confirm the three parameter regions. One way is to keep the brake pressure constant and vary the driving speed; another way is to keep the driving speed constant and vary the brake pressure. Both experiments are carried out and the theoretical and experimental results have good agreement with each other. In the region II, both stable equilibrium solution and the stick-slip limit cycle can be measured with different initial conditions.

At the end, a Proportional-Integral observer is designed to observe the friction force from the measured $\Delta\theta$ and $\Delta\dot{\theta}$. Compared to the modeling method, designing a friction observer requires only a linear disk-shaft model, so that the parameters of the friction law don't need to be identified. However, it has a disadvantage that the measurement noise will strongly influence the accuracy of the observed force. By comparing the calculated friction force with the observed friction force, it is found that the observed friction force is more similar to the friction calculated by the model with the bristle friction law than that with Coulomb's friction law. It proves that the bristle friction law is more suitable to describe the friction interface of the brake system.

5 Theoretical and experimental analysis of creep groan on the test rig with a real brake

In this chapter, a dynamic model of the test rig with a real brake is studied. Different from the test rig with an idealized brake, the test rig with a real brake consists of a complex brake carrier with a suspension system. Therefore, a model with large number of degrees of freedom is required to describe the dynamic system. With respect to the modeling, it is hard to identify the stiffness and damping of each component of the test rig due to their complex construction. On the other hand, it needs plenty of calculation time for the transition analysis of a nonlinear system with large number of degrees of freedom. In order to solve these issues, Butlin and Woodhouse use the transfer function model to describe the friction-induced vibration [109]. Inspired by this work, a reduced-order model expressed by transfer functions is studied in this chapter. After parameter identification of the reduced-order model, simulation results will be compared with the experimental results. Some results of experimental investigations are already described in [33].

5.1 Modeling of the test rig with a real brake

The real brake system can be decomposed into three sub-systems, in terms of the rotating parts, the non-rotating parts and the friction interface. The rotating parts include the disk, the drive shaft and the motor. The non-rotating parts include the brake pads, the carrier, the caliper, and the suspension system. During modeling, the suspension is considered as a rigid body and hung on the basic frame with a set of mass-spring systems. According to experimental analysis, both pads move simultaneously during creep groan. Then, two pads are treated as one rigid body which connects to the suspension through a set of mass-spring systems. The disk is assembled in the drive shaft, which is supported by a bearing assembled in the suspension. The shaft is driven by the motor with a reduction gear box. The structure of the brake test rig and its dynamic model are sketched in Fig. 5.1.
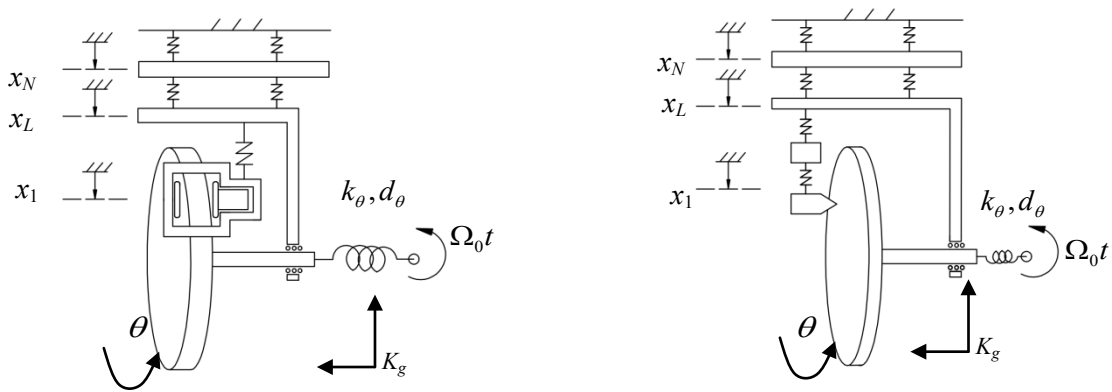
Fig.5.1: Structure of the test rig of real brake and its dynamic model

The dynamic equation of the non-rotating parts is given as

$$M\ddot{X} + D\dot{X} + KX = F,$$

(5.1)

where

$$X = \begin{bmatrix} x_1 & x_2 & ... & x_N \end{bmatrix}^{\mathrm{T}}, M = \mathrm{diag}(\begin{bmatrix} m_1 & m_2 & ... & m_N \end{bmatrix}),$$

$$D = \beta K, F = \begin{bmatrix} F_R & 0 & ... & 0 \end{bmatrix}^{\mathrm{T}},$$

$$K = \begin{bmatrix} k_1 & -k_1 & 0 & 0 & 0 \\ -k_1 & ... & & ... & 0 & 0 \\ 0 & ... & k_L + k_{L+1} & ... & 0 \\ 0 & 0 & ... & ... & -k_{N-1} \\ 0 & 0 & 0 & -k_{N-1} & k_N \end{bmatrix},$$

where M is the mass matrix, D and K are the damping and stiffness matrixes, which are symmetric matrices, F_R is the friction force, x_1, x_L and x_N are the displacement of the pad, the suspension and the frame in vertical direction, respectively. It is assumed that D is a proportional modal damping proportional to K with a factor β.

The rotating parts consist of the disk and the drive shaft. Its dynamic equation is written as

$$I\Delta\ddot{\theta} + d_\theta \Delta\dot{\theta} + k_\theta \Delta\theta = F_R r, \tag{5.2}$$

where r is the radius of the point where the pad acts, k_θ and d_θ are the stiffness and damping of the drive shaft, $\Delta\theta$ is the torsional angle of the drive shaft.

According to the bristle friction law, the friction force between the contact surface of the pads and disk is

$$F_R = \sigma_0 z + \sigma_1 \dot{z}, \tag{5.3}$$

and $\dot{z}$ is a nonlinear function of v and z

$$\dot{z} = \phi(v, z) = v - \frac{z}{g_0}|v|. \tag{5.4}$$

and

$$g_0 = \frac{1}{\sigma_0}\left(N\mu_d + N(\mu_s - \mu_d)\exp\left(-|v/v_s|\right)\right), \tag{5.5}$$

where g_0 is a scalar including the Stribeck effect, v is the relative velocity between the pads and disk. It is important to define v. Since the disk is rotating around the bearing fixed in the suspension, the disk has no relative transition motion referring to the suspension. Then, the relative velocity between the pad and disk is

$$v = \Omega_0 r - \Delta\dot{\theta} r + \left(\dot{x}_1 - \dot{x}_L\right), \tag{5.6}$$

where $\dot{x}_1$ is the velocity of the pads in vertical direction, $\dot{x}_L$ is the velocity of the suspension in vertical direction, Ω_0 is the driving speed of the motor, the rotating angle of the disk is $\dot{\theta}$, and the torsional angle of the shaft is $\Delta\dot{\theta}$ with $\Delta\dot{\theta} = \Omega_0 - \dot{\theta}$. The relationship in Eq. (5.6) is also true for a real vehicle, i.e. it is possible to isolate the brake-suspension system from the frame or the chassis for the study of the stick-slip motion, and complex components such as the chassis can be at first ignored.

Substituting Eqs. (5.3)-(5.6) into (5.1) and (5.2), the integrated dynamics of the test rig can be written as first order differential equations

$$
\begin{bmatrix} \Delta\dot\theta \\ \dot{X} \\ \Delta\ddot\theta \\ \ddot{X} \\ \dot{z} \end{bmatrix} = \begin{bmatrix} \Delta\dot\theta \\ \dot{X} \\ -\dfrac{d_\theta}{I}\Delta\dot\theta - \dfrac{k_\theta}{I}\Delta\theta + \dfrac{r}{I}F_R \\ -\boldsymbol{M}^{-1}\boldsymbol{D}\dot{X} - \boldsymbol{M}^{-1}\boldsymbol{K}X + \boldsymbol{M}^{-1}\boldsymbol{F} \\ \Omega_0 r - \Delta\dot\theta r - (\dot{x}_1 - \dot{x}_L) - \dfrac{z}{g_0}\left|\Omega_0 r - \Delta\dot\theta r - (\dot{x}_1 - \dot{x}_L)\right| \end{bmatrix}.
\tag{5.7}
$$

5.2 A reduced-order model for the simulation of creep groan

In practice, it is very hard to measure the damping and stiffness matrix $\boldsymbol{D}$ and $\boldsymbol{K}$. Instead, it is possible to measure the transfer function of the non-rotating parts by modal analysis. Therefore, $\dot{x}_{1-L}$ can be expressed through a rational transfer function $H_{x1-xL,F}(j\omega)$ as

$$
\dot{x}_{1-L} = \dot{x}_1 - \dot{x}_L = H_{x1-xL,F}(j\omega)F_R,
\tag{5.8}
$$
$$
H_{x1-xL,F}(j\omega) = \frac{a_{2L-1}(j\omega)^{2L-1} + a_{2L-2}(j\omega)^{2L-2} + ... + a_2(j\omega)}{(j\omega)^{2L} + b_{L-1}(j\omega)^{2L-1} + ... + b_1} \frac{\text{s}}{\text{kg}},
$$

where the input of the transfer function is the friction force, the output is the relative velocity of the pad referring to the suspension, ω represents the angular frequency with unit [rad/s], j is the imaginary unit with the property $j^2 = -1$ [107]. The transfer function is the ratio of two polynomials. The orders of the numerator polynomials are less than the orders of the denominator polynomials. The poles of the transfer function correspond to values of the ω-variable for which the denominator polynomial is zero. The zeros of the transfer function correspond to values of the ω-variable for which the nominator polynomial is zero.

The transfer function can also be written in the partial transfer function, which is expressed as the sum of independent second order transform functions. Since $\boldsymbol{D}$ is proportional to $\boldsymbol{K}$, the partial transfer function has a standard form as

$$
H_{x1-xL,F}(j\omega) = \sum_{i=1}^{L} H_i(j\omega) = \sum_{i=1}^{L} \frac{\alpha_i(j\omega)}{(j\omega)^2 + d_i(j\omega) + k_i},
\tag{5.9}
$$

where $H_i(j\omega)$ is a mode of the system. The transfer function can be obtained from the FE model, multi-body dynamic model, or measured by modal analysis on the test rig. Since the original transfer function may have lots of modes, it is necessary to reduce them to gain a reduced-order model. For purposes of potential modes reduction, the H_2 norm of $H_i(j\omega)$ is calculated, and the modes with $\left\| H_i(j\omega) \right\|_2 > \varepsilon$ is defined as the relative importance modes [110]. $\left\| \cdot \right\|_2$ is H_2 norm of a stable continuous-time system and measures the steady-state power of the output response, which is given by

$\left\| H_i(j\omega) \right\|_2 = \sqrt{\dfrac{1}{2\pi}\displaystyle\int_{-\infty}^{\infty}\mathrm{Trace}\left[H_i(j\omega)^H H_i(j\omega) \right]d\omega}$. ε is a threshold determined by the designer. By ignoring relative unimportant modes, the reduced-order transfer function can be written as

$$\tilde{H}_{x1-xL,F}(j\omega) = H_{x1-L,F}(j\omega) - \Delta H_{x1-xL,F}(j\omega) = \sum_{i=1}^{L_R}\frac{\alpha_i(j\omega)}{(j\omega)^2 + d_i(j\omega)+k_i}, \tag{5.10}$$

where $L_R < L$, $\tilde{H}_{x1-xL,F}(j\omega)$ consists of the relative important modes, $\Delta H_{x1-xL,F}(j\omega)$ is the relative unimportant modes. In order to simplify the calculation, $\tilde{H}_{x1-xL,F}(j\omega)$ is instead of $H_{x1-xL,F}(j\omega)$ to calculate the friction force.

For the rotating parts, Eq. (5.2) converts to a transform function as

$$\Delta\dot{\theta} = H_{\theta,F}(j\omega)F_R = \frac{r(j\omega)}{I(j\omega)^2 + d_\theta(j\omega)+k_\theta}F_R, \tag{5.11}$$

where $H_{\theta,F}$ is a transfer function from the input friction force to the torsional velocity of the shaft.

Then, the complete equations of the reduced-order model are given as

$$\begin{bmatrix} \Delta\dot{\theta} \\ \dot{x}_{1-L} \end{bmatrix} = \begin{bmatrix} H_{\theta,F}(j\omega) \\ \tilde{H}_{x1-xL,F}(j\omega) \end{bmatrix}(\sigma_0 z + \sigma_1 \dot{z}), \tag{5.12}$$

$$\dot{z} = \phi(\Delta\dot{\theta}, \dot{X}_p, z) = \Omega_0 r - \Delta\dot{\theta}r - \dot{x}_{1L} - \frac{z}{g_0}|\Omega_0 r - \Delta\dot{\theta}r - \dot{x}_{1L}|.$$

With two transfer functions to hand, the calculation procedure is given as follows with its flow chart in Fig. 5.2:

1. Give the initial relative velocity $\dot{x}_{1-L}$ and the torsional velocity $\Delta\dot{\theta}$,

2. Calculate the friction force by the bristle friction law with given $\dot{x}_{1-L}$ and $\Delta\dot{\theta}$,

3. Let the calculated friction force feedback to the transfer function $\tilde{H}_{x1-xL,F}(j\omega)$ and $H_{\theta,F}(j\omega)$, so that the $\dot{x}_{1-L}$ and $\Delta\dot{\theta}$ for the next time step can be calculated,

4. Repeat steps 1 to 3 iteratively to obtain the friction force during creep groan.

Compared to the original model, the reduced-order model has some advantages. On the one hand, the calculation time of the reduced-order model is much less than that of original model; on the other hand, only the system parameters are required in the reduced-order model, which can be easily identified by modal analysis.
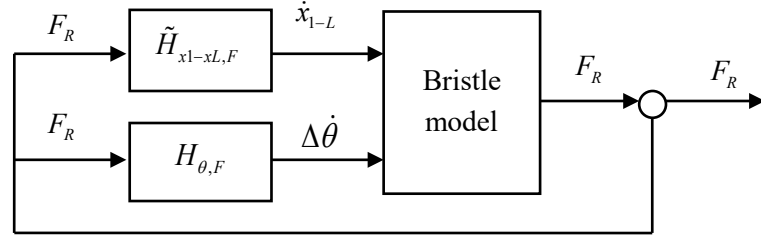
Fig. 5.2: Flow chart of the calculation procedure

5.3   Transfer function identification through modal analysis

In this section, modal analysis is performed to identify the transfer function between the friction force and the velocity of the pad related to the suspension. In practice, the acceleration of the pad instead of its velocity is measured, but the velocity can be obtained by doing time integration of the acceleration. The frequency response function (FRF) is really the transfer function evaluated along the frequency axis [111], which is rewritten as

$$H(\omega) = \frac{\sum_{k=0}^{m} a_k (j\omega)^k}{(j\omega)^n + \sum_{k=0}^{n-1} b_k (j\omega)^k}. \tag{5.13}$$

The way to find the unknown parameters a_k and b_k is equivalent to solve the curve fitting problem such that the error between the analytical expression and the frequency response measurement is minimized over a chosen frequency range [111]. The error between the analytical FRF and measured FRF is

$$e_i = \frac{\sum_{k=0}^{m} a_k (j\omega)^k}{(j\omega)^n + \sum_{k=0}^{n-1} b_k (j\omega)^k} - h_i, \tag{5.14}$$

where h_i is the frequency response measurement at ω_i, which is a complex number. Multiplying $\sum_{k=0}^{n} b_k (j\omega)^k$ in both sides of Eq. (5.14)

$$\tilde{e}_i = e_i \left[\sum_{k=0}^{n-1} b_k (j\omega_i)^k + (j\omega_i)^n \right] = \sum_{k=0}^{m} a_k (j\omega_i)^k - h_i \left[\sum_{k=0}^{n-1} b_k (j\omega_i)^k + (j\omega_i)^n \right]. \tag{5.15}$$

Then, the error vector can be expressed as $\boldsymbol{E} = \begin{bmatrix} \tilde{e}_1 & \dots & \tilde{e}_L \end{bmatrix}^{\mathrm{T}}$. The error vector can be rewritten in a more compact form by expanding each of the summations

$$\boldsymbol{E} = \boldsymbol{PA} - \boldsymbol{TB} - \boldsymbol{W}, \tag{5.16}$$

where

$$P = \begin{bmatrix} 1 & j\omega_1 & (j\omega_1)^2 & ... & (j\omega_1)^m \\ 1 & j\omega_2 & (j\omega_2)^2 & ... & (j\omega_2)^m \\ ... & ... & ... & ... & .... \\ 1 & j\omega_L & (j\omega_L)^2 & ... & (j\omega_L)^m \end{bmatrix}, T = \begin{bmatrix} h_1 & h_1(j\omega_1) & h_1(j\omega_1)^2 & ... & h_1(j\omega_1)^{n-1} \\ h_2 & h_2(j\omega_2) & h_2(j\omega_2)^2 & ... & h_2(j\omega_2)^{n-1} \\ ... & ... & ... & ... & .... \\ h_L & h_L(j\omega_L) & h_L(j\omega_L)^2 & ... & h_L(j\omega_L)^{n-1} \end{bmatrix}$$ (5.17)

$$A = \begin{bmatrix} a_0 & a_1 & ... & a_m \end{bmatrix}^{\mathrm{T}},$$

$$B = \begin{bmatrix} b_0 & b_1 & ... & b_{n-1} \end{bmatrix}^{\mathrm{T}},$$

$$W = \begin{bmatrix} h_1(j\omega_1)^n & h_2(j\omega_2)^n & ... & h_L(j\omega_L)^n \end{bmatrix}^{\mathrm{T}}.$$

The squared error criterion is the squared norm of the error vector

$$\begin{aligned} J &= \|E\|_2^2 = E^{*\mathrm{T}}E \\ &= A^{\mathrm{T}}P^{*\mathrm{T}}PA + B^{\mathrm{T}}T^{*\mathrm{T}}TB + W^{*\mathrm{T}}W \\ &\quad -2\,\mathrm{Re}\left(A^{\mathrm{T}}P^{*\mathrm{T}}TB\right) - 2\,\mathrm{Re}\left(A^{\mathrm{T}}P^*W\right) - 2\,\mathrm{Re}\left(B^{\mathrm{T}}T^{*\mathrm{T}}W\right), \end{aligned}$$ (5.18)

where $\|E\|_2$ is the Euclidian norm. Once the criterion function has a single minimum value, its derivatives with respect to the variables A and B should be zero in the minimum point. Therefore, the following equations exist [111]

$$\frac{\partial J}{\partial A} = 2P^{*T}PA - 2\,\mathrm{Re}\left(P^*TB\right) - 2\,\mathrm{Re}\left(P^{*T}W\right) = 0,$$ (5.19)

$$\frac{\partial J}{\partial B} = 2T^{*T}TB - 2\,\mathrm{Re}\left(T^*PA\right) - 2\,\mathrm{Re}\left(T^{*T}W\right) = 0.$$

The above equations can be written in a compact form

$$\begin{bmatrix} P^{*T}P & -\mathrm{Re}\left(P^*T\right) \\ -\mathrm{Re}\left(T^*P\right) & T^{*T}T \end{bmatrix} \begin{bmatrix} A \\ B \end{bmatrix} = \begin{bmatrix} \mathrm{Re}\left(P^{*T}W\right) \\ \mathrm{Re}\left(T^{*T}W\right) \end{bmatrix}.$$ (5.20)

In this equation, P, T and W are known variables, and A and B are unknown variables. The parameter vectors A and B can be obtained by solving the linear equations (5.20). However, the matrixes P and T are commonly in ill-conditioning and hence Eq. (5.20) is difficult to solve. A method to solve this issue is proposed in [111], where orthogonal polynomials are used to remove the ill-condition.

In order to obtain the frequency response function of the test rig, modal analysis is performed, shown in Fig. 5.3. A modal hammer is knocked on the brake carrier when the disk is rotating under constant speed and brake pressure without stick-slip. The input force $F_{in}(t)$ can be measured by a force sensor. In the meantime, two accelerometers, which are adhered to the brake pad and near the bearing of the suspension, measure the excited accelerations.
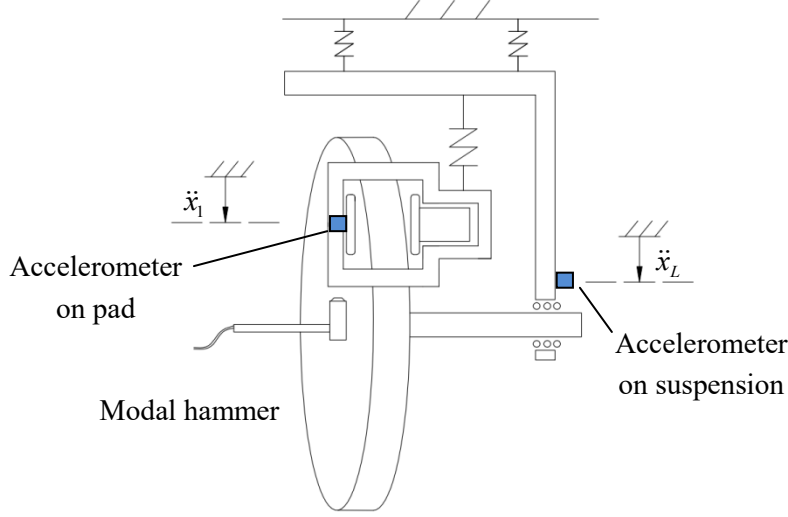
Fig. 5.3: Modal analysis of the test rig with a real brake

The frequency spectra of the velocity on the pad $\dot{x}_1(t)$ and the velocity near the bearing $\dot{x}_L(t)$ are presented in Fig. 5.4 with the red line and the blue line, respectively. As a result, the transfer function $H_{x1-xN,F}$ and $H_{x1-xN,F}$ can be identified as

$$H_{x1-xN,F} = \frac{\mathcal{F}\left(\dot{x}_1(t)\right)}{\mathcal{F}\left(F_{in}(t)\right)}, H_{xL-xN,F} = \frac{\mathcal{F}\left(\dot{x}_L(t)\right)}{\mathcal{F}\left(F_{in}(t)\right)}, \tag{5.21}$$

where $\mathcal{F}(.)$ denotes Fourier transform. It should be noted that in Fig. 5.4 the frequency spectra of $\dot{x}_1(t)$ and $\dot{x}_L(t)$ coincide with each other at frequency 27.5 Hz. After analysis, this frequency is the eigenfrequency of the suspension system, so that the suspension and brake system move synchronously. Since the motion of the suspension will not influence the friction force between the pads and disk, this frequency should be not considered in the calculation of the stick-slip motion. The transfer function between the relative velocity and the friction force $H_{x1-xL,F}$ is expressed as

$$H_{x1-xL,F} = \frac{\mathcal{F}\left(\dot{x}_1(t) - \dot{x}_L(t)\right)}{\mathcal{F}\left(F_{in}(t)\right)}. \tag{5.22}$$

Fig. 5.5 shows the measured FRF of $H_{x1-xL,F}$ with the blue line. Obviously, there is no peak frequency at 27.5 Hz. The transfer function is identified by analyzing the measured FRF according to Eq. (5.20). The FRF of the estimated transfer function with 12 modes is shown in Fig. 5.5 (a) with the red line. It is worth to declare that with 12 modes the estimated FRF has good agreement with the measured FRF. In general, the more modes are used, the better result can be obtained. However, a large number of modes of a system may lead to an over-fitting problem, and may bring some difficulties for the numerical calculation. Therefore, only 4 important modes are chosen to describe the non-rotating parts. The FRF of the estimated transfer function with 4 modes is shown in Fig. 5.5 (b) with the red line. Compared to Fig. 5.5 (a), the error between the estimated and the measured FRF becomes larger. It is well understood that the calculation efficiency can be increased by sacrificing some calculation accuracy by using the reduced-order model. However, since the error between those models is limited, it is more

sensible to use the reduced-order model to save calculation time. The transfer function of the reduced-order model $\tilde{H}_{x1-xL,F}$ is given as

$$\tilde{H}_{x1-xL,F} = \frac{0.01028(j\omega)}{(j\omega)^2 + 150(j\omega) + 3.234 \cdot 10^5} \frac{s}{kg} + \frac{0.07617(j\omega)}{(j\omega)^2 + 359.3(j\omega) + 6.434 \cdot 10^6} \frac{s}{kg} \qquad (5.23)$$

$$+ \frac{0.1334(j\omega)}{(j\omega)^2 + 144.9(j\omega) + 1.432 \cdot 10^7} \frac{s}{kg} + \frac{0.06125(j\omega)}{(j\omega)^2 + 543.7(j\omega) + 1.475 \cdot 10^8} \frac{s}{kg}.$$
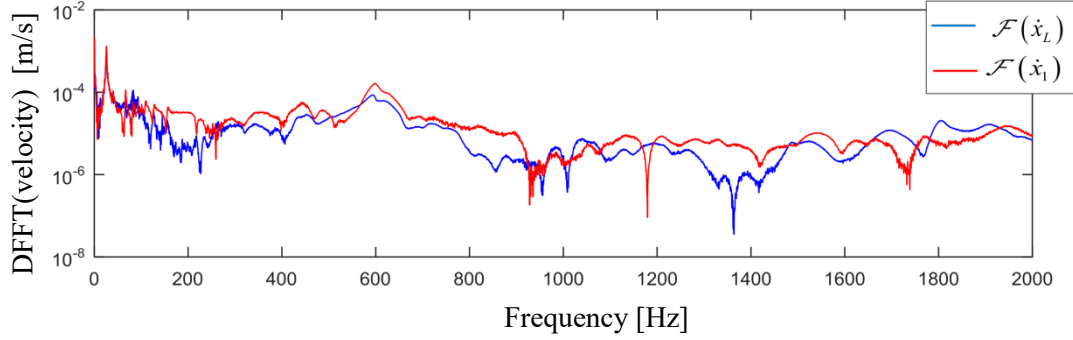
Fig. 5.4: Frequency spectra of the velocities of the pad and suspension
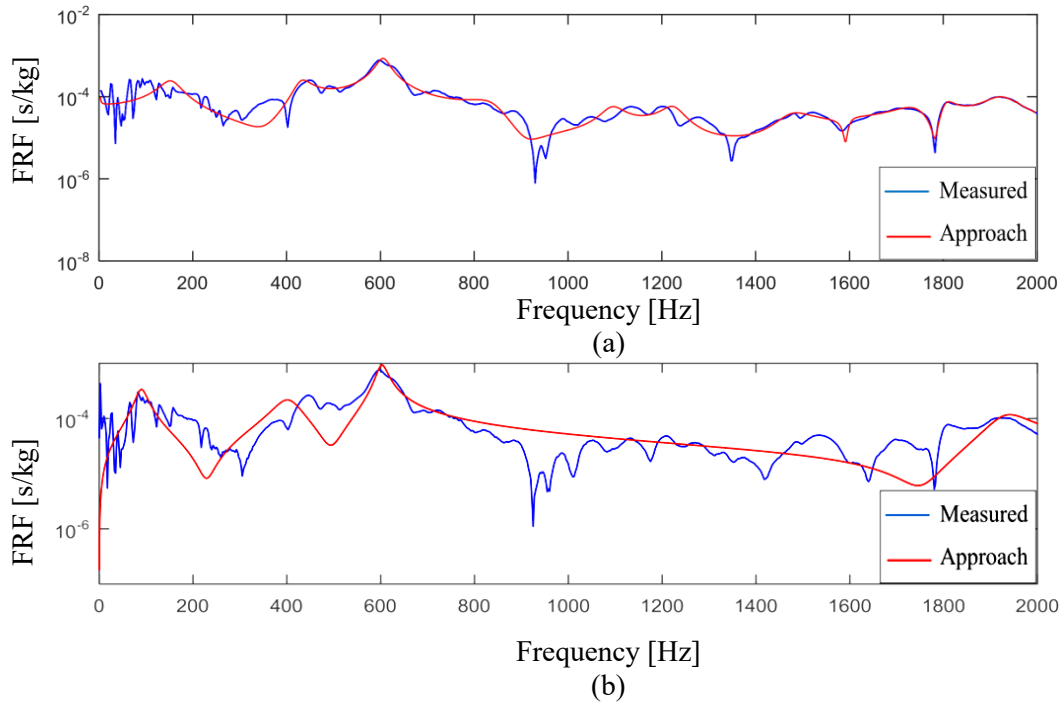

Fig. 5.5: Measured FRF and estimated FRF, (a) approximated with 12 DOFs, (b) approximated with 4 DOFs

5.4 Comparison study of experimental and simulation results

The parameters of the test rig with a real brake should be identified at first. The way to identify the transfer function $\tilde{H}_{x1-xL,F}$ has been presented in section 5.3 and is given in Eq. (5.23). The transfer

function of $H_{\theta,F}$ is easy to measure, since only one mode is considered. The static friction coefficient, the dynamic friction coefficient, the Stribeck velocity, the contact stiffness and contact damping can be identified according to the process proposed in section 4.2. As a result, the parameters of Eq. (5.12) are given in Table 5.1. It should be noticed that the parameters in Table 5.1 are different with the parameters in Table 4.3, since different brake components are used in the test rig with a real brake as that of the idealized brake.

Parameters	Values
$H_{\theta,F}$	$\dfrac{0.15(j\omega)}{0.225(j\omega)^2 + 1.8(j\omega) + 9.38\cdot10^3}\dfrac{\text{s}}{\text{kgm}}$
μ_d	0.335
$\mu_s - \mu_d$	0.03
σ_0	$8.88\cdot10^8\,\text{N/m}$
σ_1	$8.88\cdot10^5\,\text{Ns/m}$
v_s	$0.0547\,\text{m/s}$

Table 5.1: Parameters of the friction law

With parameters to hand, the simulation results are expressed in Figs. 5.6-5.9. The driving speed is 0.31 rad/s and the brake pressure is at 8 bar. Fig. 5.6 shows the measured and simulated torsional angle and torsional velocity of the drive shaft, while the simulated acceleration of the brake pads and the simulated friction force are presented in Fig. 5.7. When the system converts to the slip region from the stick region, the friction force has a sudden change, so that the acceleration shows a large impulse. The same signal can also be observed in the measurements as shown in Fig. 2.12. However, the measured acceleration also exhibits an impulse between the stick and slip region, while the simulation results show only a week impulse. In Fig. 5.8, the frequency spectrum of the torsional velocity of the shaft shows a dominant frequency at 30 Hz and a second frequency at 60 Hz, which is the frequency of the stick-slip motion. The frequency spectrum of the acceleration of the pad shows a lot of frequencies of peak, also at much higher frequencies than the frequency of the stick-slip motion, this vibration is the driver heard or felt during creep groan. Fig. 5.9 exhibits the simulated and measured stick-slip limit cycle in the phase plot with $\Delta\dot\theta$ as a function of $\Delta\theta$, where the simulation results have good agreement with experimental results.

Just as the test rig with an idealized brake, both test rigs can be described by the similar models, which are two linear systems coupled by a nonlinear friction law. Therefore, the limit cycle obtained from those models are qualitatively same. However, the test rig with a real brake is much more complex than that of the idealized brake, so that a model with more DOFs is required to describe the vibration of the carrier. The question will be if the proposed model still works for a real vehicle. The answer seems to be yes, because the stick-slip motion is related to the velocity of the pad referring to the suspension, i.e. the stick-slip motion is only related to the isolated brake-suspension sub-system. Therefore, the stick-slip motion will be the same no matter whether the suspension is assembled in the frame or assembled in the chassis of a vehicle. However, even though the stick-slip motion is un-

changed, the generated creep groan will be different if the chassis of a vehicle is considered, since the vibration of the chassis can also be excited by the varied friction force. As a conclusion, the proposed model in Eq. (5.12) also works for a real vehicle. The stick-slip motion only relates to the brake-suspension sub-system, but creep groan noise will be influenced by the other components of a vehicle, such as the chassis, the axle and so on.
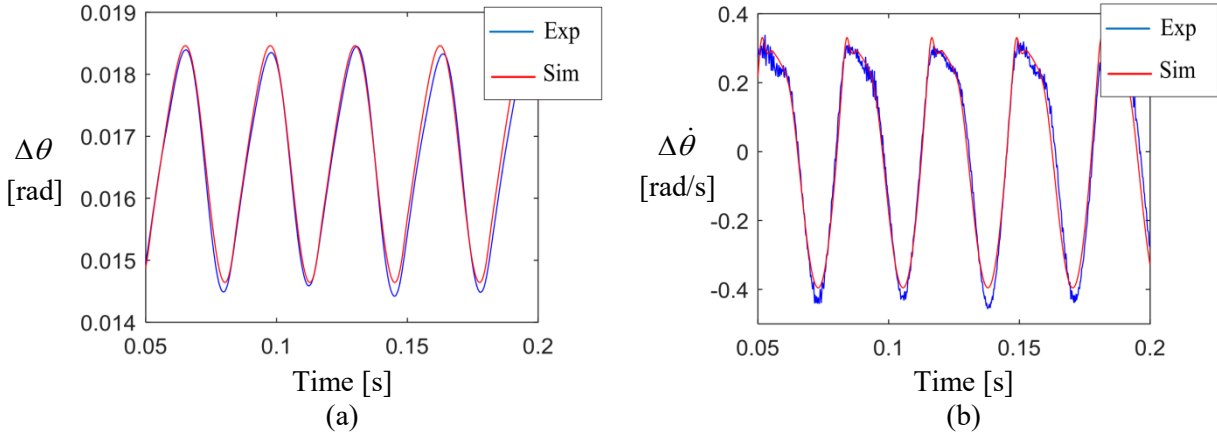

Fig. 5.6: Experimental and simulated torsional angle (a) and torsional velocity (b) of the shaft
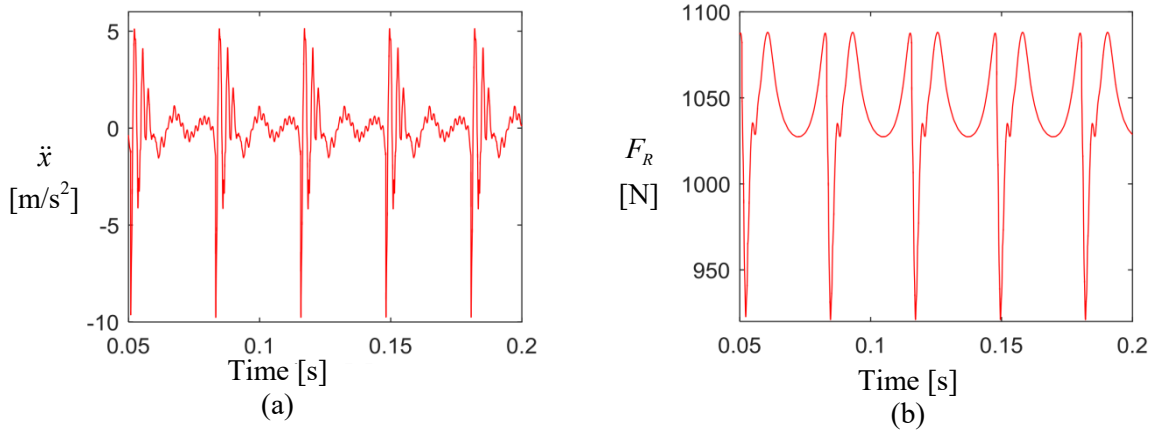

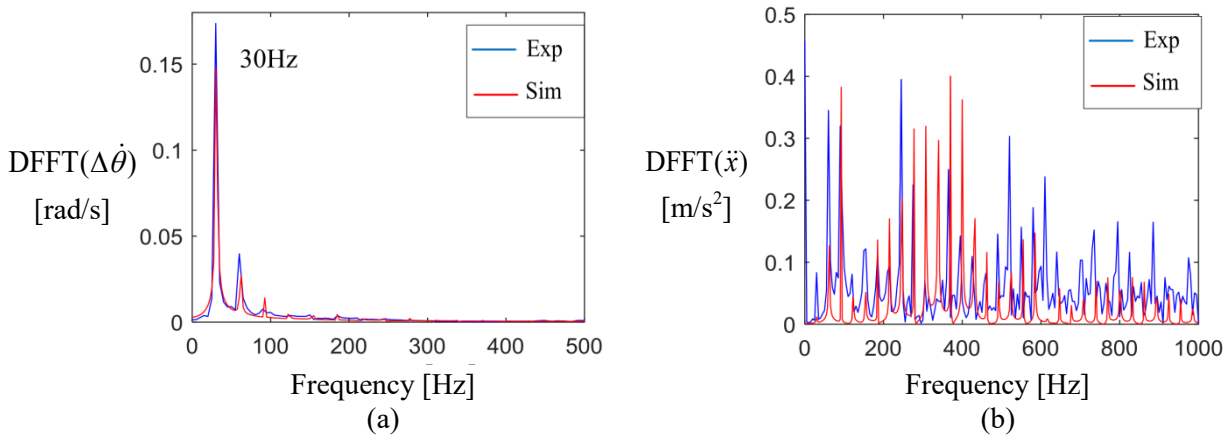Fig. 5.7: Simulated acceleration of the pad (a) and the simulated friction force (b)

Fig. 5.8: Frequency spectra of torsional velocity of the shaft (a) and acceleration of the pad (b)

In order to study the existence condition of creep groan, the stability of the solution is proposed as follows. At first, the transfer function $\tilde{H}_{x1-xL,F}$ is converted to the state space function

$$I_p \ddot{X}_p + D_p \dot{X}_p + K_p X_p = B_p F_R,$$

(5.24)

$$\dot{x}_{1L} = \sum_{i=1}^{L_R} \dot{x}_i, D_p = \mathrm{diag}\left([.... \quad d_i \quad ...]\right), K_p = \mathrm{diag}\left([.... \quad k_i \quad ...]\right),$$

$$B_p = [.... \quad \alpha_i \quad ...]^{\mathrm{T}}, X_p = [... \quad x_i \quad ...]^{\mathrm{T}}, (i=1,2,....,L_R).$$

Then, the equivalent position of Eq. (5.12) is given as

$$\Delta\theta_{eq} = r\left(N\mu_d + N(\mu_s - \mu_d)e^{-\Omega_0 r/v_s}\right)/k_\theta, \Delta\dot{\theta}_{eq} = 0,$$

(5.25)

$$X_{p,eq} = \left(N\mu_d + N(\mu_s - \mu_d)e^{-\Omega_0 r/v_s}\right)K_p^{-1}, \dot{X}_{p,eq} = 0, z_{eq} = \left(N\mu_d + N(\mu_s - \mu_d)e^{-\Omega_0 r/v_s}\right)/\sigma_0.$$

The stability of the equilibrium solution of Eq. (5.12) is obtained by analyzing the eigenvalue of the linearized system under its equilibrium position

$$\dot{Y} = AY,$$

$$Y = \begin{bmatrix} \Delta\theta & \Delta\dot{\theta} & X_p & \dot{X}_p & z \end{bmatrix}^{\mathrm{T}},$$

$$A =$$

$$\begin{bmatrix}
0 & 1 & \mathbf{0}_{1 \times L_R} & \mathbf{0}_{1 \times L_R} & 0 \\
-\dfrac{k_\theta}{I} & -\dfrac{d_\theta}{I} + \dfrac{r\sigma_1}{I}\dfrac{\partial\phi(\Delta\dot{\theta},\dot{X}_p,z)}{\partial\Delta\dot{\theta}} & \mathbf{0}_{1 \times L_R} & \dfrac{r\sigma_1}{I}\dfrac{\partial\phi(\Delta\dot{\theta},\dot{X}_p,z)}{\partial\dot{X}_p} & \dfrac{r}{I}\left(\sigma_0 + \sigma_1\dfrac{\partial\phi(\Delta\dot{\theta},\dot{X}_p,z)}{\partial z}\right) \\
\mathbf{0}_{L_R \times 1} & \mathbf{0}_{L_R \times 1} & \mathbf{0}_{L_R \times L_R} & \mathbf{I}_{L_R \times L_R} & \mathbf{0}_{L_R \times L_R} \\
\mathbf{0}_{L_R \times 1} & B_p\sigma_1\dfrac{\partial\phi(\Delta\dot{\theta},\dot{X}_p,z)}{\partial\Delta\dot{\theta}} & -K_p & -D_p + B_p\sigma_1\dfrac{\partial\phi(\Delta\dot{\theta},\dot{X}_p,z)}{\partial\dot{X}_p} & B_p\left(\sigma_0 + \sigma_1\dfrac{\partial\phi(\Delta\dot{\theta},\dot{X}_p,z)}{\partial z}\right) \\
0 & \dfrac{\partial\phi(\Delta\dot{\theta},\dot{X}_p,z)}{\partial\Delta\dot{\theta}} & \mathbf{0}_{1 \times L_R} & \dfrac{\partial\phi(\Delta\dot{\theta},\dot{X}_p,z)}{\partial\dot{X}_p} & \dfrac{\partial\phi(\Delta\dot{\theta},\dot{X}_p,z)}{\partial z}
\end{bmatrix}$$

(5.26)

with

$$\frac{\partial\phi(\Delta\dot{\theta},\dot{X}_p,z)}{\partial\Delta\dot{\theta}} = \frac{(\mu_s - \mu_d)r^2\Omega_0}{v_s(\mu_s - \mu_d + \mu_d e^{\Omega_0 r/v_s})},$$

$$\frac{\partial\phi(\Delta\dot{\theta},\dot{X}_p,z)}{\partial z} = \frac{-r\sigma_0\Omega_0}{N\mu_d + N(\mu_s - \mu_d)e^{-\Omega_0 r/v_s}},$$

$$\frac{\partial\phi(\Delta\dot{\theta},\dot{X}_p,z)}{\partial\dot{X}_p} = \begin{bmatrix} \dfrac{(\mu_s - \mu_d)r\,\Omega_0}{v_s(\mu_s - \mu_d + \mu_d e^{\Omega_0 r/v_s})} & 0...0 & -\dfrac{(\mu_s - \mu_d)r\,\Omega_0}{v_s(\mu_s - \mu_d + \mu_d e^{\Omega_0 r/v_s})} & 0...0 \end{bmatrix},$$

where A is the corresponding system matrix. The stability of the equilibrium solution can be analyzed by studying the eigenvalues of A. If the real parts of all eigenvalues are negative, the equilibrium solution is asymptotically stable. If any of the real parts of the eigenvalues is positive, the equilibrium solution is unstable, and the solution will show increasing amplitudes. The stick-slip limit cycle of the test rig with a real brake can be calculated by performing numerical integration based on Eq. (5.12). If

the system has no stick-slip limit cycle, the system reaches its equilibrium solution with the initial condition in the stick region. Otherwise, the stick-slip limit cycle is reached.
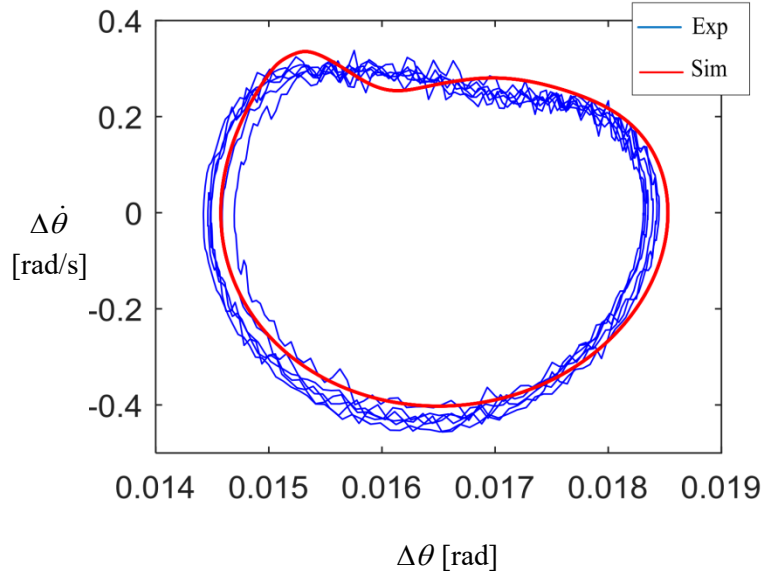
Fig. 5.9: Simulated and measured stick-slip limit cycle

According to the conditions for the existence of the stick-slip limit cycle and the stability of the equilibrium solution, the system shows three different regions with different types of solutions. Fig. 5.10 shows the simulated map of creep groan with the estimated parameters. It is similar to the map of creep groan for the idealized brake shown in Fig. 4.9.
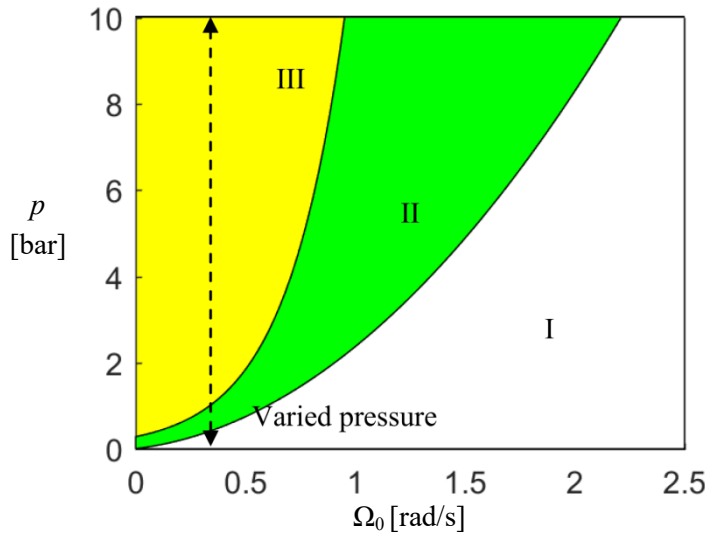
Fig. 5.10: Simulated map of creep groan of the real brake

Experiments are carried out to confirm the existence of the three regions, where the driving speed of the motor is constant (0.31 rad/s) and the brake pressure is varied. Corresponding experimental results are shown in Fig. 5.11. The red line describes the brake pressure, while the blue line shows the torsional vibration angle $\Delta \tilde{\theta}$ of the drive shaft. When the brake pressure increase slowly from 0 bar to 5 bar, the system has no creep groan at low pressure, but creep groan occurs when the pressure is higher than a critical pressure p_{c23} (2 bar). After that, the pressure is slowly decreased from 5 bar to 0 bar. Creep groan occurs at high pressure and disappears when the pressure is lower than another critical

pressure p_{c12} (1.2 bar). The difference between critical pressure in fact proofs the existence of three regions of the system.

Fig. 5.12 shows the equilibrium solution and the limit cycle of the brake system with different pressure in the phase plot with $\Delta\dot{\tilde{\theta}}$ as a function of $\Delta\tilde{\theta}$. When the pressure is lower than p_{c12}, only the equilibrium solution can be measured both in the pressure-increasing and pressure-decreasing processes, meaning that the system is in region I and creep groan cannot occur. When the pressure is higher than p_{c23}, creep groan is measured in both processes, meaning that the system is in region III and creep groan always occurs in this region. When the pressure is lower than p_{c23} but higher than p_{c12}, creep groan is measured in the pressure-decreasing process, but not in the pressure-increasing process, meaning that the system is in region II.
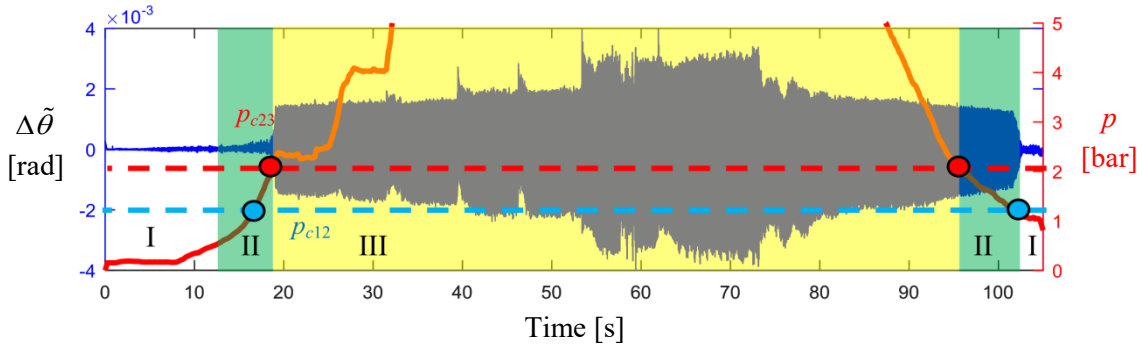
Fig. 5.11: Torsional vibration angle with varied brake pressure, the red and blue points represent the measured boundary pressure between the three regions.
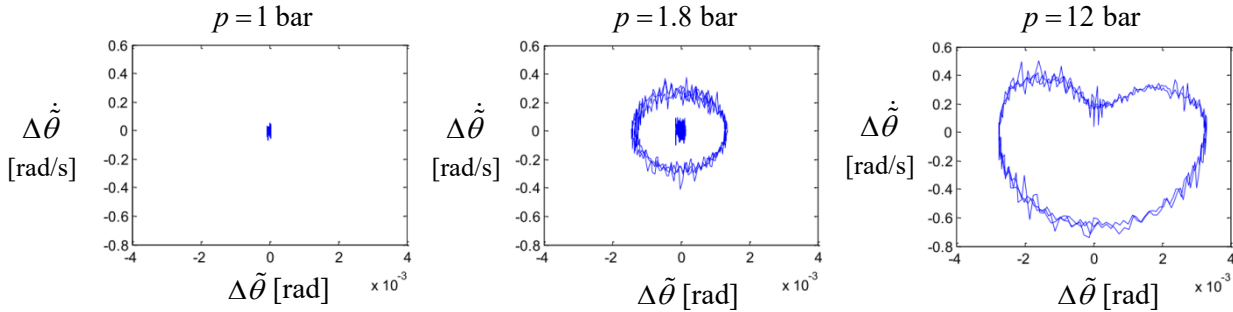
Fig. 5.12: Equilibrium solution and stick-slip limit cycle under different pressure

In the rest part of this section, an experimental method is proposed to identify the map of creep groan of the brake system. The detailed steps are given as follows. At a constant speed $\Omega_{c0,i}$, the brake pressure is increased from 0 bar. The system is in its equilibrium solution at low brake pressure. If the pressure is higher than a critical value $p_{c23,i}$, creep groan will occur. At this moment, the speed as well as the brake pressure is recorded as a boundary point $\begin{bmatrix} \Omega_{c0,i} & p_{c23,i} \end{bmatrix}$ in the velocity-pressure map with a triangle. Once creep groan occurs in the system, the brake pressure is slowly decreased until the disappearance of creep groan. Meanwhile, the boundary point is recorded as $\begin{bmatrix} \Omega_{c0,i} & p_{c12,i} \end{bmatrix}$ in the velocity-pressure map with a cycle.

Furthermore, the driving speed is changed to $\Omega_{c0,i+1}$ and find the corresponding boundary points $\begin{bmatrix} \Omega_{c0,i+1} & p_{c23,i+1} \end{bmatrix}$ as well as $\begin{bmatrix} \Omega_{c0,i+1} & p_{c12,i+1} \end{bmatrix}$. Repeating this process, the boundary points under different speeds can be measured. It is possible to find a polynomial regression that fits the data set $\begin{bmatrix} \Omega_{c0,i} & p_{c12,i} \end{bmatrix}$, $i = 1, 2, ..., N$. This curve is the boundary between regions I and II. It is also possible to find a polynomial regression that fits the data set $\begin{bmatrix} \Omega_{c0,i} & p_{c23,i} \end{bmatrix}$, $i = 1, 2, ..., N$. This curve is the boundary between regions II and III. As a result, the boundaries of regions I, II and III can be obtained by experimental analysis, shown in Fig. 5.13 (Similar results have been published in [33]). Compared to the simulated map of creep groan in Fig. 5.10, the measured map shows the similar behavior with the simulated one.
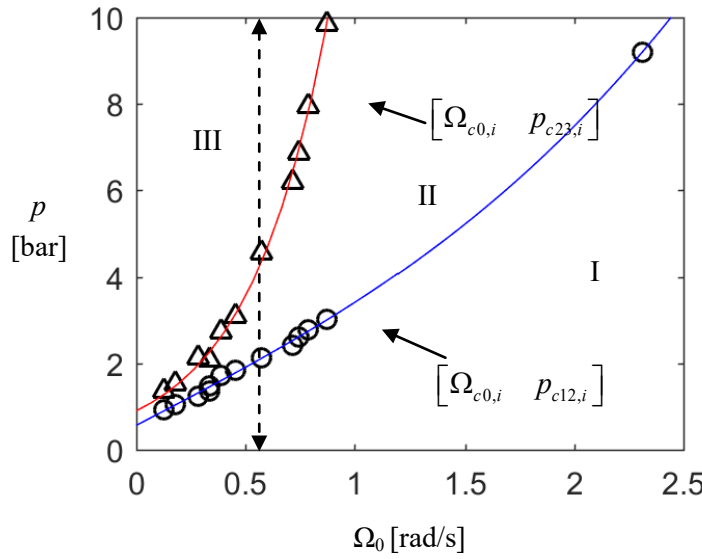
Fig. 5.13: Map of creep groan identified by experiments, the triangles represent the measured boundary points between regions II and III, while the cycles represent the measured boundary points between region I and II; the red line and the blue line are the polynomial regression curves of the measured boundary points

During the pressure-increasing process, the vibration amplitude of the drive shaft increases with the brake pressure, shown in Fig. 5.14 (a). By doing SFFT of $\Delta\dot{\theta}$ (using Hamming window with window size 0.5s) as shown in Fig. 5.14 (b), one can see that the frequency of the stick-slip motion decreases with increasing of the brake pressure. Meanwhile, the amplitudes of the acceleration of the pad $\ddot{x}_1$ increases with the brake pressure, shown in Fig. 5.14 (c). The SFFT of $\ddot{x}_1$ is shown in Fig. 5.14 (d), and the frequency of $\ddot{x}_1$ changes with the brake pressure.

Similarly, during the accelerating process, the vibration amplitude of the drive shaft is increased with the speed, shown in Fig. 5.15 (a). The frequency of the stick-slip motion increases with the speed, and approaches the eigenfrequency of the disk-shaft sub-system, shown in Fig. 5.15 (b). In Fig. 5.15 (c), the amplitude of the acceleration of the pad $\ddot{x}$ is almost not influenced by the speed. The SFFT of $\ddot{x}$ is presented in Fig. 5.15 (d), and the speed has almost no influence on the vibration frequency of the pad.
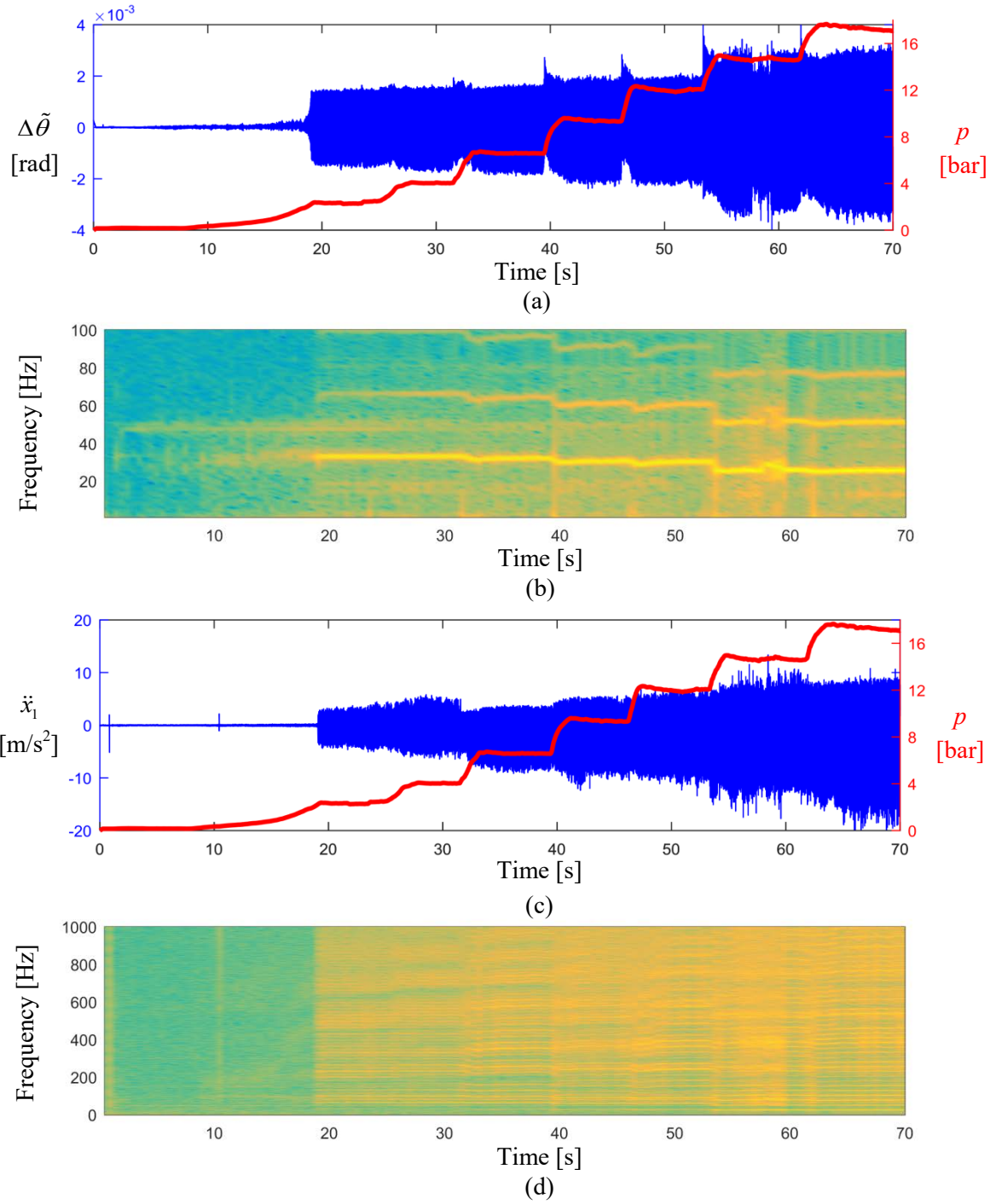
Fig. 5.14: Measured signals during pressure-increasing process, (a) vibration of the torsional angle $\Delta\tilde{\theta}$ with increasing brake pressure, (b) SFFT of $\Delta\dot{\tilde{\theta}}$, (c) acceleration of the pad with increasing brake pressure, (d) SFFT of $\ddot{x}$.
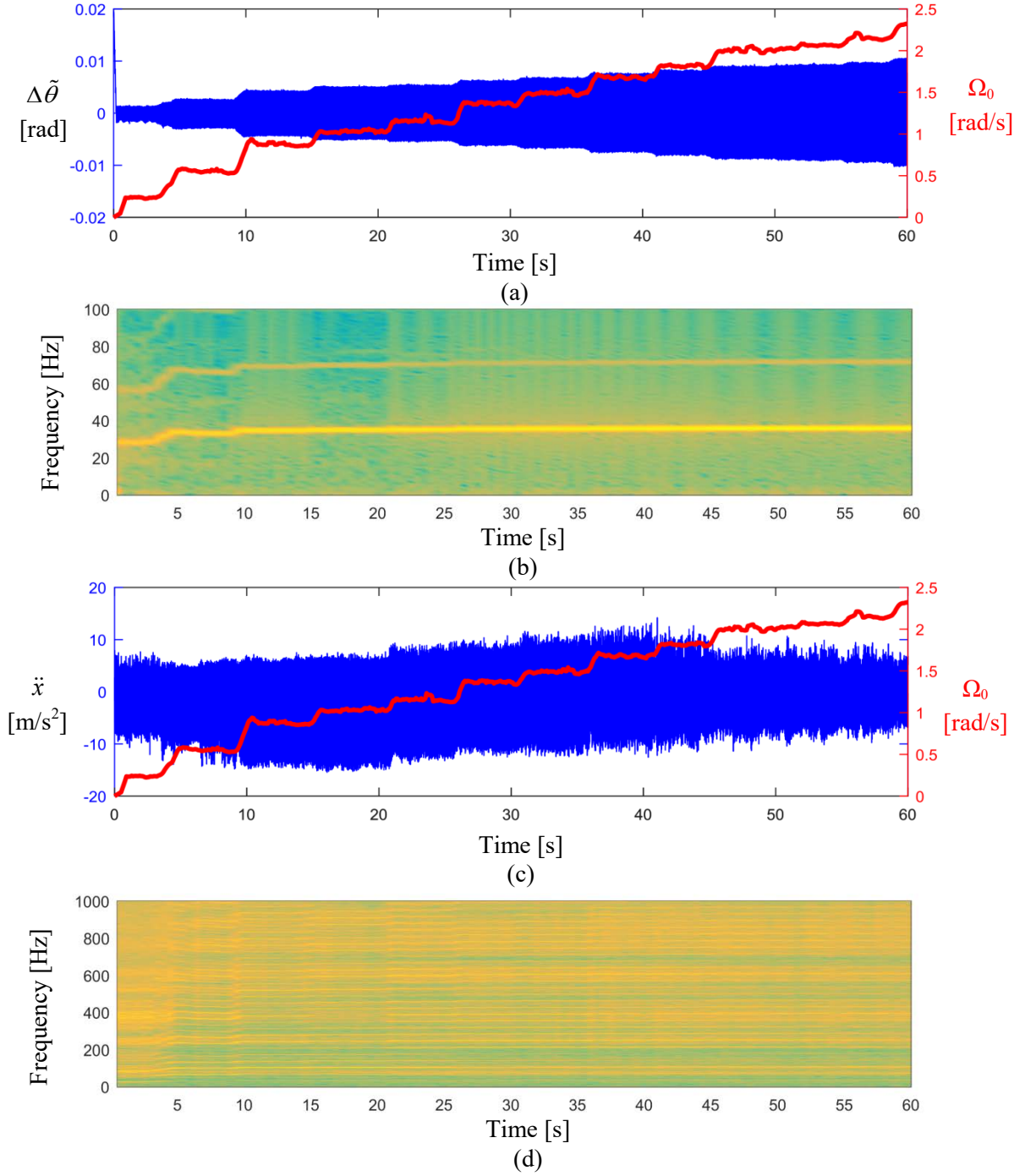
Fig. 5.15: Measured signals during accelerating process, (a) vibration of the torsional angle $\Delta\tilde{\theta}$ with increasing speed, (b) SFFT of $\Delta\dot{\tilde{\theta}}$, (c) acceleration of the pad with increasing speed, (d) SFFT of $\ddot{x}$.

5.5 Summary

In this chapter, theoretical and experimental investigations of creep groan on a test rig with a real brake are carried out. According to the analysis of the dynamic model, it is possible to isolate the brake-suspension system from the frame, the axle, and the chassis for the study of the stick-slip motion. Therefore, complex components such as the chassis can be at first ignored.

In order to analyze creep groan in such test rig efficiently, a reduced-order model is proposed by ignoring the relative unimportant modes. The advantages of the reduced-order model are that it requires only system parameters and it has high computational efficiency.

Modal analysis is carried out to identify parameters of the test rig with a real brake. Based on the identified transfer function, the simulated results are compared with the experimental results quantitatively. Both results have good agreement with each other. It is confirmed that the reduced-order model is of efficiency to describe creep groan of the brake system.

Furthermore, a map of creep groan is obtained by stability analysis of the equilibrium solution and stick-slip limit cycle. Additionally, this map is measured through an experimental method. The measured and calculated maps show the similar behavior.

6 Countermeasures against creep groan

After understanding the mechanism of creep groan, different methods against creep groan are discussed in this chapter. At first, a pad, which contains piezoceramic staple actuators [112], is used to suppress creep groan. Then, damping materials are added between the shaft and disk to suppress creep groan. Furthermore, during the accelerating process, a skillful driver can employ the cadence braking technique to decrease the time of creep groan. Inspired by the optimal braking technique, a control loop is designed and integrated into an anti-lock braking system to prevent creep groan.

6.1 Suppression of creep groan through a active pad

It is a well-known effect that vibration can influence frictional contacts see e.g. [47], [57]-[61], [80], [81]. Therefore, a pad, which contains piezoceramic staple actuators, is applied to eliminate creep groan of the brake system. Von Wagner *et al.* have successfully used such "smart pads" for the active suppression of brake squeal via optimal control [112], [113]. As an extension of this work, similar active pads are used to suppress creep groan in this thesis. In this case, creep groan can be eliminated by giving an external vibration at a constant frequency via the active pad.

At the beginning of this section, the Prandtl-Tomlinson model is studied to understand the frictional mechanism on the atomic scale [78]. The Prandtl-Tomlinson model describes a sharp tip scanning a corrugated surface at a constant normal force in nanotribology, and the friction force is generated by the torsional bending of the cantilever which the tip is mounted on. The way to calculate the static friction on the atomic scale is given in [80]. Assuming that the corrugated surface has sinusoidal surface potential with amplitude E_0 and periodicity a, the potential energy V_{int} of the system is

$$V_{int} = -\frac{E_0}{2}\cos\left(2\pi\frac{x_t}{a}\right) + \frac{1}{2}k_t\left(x_t - x_s\right)^2, \tag{6.1}$$

where the pulling spring with stiffness k_t is extended between the position of the tip x_t and the moving tip x_s. If the tip moves slowly, it always resides in a minimum of the effective potential. The condition of the minimum of the effective potential is $\partial V_{int}/\partial x_t = 0$ [80]

$$\frac{\partial V_{int}}{\partial x_t} = \frac{\pi E_0}{a}\sin\left(2\pi\frac{x_t}{a}\right) + k_t(x_t - x_s). \tag{6.2}$$

The pulling force F_L is equal to the force in the spring if ignoring the damping and acceleration of the tip. With $F_L = k_t(x_t - x_s)$, it follows that

$$F_L = -\frac{\pi E_0}{a}\sin\left(2\pi\frac{x_t}{a}\right). \tag{6.3}$$

The corrugation of the surface potential E_0 is linearly related to the maximum lateral force F_L, the maximum of the absolute value of the force F_L is found at $x_t = a/4$. It is obtained

$$F_L = \frac{\pi E_0}{a}, \tag{6.4}$$

where F_L is considered as the static friction force, which is the minimum force to let the tip jump out the energy barrier of height $\pi E_0 / a$. The static friction coefficient is therefore given as

$$\mu_{s,0} = \frac{\pi E_0}{a F_N}, \tag{6.5}$$

where F_N is the normal force.

If a mechanical vibration f is added in the out-of-plane direction of the disk, the oscillation causes the variation of the normal force F_N and the energy corrugation E_0. It is assumed that the corrugation energy changes with time as $E(t) = E_0(1 + \alpha \cos 2\pi f t)$ when the normal oscillation acts on the lateral tip motion, where α is a scale associated to the amplitude of the vibration. If $f \gg \dot{x}_s / a$, the tip reaches the minimum corrugation $E_0(1 - \alpha)$ many times when the tip slowly moves on the surface [81]. It means that the surface potential energy under mechanical vibration can be expressed as $E_0(1 - \alpha)$, then

$$F_L = \frac{\pi E_0(1 - \alpha)}{a}. \tag{6.6}$$

As a result, the static friction coefficient under mechanical vibration is expressed as

$$\mu_s = \mu_{s,0}(1 - \alpha). \tag{6.7}$$

Obviously, the static friction coefficient is decreased with increasing α. The dynamic coefficient will not change until the tip separates from the surface.
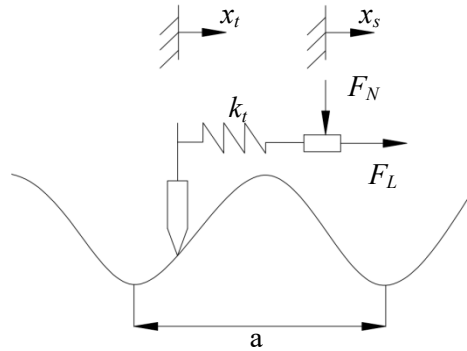
Fig. 6.1: Prandtl-Tomlinson model [78]

A pad with integrated piezoceramics manufactured at MMD TU Berlin provides high frequency excitation in the out-of-plane direction, which is similar to the pad used in [112]. This pad contains two piezoelectric layers with an electrode layer between them, shown in Fig. 6.2. A signal generator can produce a sine form voltage with frequency from 1 Hz to 100 kHz. A signal amplifier is utilized for the voltage amplification. Then the excitation voltage is

$$U = U_p \sin 2\pi f_0 t, \tag{6.8}$$

where U_p is the amplitude of the voltage, and f_0 is its frequency.

There are numerous publications on active influencing frictional contacts [47], [57]-[61], [80], [81], but author is to the best of his knowledge not aware of the prior usage of such active pads for the suppression of creep groan so far. In order to suppression of creep groan, the active pad is assembled to the carrier as shown in Fig. 6.3 (a). According to the above analysis, it is possible to decrease the static friction coefficient by giving a high frequency mechanical vibration in the out-of-plane direction via the active pad. Creep groan can therefore be eliminated when the static friction coefficient is less than some critical value. Experiments are performed to confirm this statement. The frequency of the external variation is chosen in such a way that, on the one hand, the frequency should be one of eigenfrequencies of the caliper to maximize the amplitude of the external vibration. On the other hand, it should be higher than the human limits of hearing to avoid additional noise. As a result, the frequency 20 kHz is chosen which fulfills both requirements.
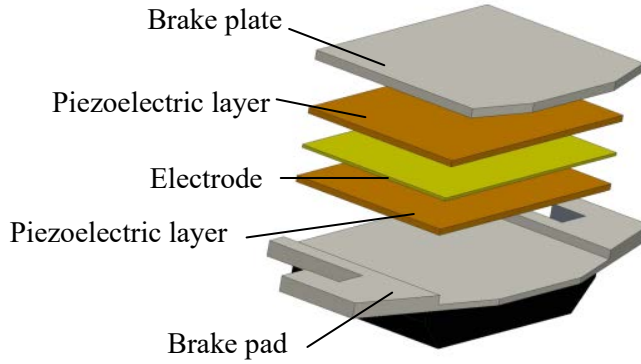
Fig. 6.2: Construction of the active pad
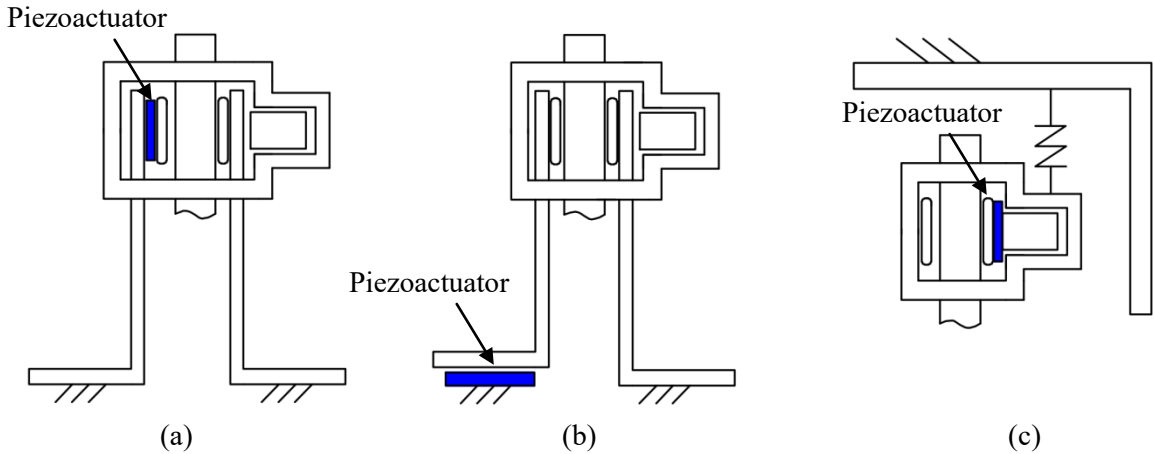
Fig. 6.3: Location of the piezoceramic actuator, (a) active pad in the idealized brake, (b) active carrier, (c) active pad in the real brake

The speed of the motor is set as 0.2 rad/s and the brake pressure is given as 6 bar. Under this condition the system is in region III and creep groan will always occur without external excitation. The measurement is started when a stable stick-slip limit cycle is observed in the system. In Fig. 6.4, the vibration of the shaft $\Delta\tilde{\theta}$ is exhibited with a blue line, while the driving voltage U_p is shown as a red

line. It is noticed that the amplitude of the creep groan decreases with the increase of the voltage. Once the voltage is larger than another critical value U_{c1}, creep groan is eliminated. The reason is that the system shifts into region I due to the decrease of the static friction coefficient. This experiment confirms that creep groan can be eliminated by adding an external vibration in the out-of-plane direction.

Furthermore, if the voltage is decreased and lower than a critical value U_{c2}, creep groan appears again. The reason is that the system returns to region III due to the increase of the static friction coefficient. U_{c2} is lower than U_{c1}, which also confirms the existence of region II with both stable equilibrium solution and limit cycle.

Fig. 6.5 shows the equilibrium solution and stick-slip limit cycle of the system. If the driving voltage is lower than U_{c2}, the system is in region III and the stick-slip limit cycle is the only stable solution of the system. If the driving voltage is higher than U_{c1}, the system is in region I and the stick-slip limit cycle does not exist. If the driving voltage is between U_{c1} and U_{c2}, the system is in region II and the occurrence or absence of creep groan depends on its initial condition. Therefore, the stick-slip limit cycle can be observed in the voltage-increasing process in region II, while the equilibrium solution can be observed in the voltage-decreasing process.
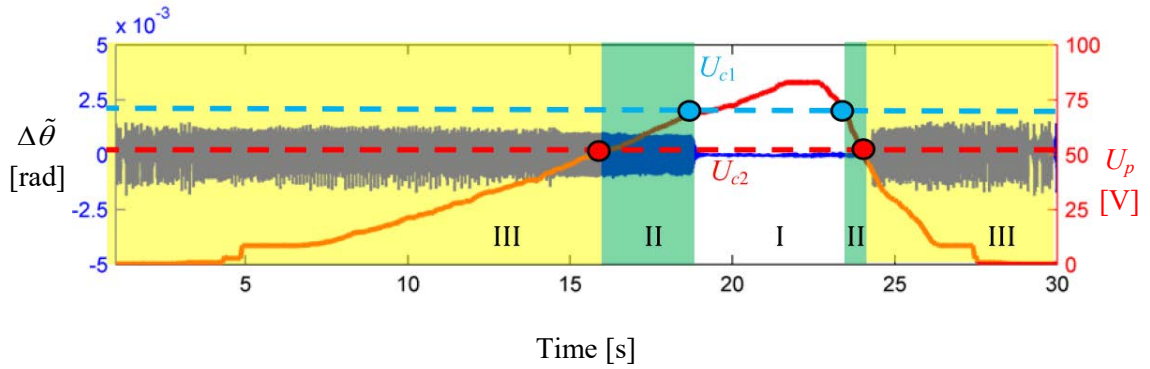
Fig. 6.4: Suppression of creep groan by adding an external excitation in the out-of-plane direction of the disk, the blue points are the critical voltage that creep groan disappears, while the red points are the critical voltage that creep groan appears again.
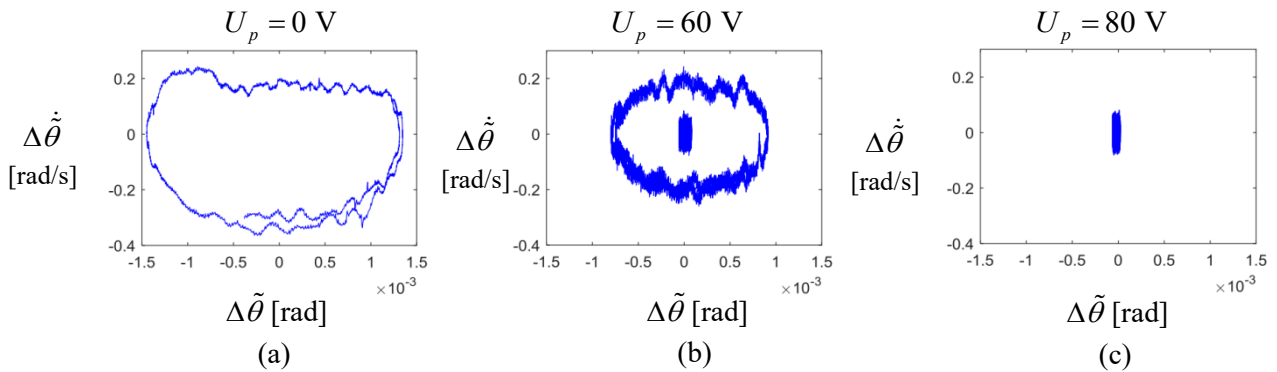
Fig. 6.5: Equilibrium solution and limit cycle with different amplitude of voltage, (a) system in region III, (b) system in region II, (c) system in region I

Furthermore, a mechanical vibration added in the in-plane direction of the disk will be considered. In this case, the oscillation will change the position of x_t. According to the Ref. [58], Eq. (6.3) becomes

$$F_L = -\frac{\pi E_0}{a} \sin\left[\frac{2\pi}{a}\left(x_t + \beta \sin\left(2\pi f_0 t\right)\right)\right], \tag{6.9}$$

where β is a scalar associated to the amplitude of the in-plane vibration. Integrating Eq. (6.9) with a period $T = 1/f_0$

$$\begin{aligned} F_L &= -\frac{\pi E_0}{a} \int_0^{1/f} \sin\left[\frac{2\pi}{a}\left(x_t + \beta \sin\left(2\pi ft\right)\right)\right] dt \\ &= -\frac{\pi E_0}{a} \sin\left(\frac{2\pi}{a} x_t\right) \int_0^{1/f} \cos\left(\beta \sin\left(2\pi ft\right)\right) dt - \frac{\pi E_0}{a} \cos\left(\frac{2\pi}{a} x_t\right) \int_0^{1/f} \sin\left(\beta \sin\left(2\pi ft\right)\right) dt. \end{aligned} \tag{6.10}$$

The mean value of the second term is equal to 0, since it is an odd function. The mean value of the first term can be calculated with the help of the Bessel-function [58]

$$F_L = -\frac{\pi E_0}{a} \sin\left(\frac{2\pi}{a} x_t\right) J_0(\beta), \tag{6.11}$$

where J_0 is the Bessel function of the first kind. The maximum value of Eq. (6.11) is

$$F_L = \left| -\frac{\pi E_0}{a} \sin\left(\frac{2\pi}{a} x_t\right) J_0(\beta) \right|_{\max} = \frac{\pi E_0}{a} J_0(\beta), \tag{6.12}$$

where F_L is the static friction force. As a result, the static friction coefficient is

$$\mu_s = J_0(\beta)\mu_{s,0}. \tag{6.13}$$

Therefore, the static friction coefficient is decreased with increasing β. In order to confirm the above analysis, a piezoceramic actuator is assembled under the short edge of the L-shaped steel plate which constitutes an active carrier, shown in Fig. 6.3 (b). The voltage of the piezoceramic actuator is given as $U = U_p \sin 2\pi f_0 t$. After test, it is found that creep groan can be eliminated when the frequency of the voltage is 8 kHz, which is one of the eigenfrequencies of the carrier. The operation condition is at the brake pressure 10 bar with the speed 0.3 rad/s. Experimental results are presented in Fig. 6.6. At the beginning, the system is in the region III and creep groan occurs without external excitation. It is obvious that creep groan is eliminated when the piezoceramic actuator turns on. Once the piezoceramic actuator turns off, creep groan appears again.

It should be noted that the active carrier has disadvantages compared to the active pad: The vibration source is far from the contact surface; it is hard to add a piezoceramic actuator in a real brake carrier due to its compact structure.
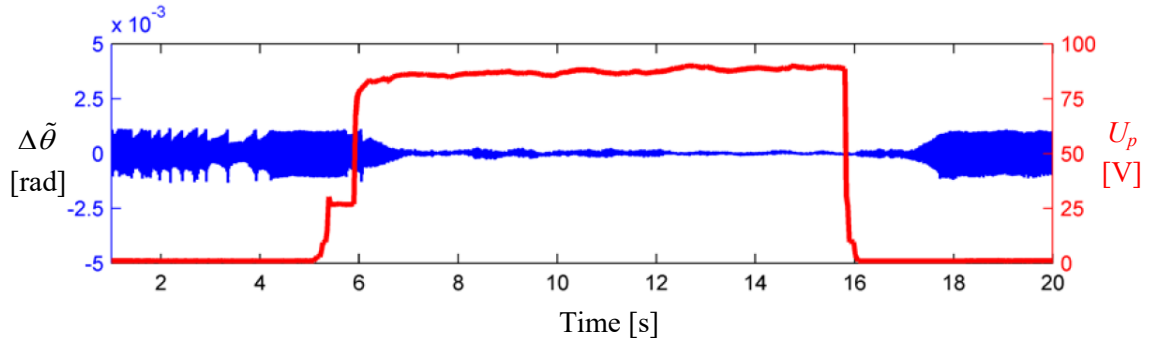
Fig. 6.6: Suppression of creep groan by an external excitation in the in-plane direction of the disk

Therefore, the active pad is employed in the test rig with a real brake against creep groan. Once this technique is successfully performed in the test rig with a real brake, it can be considered to use in a real vehicle. An active pad is assembled in the piston side of the caliper as shown in Fig. 6.4 (c). The speed of the motor is set as 0.2 rad/s and the brake pressure is given as 6 bar. Under this condition the system is in region III and creep groan occurs without external excitation. In the first experiment, the amplitude of the voltage is kept constant and its frequency is changed. The voltage of piezoceramic actuator is set as 70 V and varies from 10 kHz to 20 kHz. Experiment results are exhibited in Fig. 6.7, where the red line presents the frequency of the voltage and the blue line shows the vibration of the torsional angle of the shaft. The vibration amplitude of the shaft varies with the frequency and has the minimum value at 15.8 kHz and 16.5 kHz, which are eigenfrequencies of the caliper. The external vibration has the maximum amplitude under those frequencies, so that the static friction coefficient has the minimum value.

In the second experiment, the frequency of the voltage is set as 15.8 kHz, and the amplitude of the voltage is slowly increased from 0 V to 100 V. In Fig. 6.8, the stick-slip vibration $\Delta\tilde{\theta}$ is exhibited with a blue line, and the amplitude of the voltage is shown as a red line. The system has creep groan when the voltage equals to 0. The vibration amplitude of the shaft decreases with increasing the amplitude of the voltage. Once the voltage is larger than a critical value, creep groan is eliminated. If the amplitude of the voltage is decreased, creep groan occurs again.

For a conventional active noise cancellation method, a feedback control loop is required [112]. In order to guarantee the stability of feedback control as well as good control performance of the control loop, lots of work is required and the corresponding hardware is generally expensive. In contrast, the proposed active pad system is easier and cheaper.
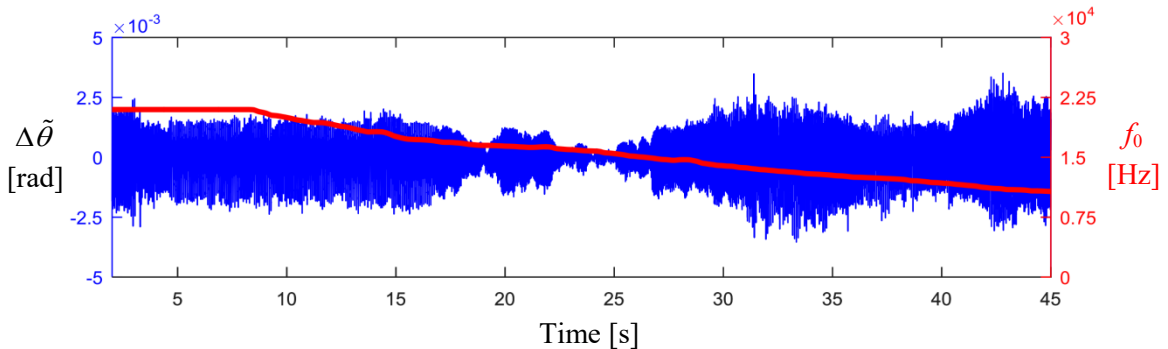
Fig. 6.7: Suppression of creep groan by an external excitation with varied voltage frequency
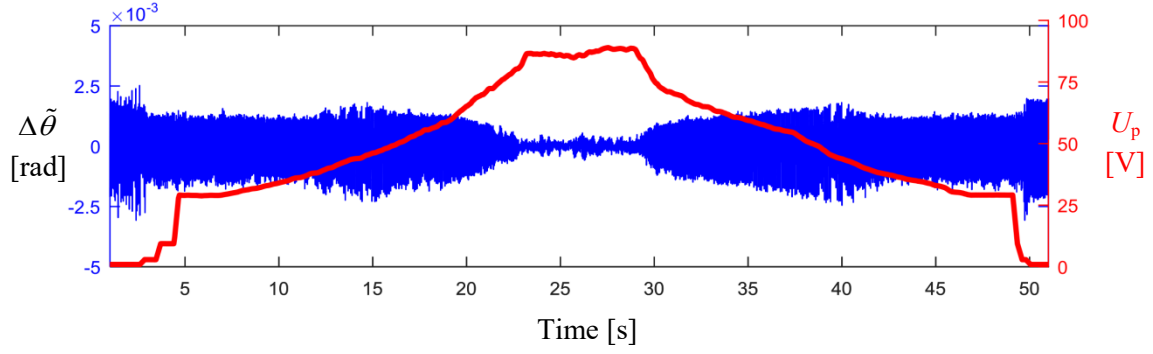
Fig. 6.8: Suppression of creep groan by an external excitation with varied voltage amplitude

6.2 Passive method against creep groan

Another feasible method against creep groan is to increase the damping of the shaft. Compared to the active method, the passive method doesn't require external actuators and sensors. When the damping of the drive shaft increases, energy dissipation in the slip region becomes so large, that the system may not return to the stick region. As a result, the stick-slip motion cannot repeat and creep groan cannot occur in the system. On the other hand, if damping of the carrier is increased, the vibration of the pad may be reduced, but the stick-slip motion on the disk-shaft sub-system is not influenced. The map of creep groan will not change. Therefore, only the countermeasure with increasing the damping of the shaft is discussed here.
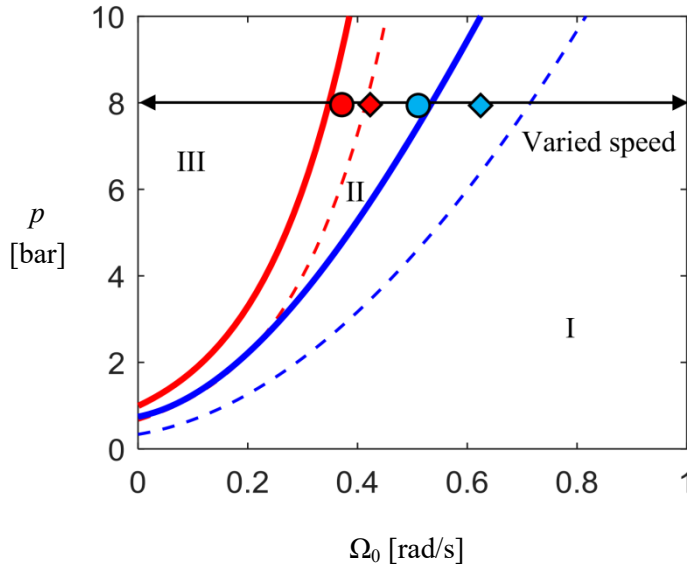
Fig. 6.9: Simulated map of creep groan of the system with (-) and without (- -) damping materials. The rhombus represent the measured critical points of the system without damping materials, the cycles represent the measured critical points of the system with damping materials

Theoretical analysis is by the model proposed in Eq. (3.42) with its parameters in Table 4.1 and Table 4.3. Fig. 6.9 shows the map of the parameter regions with and without damping materials, where the dotted line represents the region boundaries of the original system ($d_\theta = 2$ Nms), while the solid line denotes the region boundaries of the system with damping materials ($d_\theta = 2.5$ Nms). Compared to map of the original system, the area of regions II and III is decreased with the increase of damping of the drive shaft, i.e. damping materials reduce the risk of creep groan generation.
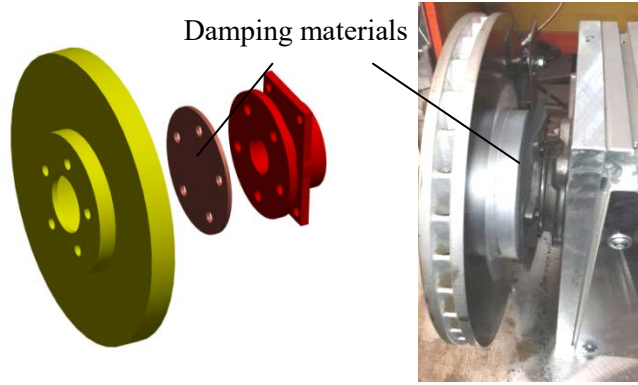
Fig. 6.10: Adding damping materials between the disk and the driven shaft

(a)

(b)
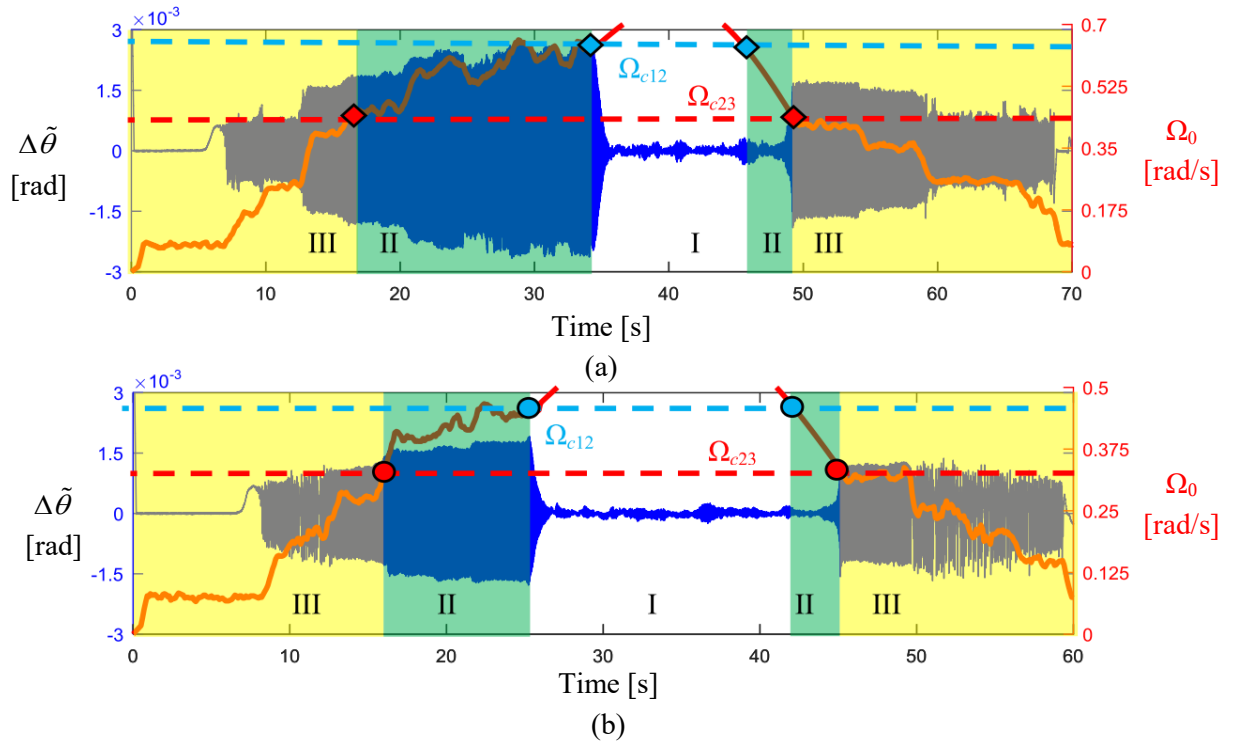
Fig. 6.11: The critical speed of original the system (a), and that of the system with damping materials (b), the rhombus represent the measured critical points of the system without damping materials, the cycles represent the measured critical points of the system with damping materials

In practice, damping materials are added between the shaft and brake disk as shown in Fig. 6.10, and experiments are carried out to testify the above theoretical analysis. The driving speed is varied under a constant brake pressure (8 bar). The measured results are shown in Fig. 6.11, where the blue line denotes the vibration of the shaft and the red line presents the motor speed. For the original brake system, the critical speed between regions I and II is 0.62 rad/s and the critical speed between regions II and III is 0.42 rad/s, which are marked in Fig. 6.9 with the rhombus. For the system with damping materials, both the critical speeds are decreased. The critical speed between region I and II becomes 0.48 rad/s and the critical speed between regions II and III is decreased to 0.35 rad/s, which are marked in Fig. 6.9 with circles. The experiments indicate that both critical speeds are decreased by

adding damping materials between the shaft and the disk. In practice, the shaft can be designed with a large damping coefficient. It is possible to increase the thickness of the shaft so that the damping of the shaft increases.

6.3 Suppression of creep groan through an optimal brake technique

In this section, the occurrence of creep groan in drive processes will be studied with the assistance of the map of creep groan. Instead of redesigning the components of a vehicle, another way to influence creep groan is to control the velocity of the wheel and brake pressure during drive processes. For the sake of simplification, a two wheel vehicle model is used for the simulation. The dynamics of a vehicle is given as

$$M\dot{\Omega}(t)r + F_r(\Omega(t)) = T_0 r - \sum_{i=1}^{2} A_p p_i(t)\mu\frac{R}{r}, \tag{6.14}$$

where M is the mass of the vehicle, r is the radius of the wheel, F_r is the resistance force such as wind force, T_0 is the drive moment provided by the motor, $p(t)$ is the brake pressure, A_p is the area of the pressure surface, μ is the friction coefficient, R is the radius of the friction contact to the center of the disk, $\Omega(t)$ is the angular speed of wheels, which is calculated as

$$\Omega(t) = \int_0^t \dot{\Omega}(\tau)d\tau + \Omega_0. \tag{6.15}$$

In the accelerating process, it is assumed that the driver releases the brake pedal slowly, while the drive moment and the resistance force keep constant. As a result, the brake pressure and the corresponding velocity is given as

$$p(t) = p_0 - a_0 t, \tag{6.16}$$

$$\Omega(t) = \frac{1}{Mr}\left(T_0 r - F_r - 2\frac{R}{r}p_0 A_p \mu\right)t + \frac{1}{Mr}\frac{R}{r}\mu A_p a_0 t^2 + \Omega_0,$$

where p_0 is the initial brake pressure, a_0 is the slop of the linear decreasing brake pressure.

If this process is plotted in the map of creep groan, the time of creep groan can be easily estimated with the assistance of the map. As shown in Fig. 6.12 (a), the system is at first in region III and creep groan occurs since the stick-slip limit cycle is the only stable solution of the system, where the red line denotes the system with creep groan. With increasing speed, creep groan disappears once the system enters region I, where the blue line denotes the system without creep groan. Fig. 6.12 (b) shows the brake pressure and the angular speed of the wheel. In the accelerating process, creep groan appears at the beginning and disappears at 4.7 seconds.

In the decelerating process, it is assumed that the driver presses the brake pedal slowly, and the brake pressure is increased with a slop a_0. Then, the brake pressure and the corresponding velocity of the vehicle is given as

$$p(t) = p_0 + a_0 t, \qquad (6.17)$$

$$\Omega(t) = \frac{1}{Mr}\left(T_0 r - F_r - 2\frac{R}{r}p_0 A_p \mu\right)t - \frac{1}{Mr}\frac{R}{r}\mu A_p a_0 t^2 + \Omega_0.$$

The decelerating process is plotted in the map of creep groan as shown in Fig. 6.13 (a). The system is at first in regions I and creep groan doesn't appear. Creep groan appears when the system reaches to region III since the equilibrium solution of the system becomes unstable. Fig. 6.13 (b) shows the brake pressure and the angular speed of the wheel. In the decelerating process, creep groan appears at 7 seconds and disappears at 9 seconds.

From the simulations, it is obvious that the time of creep groan in the accelerating process is longer than the time of the decelerating process. In the decelerating process, the initial condition is near the equilibrium solution, and creep groan happens when the equilibrium solution is unstable. In the accelerating process, the initial condition is near the stick-slip limit cycle, and creep groan disappears when the stick-slip limit cycle doesn't exist. This can explain why creep groan is more serious in the accelerating process than in the decelerating process, which agrees with driving experience. In practice, creep groan normally happens in the accelerating process.

In order to reduce the time of creep groan, an optimal accelerating process is proposed. Instead of linear decreasing the brake pressure, the cadence braking technique is introduced to prevent creep groan. Cadence braking means that the driver releases the brakes for a short time and brakes again. When the driver releases the brakes at low speed, the system leaves regions III and II rapidly. After that, even the brake pressure increases again and enters region II, creep groan doesn't appear since its initial condition is near its equilibrium solution. Simulation results are shown in Fig. 6.14. In this optimal accelerating process, creep groan appears at the beginning and disappears at 0.8 seconds, which is much shorter than the time of creep groan under the linear accelerating process described in Eq. (6.16) (with 4.7 seconds).
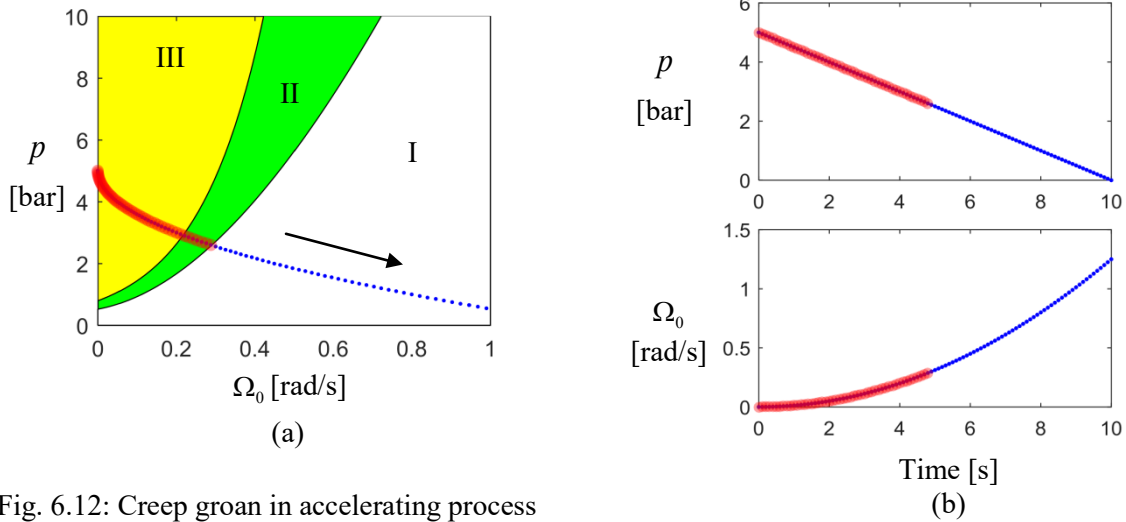
Fig. 6.12: Creep groan in accelerating process
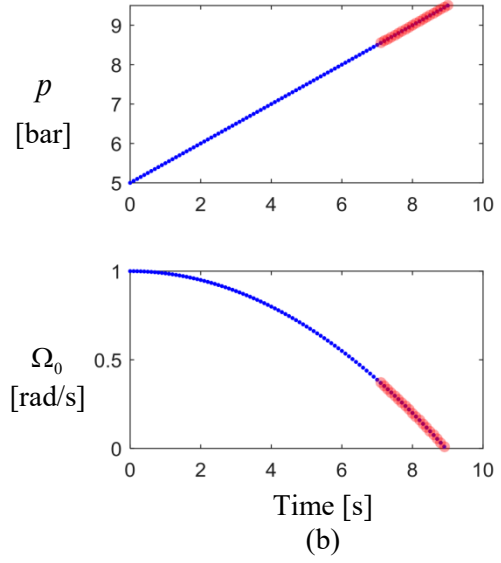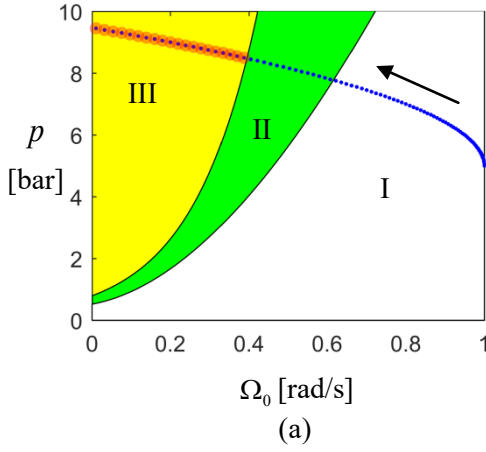
Fig. 6.13: Creep groan in decelerating process
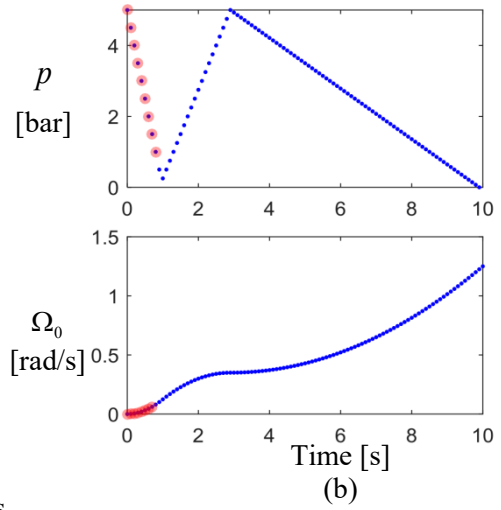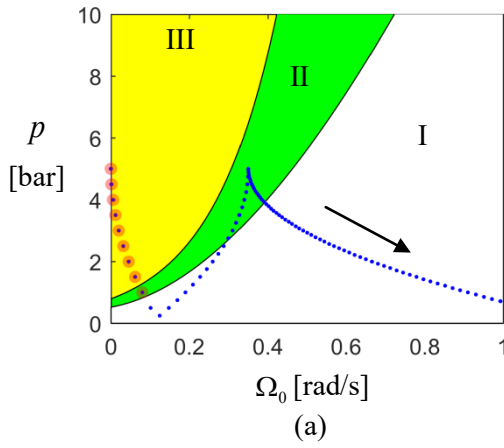
Fig. 6.14: Creep groan in optimal accelerating process

An anti-lock braking system (ABS) is an automobile safety system that allows the wheels on a vehicle to keep traction contact preventing the wheels from locking up. It can imitate the cadence braking that was practiced by skillful drivers [114]. An ABS can apply cadence braking 15 times per second, while human can do just 1 or 2 times per second. Because of this, the wheels of cars equipped with the ABS work much better than the human. Typically, an ABS includes a central electronic control unit (ECU), wheel speed sensors, and hydraulic valves within the brake hydraulics. The speed sensors determine the acceleration or deceleration of each wheel; the ECU constantly monitors the rotational speed of each wheel and controls the valves to avoid wheel lock. If a wheel rotates significantly slower than the others, the ECU can judge the impending wheel lock and actuate the valve to reduce hydraulic pressure of the brake at the affected wheel. As a result, the braking pressure on that wheel is reduced and the wheel then turns faster. Conversely, if the ECU detects a wheel turning significantly faster than the others, the brake pressure to the wheel is increased so the braking pressure is reapplied, slowing down the wheel. This process is repeated continuously to prevent the wheel block.

In the following parts, simulation analysis will be proposed to confirm that an ABS can be delivered to prevent creep groan of a vehicle, if cadence braking is applied by the ABS during the occurrence of creep groan.

At first, a creep groan detection technique is required to distinguish the creep groan case from the non-creep groan case. When creep groan occurs in a wheel, the brake disk will be alternating adhesion and sliding on the pad. As a result, a transient block of disk can be observed. The experimental result shows that the block time is about 0.01 second. This time is too short to be detected by the speed sensor of the vehicle. Therefore, a high revolution speed sensor is required for the creep groan detection, such as turning angle transmitters. Creep groan can be detected if the speed of one disk approaches to 0 but other disks not. The structure of the ABS for the suppression of creep groan exhibits in Fig. 6.15, including a central electronic control unit (ECU), high revolution wheel speed sensors, hydraulic valves within the brake hydraulics.

Once creep groan occurs in the system, the ABS can control the hydraulic valve to reduce the brake pressure. The dynamic equation of a vehicle with the ABS is given as

$$Mr\dot{\Omega} = T_0 r - \sum_{i=1}^{2} \frac{R}{r} p_{ABS,i} A_p \mu - F_r(\Omega),$$

(6.18)

where p_{ABS} is the controlled brake pressure by the ABS. Its dynamics is given as

$$\begin{cases} \dot{p}_{ABS,i} = -b_{de} p_{ABS,i} & \text{,with creep groan} \\ \dot{p}_{ABS,i} = -b_{in} p_{ABS,i} + p_d & \text{,without creep groan and } p_{ABS} < p_d \\ \dot{p}_{ABS,i} = 0 & \text{,otherwise} \end{cases}$$

(6.19)

where b_{de} and b_{in} are constant determining the decreasing and increasing rate of the brake pressure, p_d is the designed brake pressure, which is determined by the position of brake pedal. The parameters of the simulation are taken from the Table 4.1 and Table 4.3. Simulation results illustrate that creep groan can be eliminated by the ABS. In the simulation, the designed brake pressure given by the driver is assumed at 5 bar. Since the drive moment of motor is larger than the brake pressure, the vehicle accelerates slowly. The accelerating process without the ABS is expressed in the map of creep groan as shown in Fig. 6.16 (a). The angular velocity of disk is shown in Fig. 6.16 (b), where the stick region is marked with red color. Creep groan appears at the beginning and disappears at 6.3 seconds when the system enters into region I. Fig. 6.16 (c) exhibits the acceleration of the pad, large impulses are observed during creep groan. This vibration will be felt/ heard by the driver and affect driver experience.
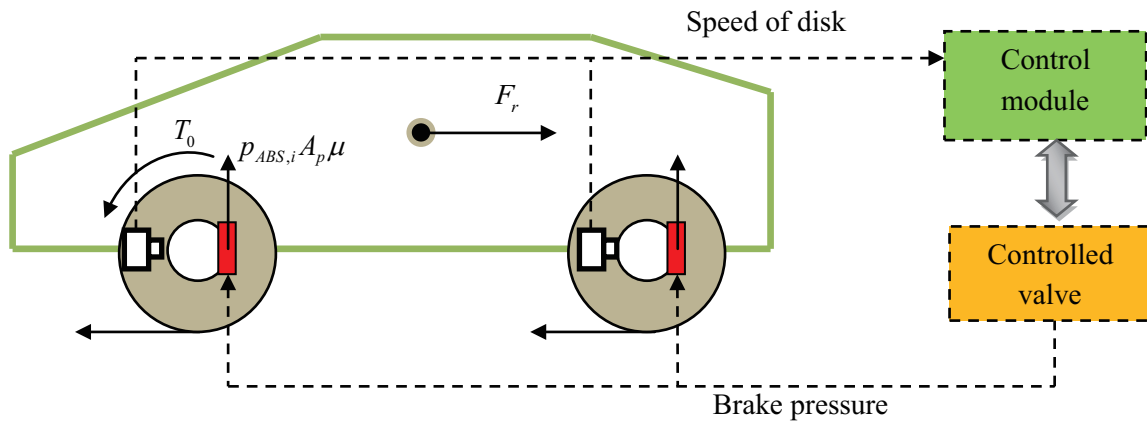
Fig. 6.15: Anti-lock braking system according to [114]

If an ABS is used in the brake system, the brake pressure can be controlled to prevent the vehicle from creep groan. The accelerating process with the assistance of the ABS is plotted in the map of creep groan as shown in the Fig. 6.17 (a). This process can be described as that the brake pressure is decreased once the stick-slip motion occurs, while the brake pressure returns to the designed pressure when the stick-slip motion disappears. As a result, the speed and the pressure of the vehicle will follow the boundary between regions II and III. The angular velocity of disk is shown in Fig. 6.17 (b), where the stick region is marked with red color. Fig. 6.17 (c) exhibits the acceleration of the pad. Compared to the simulation results without ABS, creep groan of the brake system with the ABS occurs only in short time intervals, i.e., creep groan can be successfully eliminated through the ABS.
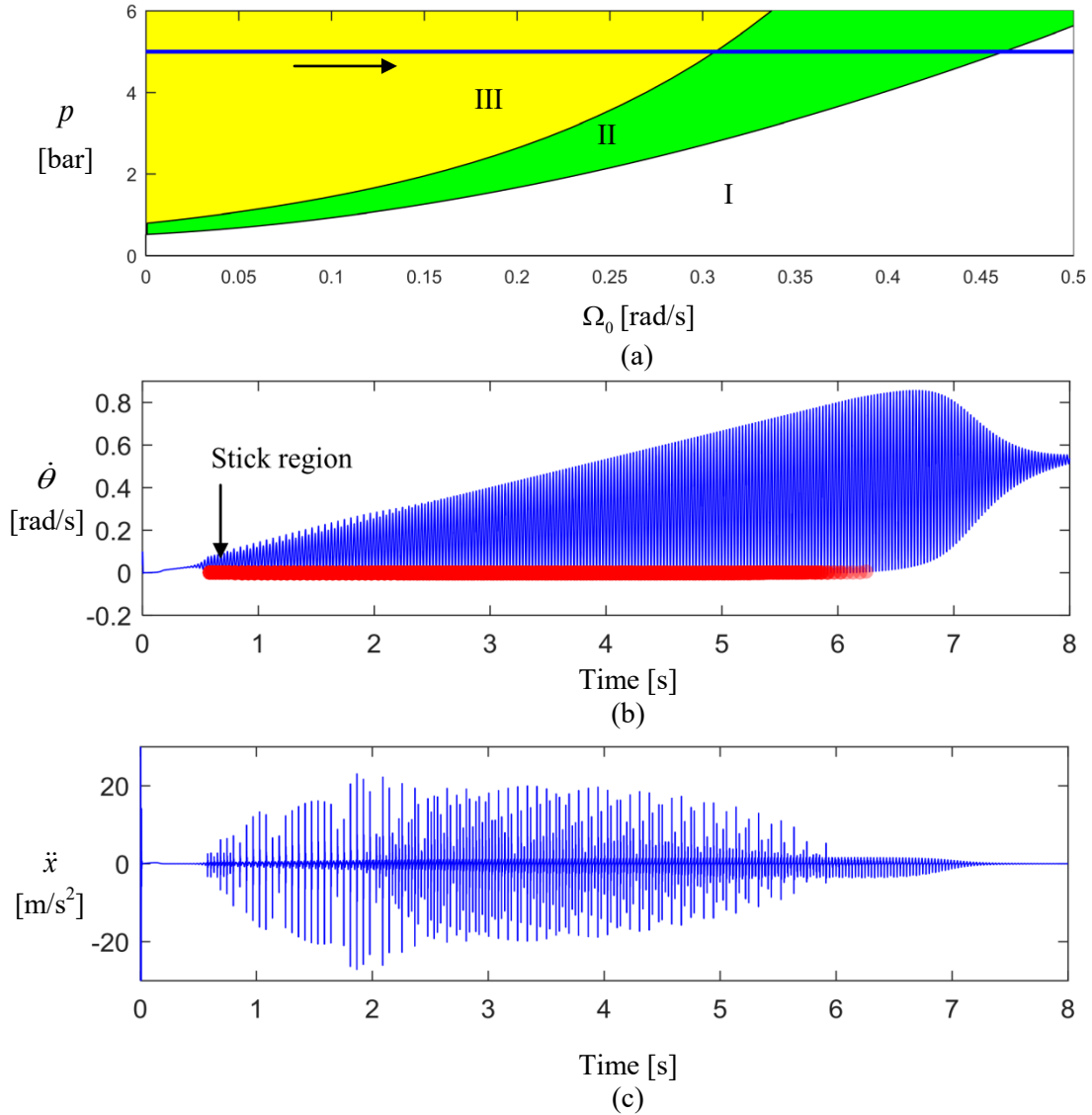
Fig. 6.16: Accelerating process without the assistance of an ABS, (a) accelerating process plotted in the map of creep groan, (b) angular velocity of disk, (c) acceleration of the pad
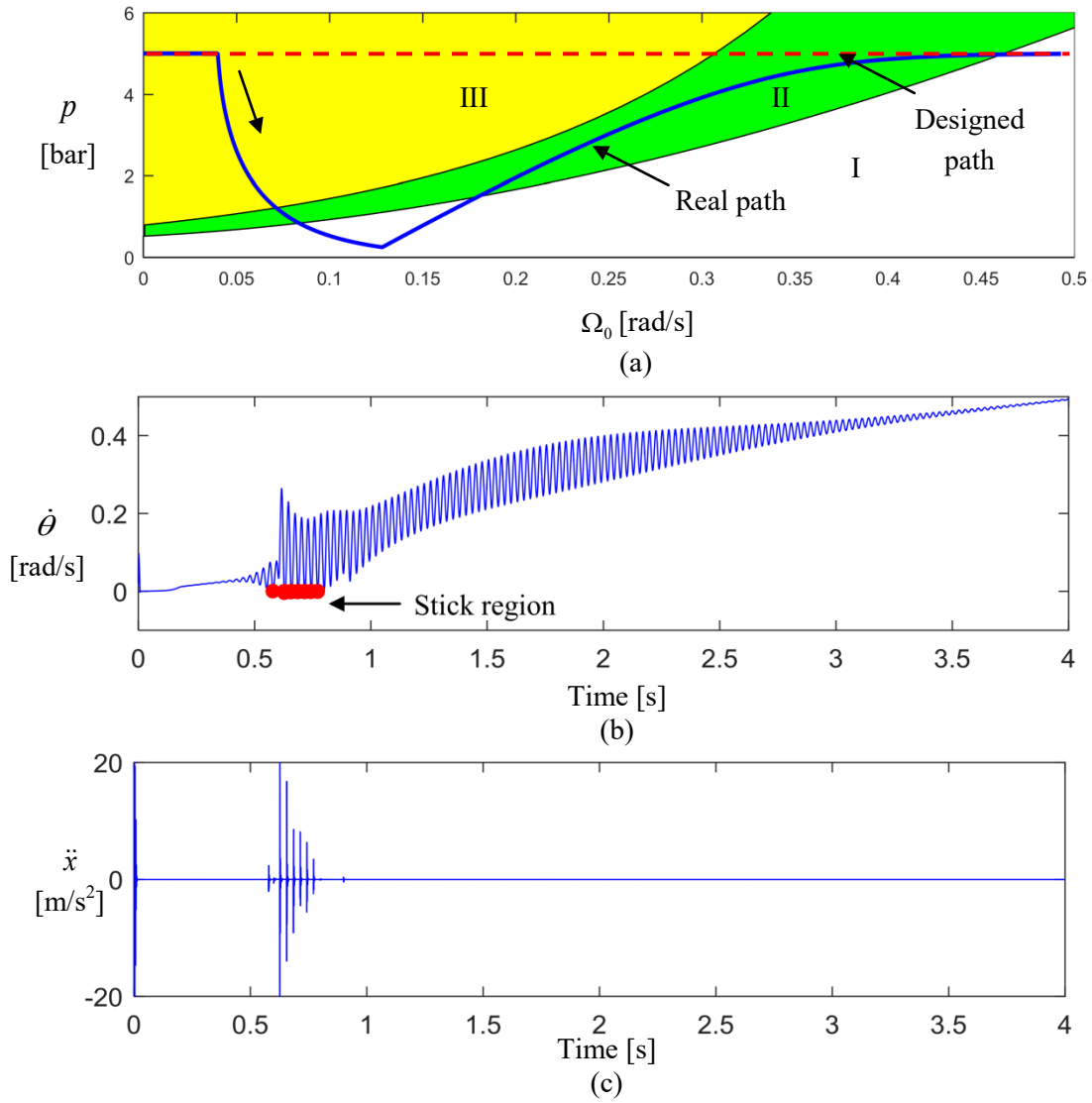
Fig. 6.17: Accelerating process with the assistance of an ABS, (a) accelerating process plotted in the map of creep groan, (b) angular velocity of disk, (c) acceleration of the pad

6.4 Summary

In this chapter, different methods are proposed to suppress creep groan, in terms of adding piezoceramics actuator, increasing the damping of the drive shaft, and by an optimal braking technique.

At first, theoretical and experimental investigations are carried out to confirm that creep groan can be eliminated by giving a high frequency mechanical vibration in the out-of-plane direction of the disk. The high frequency vibration is provided by an active pad, which contains two piezoelectric layers with an electrode layer between them. The static friction coefficient is decreased by giving a high frequency vibration, and creep groan can be eliminated when the static friction coefficient is less than a critical value. If a piezoceramic actuator is assembled between the short edges of the L-shaped steel plates and the frame, a high frequency mechanical vibration can be provided in the in-plane direction of the disk, and Creep groan can also be eliminated. Furthermore, the active pad is assembled in the test rig with a real brake, and creep groan of the real brake is suppressed by the active pad successfully.

Another feasible method against creep groan is to increase the damping of the shaft. By adding damping materials between the drive shaft and disk, energy dissipation during the slip region becomes large. As a result, the system cannot return to the stick region again so that creep groan is suppressed. Experimental and simulation results indicate that the area of regions II and III decreases with the increase of the damping of the shaft, i.e. there is less the risk of creep groan generation.

With the assistance of the map of creep groan, creep groan in accelerating and decelerating processes is studied. It is found out that creep groan is more serious in the accelerating process than in the decelerating process, which agrees with driving experience. After that, an optimal brake technique (cadence braking) is proposed to minimize the time of creep groan. Furthermore, an ABS can perform the cadence braking through a simple control loop to avoid creep groan just like a skillful driver. Simulation results indicate that creep groan can be eliminated with the assistance of the ABS.

7 Conclusions and Future Work

The main objective of this thesis is to study the fundamental mechanism of creep groan theoretically and experimentally. In Chapter 1, brief introductions on major development of brake noise, vibration and harshness, stick-slip motion and creep groan are presented. Due to the increasing comfort claims of customers, the study on low frequency creep groan has been receiving increasing attention currently.

In order to understand creep groan step by step, test rigs concentrating on creep groan are presented in Chapter 2. At first, a test rig with an idealized brake is built to study creep groan concentrated on friction contact. Subsequently, a test rig with a real brake, which is more similar to a real vehicle, is set up to study creep groan. Experimental results from both test rigs are presented and compared with each other.

In Chapter 3, different friction laws i.e. Coulomb's friction law and the bristle friction law are used to describe creep groan of the test rig with an idealized brake. The stick-slip limit cycle is firstly obtained by coupling the system model with Coulomb's friction law, in which the static friction coefficient is larger than the dynamic friction coefficient. However, the non-smooth characteristic appears between the stick and slip regions due to the switch function in Coulomb's friction law. In contrast, the bristle friction law, containing the Stribeck effect, pre-sliding effect and hysteresis, can overcome this issue. According to the stability of the equilibrium solution and the stick-slip limit cycle, the system with Coulomb's friction law has two parameters regions, i.e. a region with a stable equilibrium solution but no stick-slip limit cycle named as region I; and a region with both stable equilibrium solution and stick-slip limit cycle named as region II. In contrast, the model with the bristle friction law has three parameter regions. Besides regions I and II, there is an additional region with an unstable equilibrium solution and a stable stick-slip limit cycle, named as region III. Since different friction laws lead to different dynamic characteristics, one should choose the suitable friction law carefully to describe creep groan of brake systems.

Chapter 4 focuses on the study on the parameter identification of the friction law. If Coulomb's friction law is employed, the unknown parameters related to the contact surfaces are static and dynamic friction coefficients. They can be identified by analyzing the geometric shape of the stick-slip limit cycle. If the bristle friction law is employed, the unknown parameters related to the contact surfaces contain the static friction coefficient, the dynamic friction coefficient, the Stribeck velocity, the contact stiffness and the contact damping. As a result, a genetic algorithm is used to estimate those parameters by comparing the simulation results with the experimental results. Compared to the model with Coulomb's friction law, the model with the bristle friction law can describe the pre-sliding effect between the stick and slip regions. Besides, by changing the speed of the motor under constant brake pressure, three parameter regions namely regions I, II and III can be detected experimentally. This demonstrates that the model with bristle friction law is more reasonable to describe creep groan. At the end of Chapter 4, a Proportional-Integral observer is designed to observe the friction force from the measured $\Delta\theta$ and $\Delta\dot{\theta}$. Compared to the modeling method, the friction observer requires only a linear disk-shaft model. However, it has a disadvantage that the measurement noise will strongly influence the accuracy of the observed force. The observed friction is similar to the calculated friction by the model with the bristle friction law.

The theoretical and experimental studies of creep groan on the test rig with a real brake are presented in Chapter 5. Compared to the idealized brake, the test rig with a real brake contains a real brake carrier and an additional suspension system. A model with large number of degrees of freedom is firstly set up to describe the brake system. By analyzing the dynamic model, it is possible to isolate the brake suspension system from the frame, the axle and the chassis for the study of the stick-slip motion. Therefore, complex components such as the chassis can be at first ignored for the friction force calculation. Subsequently, a reduced-order model is proposed to improve the calculation efficiency. The advantages of the reduce-order model are that it requires only system parameters instead of the physical parameters and it has high computational efficiency. With the identified parameters to hand, the simulated stick-slip limit cycle is compared to the experimental one. Both results have good agreement with each other, which confirms that the reduced-order model is of efficiency to describe creep groan of the brake system. Furthermore, a map of creep groan is obtained by stability analysis of the equilibrium solution and stick-slip limit cycle. This map is compared with the map measured through experiments. The measured and calculated maps show the similar behavior.

In Chapter 6, some suppression methods of creep groan are finally implemented on the theoretical model as well as on the test rigs. At first, an active pad, containing two piezoelectric layers with an electrode layer between them, successfully eliminates creep groan by providing a high frequency mechanical vibration in the out-of-plane direction of the disk. The high frequency vibration decreases the static friction coefficient, and thus eliminates creep groan. Later, by adding a high frequency vibration in the in-plane direction, creep groan is also eliminated. Another feasible method against creep groan is to increase the damping of the shaft. It is confirmed that by increasing the damping of the shaft, the area of the regions II and III decreases, i.e. there is less risk to generate creep groan. At last, a method to shorten the time of creep groan by using an optimal brake technique is presented. The system can leave the regions III and II rapidly by preceding the optimal brake technique. If this optimal brake technique is integrated in an ABS, the ABS can perform the optimal braking process through a simple control loop to avoid creep groan just like a skillful driver. Simulation results indicate that creep groan can be eliminated with the assistance of the ABS.

In general, this thesis attempts to build a detail model to describe creep groan on the brake system. Methods for suppression of creep groan are suggested based on the model. Some future work is outlined as follows.

- Theoretical and experimental investigations of creep groan on a real vehicle can be studied and compared with the results from the test rigs.

- The efficiency of the active pad needs to be tested under real drive conditions. It is important to know the influence of the external high frequency excitation on a real vehicle.

- Experimental investigations on the suppression of creep groan by an anti-lock braking system can be further studied. Since an ABS is a safety relevant system, is it sensible to use it to solve the comfort problem? This question should be further discussed.

Bibliography

[1]   Kinkaid, N. M.; O'Reilly, O. M. and Papadopoulos P.: Automotive disk brake squeal. *Journal of Sound and Vibration*, 267(1), 105-166, 2003.

[2]   AbuBakar, A. R. and Ouyang, H.: Complex eigenvalue analysis and dynamic transient analysis in predicting disk brake squeal. *International Journal of Vehicle Noise and Vibration*, 2(2), 143-155, 2006.

[3]   Abendroth, H. and Wernitz, B.: The integrated test concept: Dyno-vehicle, performance-noise. *SAE Technical Paper*, No. 2000-01-2774, 2000.

[4]   Ouyang, H.; Nack, W.; Yuan, Y. and Chen, F.: Numerical analysis of automotive disk brake squeal: a review. *International Journal of Vehicle Noise and Vibration*, 1(3-4), 07-231, 2005.

[5]   Breuer, B. and Bill, K. H.: *Brake technology handbook*. SAE International, 2008.

[6]   Cantoni, C.; Cesarini, R.; Mastinu, G.; Rocca, G. and Sicigliano, R.: Brake comfort - a review. *Vehicle System Dynamics*, 47(8), 901-947, 2009.

[7]   von Wagner, U.; Hochlenert, D. and Hagedorn, P.: Minimal models for disk brake squeal. *Journal of Sound and Vibration*, 302(3), 527-539, 2007.

[8]   von Wagner, U. and Schlagner, S.: On the origin of disk brake squeal. *International Journal of Vehicle Design*, 51(1-2), 223-237, 2009.

[9]   Gräbner, N.: *Analyse und Verbesserung der Simulationsmethode des Bremsenquietschens*. Ph. D. thesis, Technische Universität Berlin, 2016.

[10]   Papinniemi, A.; Lai, J. C.; Zhao, J. and Loader, L.: Brake squeal: a literature review. *Applied Acoustics*, 63(4), 391-400, 2002.

[11]   Hetzler H. and Willner K.: On the influence of contact tribology on brake squeal. *Tribology International*, 46(1), 237–246, 2012.

[12]   Spelsberg-Korspeter G.: Eigenvalue optimization against brake squeal: symmetry, mathematical background and experiments. *Journal of Sound and Vibration*, 331(19), 4259–4268, 2012.

[13]   Gödecker, H.: *Ein Verfahren zur schnellen experimentellen Charakterisierung der Quietschneigung von Kfz-Scheibenbremsen*. Ph. D. thesis, Technische Universität Berlin, 2015.

[14]   Hornig, S. A.; Hochlenert, D.; Gödecker, H.; Gräbner, N. and von Wagner, U.: Steps towards predictive simulation and faster experimental investigation of automotive brake systems with respect to squeal. *SAE Technical Paper*, No. 2013-01-1908, 2013.

[15]   von Wagner, U.; Hornig, S.; Gräbner, N. and Gödecker H.: Schnelle Wege zur Entwicklung leiser Bremsen – aktuelle Forschung und Perspektiven. *Fortschritt-Berichte VDI*, *Reihe 12: Verkehrstechnik/Fahrzeugtechnik*, 115-147, 2013.

[16]   Tiedemann, M.; Stender, M. and Hoffmann N.: Impact of joints on dynamic behaviour of brake systems. *Proceedings of Eurobrake Conference*, Lille, 2014.

[17]   Gräbner, N.; Mehrmann, V.; Quraishi, S.; Schröder C. and von Wagner, U.: Numerical methods for parametric model reduction in the simulation of disk brake squeal. *ZAMM - Journal*

of Applied Mathematics and Mechanics, 96(12), 1388-1405, 2016.

[18] Nack, W. V. and Arun M. J.: Friction induced vibration: brake moan. *SAE Technical Paper*, No. 951095, 1995.

[19] Bauer, J.; Körner, M. and Pfaff, A.: Moan noise - the phenomenon and solution approaches. *Eurobrake*, Dresden, EB2017-VDT-002, 2017.

[20] Jacobsson, H.: Disk brake judder considering instantaneous disk thickness and spatial friction variation. *Proceedings of the Institution of Mechanical Engineers, Part D: Journal of Automobile Engineering*, 217, 325–341, 2003.

[21] Jacobsson H.: Wheel suspension related disk brake judder. *ASME, in: Proceedings of the Design Engineering Technical Conferences*, Sacramento, USA, 1997.

[22] Abdelhamid, M. K.: Brake judder analysis using transfer functions. *SAE Technical Paper*, No. 973018, 1997.

[23] Kubota, M. and Suenaga, T.: A study of the mechanism causing high-speed brake judder. *SAE Technical Paper*, No. 980594, 1998.

[24] Sen, O. T.; Dreyer, J. T. and Singh, R.: Order domain analysis of speed-dependent friction-induced torque in a brake experiment. *Journal of Sound and Vibration*, 331, 5040–5053, 2012.

[25] Duan, C. and Singh, R.: Analysis of the vehicle brake judder problem by employing a simplified source-path-receiver model. *Proceedings of the Institution of Mechanical Engineers, Part D: Journal of Automobile Engineering*, 225, 141–149, 2010.

[26] Sen, O. T.; Dreyer, J. T. and Singh, R.: Envelope and order domain analyses of a nonlinear torsional system decelerating under multiple order frictional torque. *Mechanical Systems and Signal Processing*, 35(1): 324-344, 2013.

[27] Abdelhamid, M. K.: Creep groan of disk brakes. *SAE Technical Paper*, 951282, 2-24, 1995.

[28] Abdelhamid, M. K. and Bray, W.: Braking systems creep groan noise: detection and evaluation. *SAE Technical Paper*, No. 2009-01-2103, 10-11, 2009.

[29] Brecht, J.; Hoffrichter, W. and Dohle, A.: Mechanisms of brake creep groan. *SAE Technical Paper*, No. 973026, 1997.

[30] Brecht, J.: *Untersuchungen zum Bremsenknarzen-ein Beitrag zur Beschreibung von Schwingungen in Bremssystemen*. Ph.D. Thesis, Thesis University Siegen, 2000.

[31] Zhao, X.; Gräbner, N. and von Wagner, U.: Experimental and theoretical investigation of creep groan of brakes through minimal models. *PAMM*, 16(1), 295-296, 2016.

[32] Zhao, X.; Gräbner, N. and von Wagner, U.: Creep groan: fundamental experimental and theoretical investigations. *Eurobrake*, Dresden, EB2017-FBR-002, 2017.

[33] Zhao, X.; Gräbner, N. and von Wagner, U.: Theoretical and experimental investigations of the bifurcation behavior of creep groan of automotive disk brakes. *Submitted to Journal of Theoretical and Applied Mechanics*, 2017.

[34] Urbakh, M.; Klafter, J.; Gourdon, D. and Israelachvili, J.: The nonlinear nature of friction. *Nature*, 430(6999), 525-528, 2004.

[35] Israelachvili, J.: *Intermolecular and Surface Forces*. New York: Academic, 1995.

[36] Dowson, D.: *History of Tribology*. Langman, London, 1979.

[37] Byerlee, J. D.: Frictional characteristics of granite under high confining pressure. *Journal of Geophysical Research*, 72(14), 3639-3648, 1967.

[38] Dieterich, J. H.: Time-dependent friction in rocks. *Journal of Geophysical Research*, 77, 3690–3697, 1972.

[39] Stribeck, R.: Die wesentlichen Eigenschaften der Gleit- und Rollenlager - The key qualities of sliding and roller bearings. *Zeitschrift des Vereins Deutscher Ingenieure*, 46(38-39), 1342-1348, 1902.

[40] Leine, R. I.; Van Campen, D. H.; De Kraker, A. and Van Den Steen, L.: Stick-slip vibrations induced by alternate friction models. *Nonlinear Dynamics*, 16(1), 41-54, 1998.

[41] Popp, K.; Hinrichs, N. and Oestreich, M.: Dynamical behaviour of a friction oscillator with simultaneous self and external excitation. *Sadhana: Academy Proceedings in Engineering Sciences*, 20(2-4), 627–654, 1995.

[42] Den Hartog, J. P.: Forced vibrations with combined Coulomb and viscous friction. *Transaction ASME Paper APM*, 53(15), 107-115, 1931.

[43] Bowden, F. P. and Tabor, D.: *Friction - an Introduction to Tribology*. New York: Anchor Press/Doubleday, 1973.

[44] Magnus, K.: *Schwingungen*. Teubner, Stuttgart, 1961.

[45] Marui, E. and Kato, S.: Forced vibration of a base-exited single-degree-of-freedom system with Coulomb friction. *Transaction ASME, Journal of Dynamical Systems, Measurement and Control*, 106, 280-285, 1984.

[46] Miyamoto, M.: Effect of dry friction in link suspension on forced vibration of two-axle car. *Quarterly Reports*, 14, 99-103, 1973.

[47] Popp, K.; Hinrichs, N. and Oestreich, M.: Dynamical behaviour of a friction oscillator with simultaneous self and external excitation. *Sadhana: Academy Proceedings in Engineering Sciences,* 20(2-4), 627–654, 1995.

[48] Van de Vrande, B. L.; Van Campen, D. H. and De Kraker, A.: Some aspects of the analysis of stick-slip vibrations with an application to drill strings. *in Proceedings of ASME Design Engineering Technical Conference*, 14–17, Sacramento, 1997.

[49] Pfeiffer, F.: Dynamical systems with time-varying or unsteady structure. *Zeitschrift für Angewandte Mathematik und Mechanik*, 71(4), 6–22, 1991.

[50] Bernardo, M.; Budd, C.; Champneys, A. R. and Kowalczyk, P.: *Piecewise-smooth Dynamical Systems: Theory and Applications*. Springer Science and Business Media, 2008.

[51] Leine, R. I. and Nijmeijer, H.: *Dynamics and Bifurcations of Non-smooth Mechanical Systems*. Springer Science and Business Media, 2013.

[52] Luo, A. and Thapa, S.: On nonlinear dynamics of simplified brake dynamical systems. *In ASME 2007 International Mechanical Engineering Congress and Exposition, American Society of Mechanical Engineers*, 1849-1859, Seattle, 2007.

[53] Luo, A.: A theory for non-smooth dynamic systems on the connectable domains. *Communications in Nonlinear Science and Numerical Simulation*, 10(1), 1-55, 2005.

[54] Ibrahim, R A.: Friction-induced vibration, chatter, squeal, and chaos, Part I: mechanics of contact and friction, *Applied Mechanics Reviews*, 47, 209–226, 1994.

[55] Ibrahim, R A.: Friction-induced vibration, chatter, squeal, and chaos. Part II: dynamics and modeling. *Applied Mechanics Reviews*, 47, 227–253, 1994.

[56] Galvanetto, U. and Knudsen, C.: Events Maps in a Stick-Slip System. *Nonlinear Dynamics*, 13(2): 99-115, 1997.

[57] Storck, H.; Littmann, W.; Wallaschek, J. and Mracek, M.: The effect of friction reduction in presence of ultrasonic vibrations and its relevance to travelling wave ultrasonic motors. *Ultrasonics*, 40(1), 379-383, 2002.

[58] Popov, V.: Kontaktmechanik und Reibung: von der Nanotribologie bis zur Erdbebendynamik. *Springer-Verlag*, 2016.

[59] Popov, V.; Starcevic, J. and Filippov, A. E.: Influence of ultrasonic in-plane oscillations on static and sliding friction and intrinsic length scale of dry friction processes. *Tribology letters*, 39(1), 25-30, 2010.

[60] Thomsen, J. J.: Using fast vibrations to quench friction-induced oscillations. *Journal of Sound and Vibration*, 228(5), 1079-1102, 1999.

[61] Godfrey, D.: Vibration reduces metal to metal contact and causes an apparent reduction in friction. *ASLE Transactions*, 10(2), 183-192, 1967.

[62] Armstrong-Hélouvry, B.: *Control of Machines with Friction*. Springer Science and Business Media, 1991.

[63] Al-Bender, F; Lampaert, V. and Swevers, J.: The generalized Maxwell-slip model: a novel model for friction simulation and compensation. *IEEE Transactions on Automatic Control*, 50(11), 1883-1887, 2005.

[64] Dupont, P.; Hayward, V.; Armstrong, B. and Altpeter, F.: Single state elasto-plastic friction models. *IEEE Transactions on Automatic Control*, 47(5), 787–792, 2002.

[65] Dahl, P.: A solid friction model. *Aerospace Corp El Segundo Ca*, TOR-0158(3107–18)-1, 1968.

[66] Dahl, P.: Solid friction damping of mechanical vibrations. *AIAA journal*, 14, 1675–1682, 1976.

[67] Canudas de Wit, C.; Olsson, H.; Astrom, K. J. and Lischinsky, P.: Dynamic friction models and control design. *In American Control Conference*, 1920-1926, San Francisco, 1993.

[68] Canudas de Wit, C.; Olsson, H.; Astrom, K. J. and Lischinsky, P.: A new model for control of systems with friction. *IEEE Transactions on Automatic Control*, 40(3), 419-425, 1995.

[69] Canudas de Wit, C. and Lischinsky, P.: Adaptive friction compensation with partially known dynamic friction model. *International Journal of Adaptive Control and Signal Processing*, 11(1), 65-80, 1997.

[70] Olsson, H.; Aström, K. J.; Canudas de Wit, C.; Gäfvert, M. and Lischinsky, P.: Friction models and friction compensation. *European Journal of Control*, 4(3), 176-195, 1998.

[71] Johanastrom, K. and Canudas de Wit, C.: Revisiting the LuGre friction model. *IEEE Control Systems*, 28(6), 101-114, 2008.

[72] Li, Y. and Feng, Z. C.: Bifurcation and chaos in friction-induced vibration. *Communications in Nonlinear Science and Numerical Simulation*, 9(6), 633-647, 2004.

[73] Krim, J.: Friction at the atomic scale. *Scientific Amer.*, 275(4), 74–80, 1996.

[74] Mate, C. M.; McClelland, G. M.; Erlandsson, R. and Chiang, S.: Atomic-scale friction of a tungsten tip on a graphite surface. *In Scanning Tunneling Microscopy*, 59(17), 226-229, 1987.

[75] Mate, M.: *Tribology on the Small Scale*. New York: Oxford Univ. Press, 2008.

[76] Tomanek, D.; Zhong, W. and Thomas, H.: Calculation of an atomically modulated friction force in atomic-force microscopy. *Europhysics Letters*, 15(8), 887-892, 1991.

[77] Fujisawa, S.; Kishi, E.; Sugawara, Y. and Morita, S.: Atomic-scale friction observed with a two-dimensional frictional-force microscope. *Physical Review B*, 51(12), 7849-7859, 1995.

[78] Tomlinson, G. A.: A molecular theory of friction. *The London, Edinburgh, and Dublin Philosophical Magazine and Journal of Science*, 7(46), 905-939, 1929.

[79] Gnecco, E.; Bennewitz, R.; Gyalog, T.; Loppacher, C.; Bammerlin, M.; Meyer, E. and Güntherodt, H. J.: Velocity dependence of atomic friction. *Physical Review Letters*, 84(6), 1172, 2000.

[80] Socoliuc A., Bennewitz R., Gnecco E. and Meyer E.: Transition from stick-slip to continuous sliding in atomic friction: entering a new regime of ultralow friction. *Physical Review Letters*, 92(13), 134301, 2004.

[81] Socoliuc, A.; Gnecco, E.; Maier, S.; Pfeiffer, O.; Baratoff, A.; Bennewitz R. and Meyer E.: Atomic-scale control of friction by actuation of nanometer-sized contacts. *Science*, 313(5784), 207-210, 2006.

[82] Jang, H.; Lee, J. S. and Fash, J. W.: Compositional effects of the brake friction material on creep groan phenomena. *Wear*, 251(1), 1477-1483, 2001.

[83] Fuadi, Z.; Maegawa, S.; Nakano, K. and Adachi, K.: Map of low-frequency stick–slip of a creep groan. *Proceedings of the Institution of Mechanical Engineers, Part J: Journal of Engineering Tribology*, 224(12): 1235-1246, 2010.

[84] Fuadi, Z.; Adachi, K.; Ikeda, H.; Naito, H. and Kato, K.: Effect of contact stiffness on creep-groan occurrence on a simple caliper-slider experimental model. *Tribology Letters*, 33(3), 169-178, 2009.

[85] Jung, T. and Seung, C.: Research for brake creep groan noise with dynamometer. *SAE International Journal of Passenger Cars-Mechanical Systems*, No. 2012-01-1824, 1224-1229, 2012.

[86] Vadari, V. and Jackson, M.: An experimental investigation of disk brake creep-groan in vehicles and brake dynamometer correlation. *SAE Technical Paper*, No. 1999-01-3408, 1999.

[87] Donley, M. and Riesland, D.: Brake groan simulation for a McPherson strut type suspension. *SAE Technical Paper*, No. 2003-01-1627, 2003.

[88] Zhang, P.; Zhang, L. and Meng, D.: Experimental and theoretical analysis of creep groan of disk brake. *Eurobrake*, Dresden, EB2015-NVH-008, 2015.

[89] Neis, P. D.; Ferreira, N. F.; Poletto, J. C.; Matozo, L. T. and Masotti, D.: Quantification of brake creep groan in vehicle tests and its relation with stick–slip obtained in laboratory

tests. *Journal of Sound and Vibration*, 369, 63-76, 2016.

[90]   Bettella, M.; Harrison M. F. and Sharp R. S.: Investigation of automotive creep groan noise with a distributed-source excitation technique. *Journal of Sound and Vibration*, 255(3), 531-547, 2002.

[91]   Gauterin, F.; Grochowicz, J.; Haverkamp, M.; Marschner, H.; Pankau, J. and Rostek, M.: Creep groan—phenomenology and remedy. *ATZ worldwide*, 106(7-8), 15-18, 2004.

[92]   Crowther, A. R. and Singh, R.: Analytical investigation of stick-slip motions in coupled brake-driveline systems. *Nonlinear Dynamics*, 50(3), 463-481, 2007.

[93]   Crowther, A. R. and Singh, R.: Identification and quantification of stick-slip induced brake groan events using experimental and analytical investigations. *Noise Control Engineering Journal*, 56(4), 235-255, 2008.

[94]   Hegde, S., and Suresh, B. S.: Study of friction induced stick-slip phenomenon in a minimal disk brake model. *Journal of Mechanical Engineering and Automation*, 5(B), 100-106, 2015.

[95]   Hetzler, H.; Seemann, W. and Schwarzer, D.: Steady-state stability and bifurcations of friction oscillators due to velocity dependent friction characteristics. *Proceedings of the Institution of Mechanical Engineers Part K Journal of Multi-body Dynamics*, 221(3), 401-412, 2007.

[96]   Hetzler, H.; Schwarzer, D. and Seemann, W.: Analytical investigation of steady-state stability and Hopf-bifurcations occurring in sliding friction oscillators with application to low-frequency disc brake noise. *Communications in Nonlinear Science and Numerical Simulation*, 12(1), 83-99, 2007.

[97]   Hetzler, H.: On the effect of nonsmooth Coulomb friction on Hopf bifurcations in a 1-DoF oscillator with self-excitation due to negative damping. *Nonlinear Dynamics*, 69(1), 601-614, 2012.

[98]   Hetzler, H.: On the effect of non-smooth Coulomb damping on flutter-type self-excitation in a non-gyroscopic circulatory 2-DoF-system. *Nonlinear Dynamics*, 73(3), 1829-1847, 2013.

[99]   Simon, K.; Seemann W. and Hetzler H.: The effect of longitudinal high-frequency in-plane vibrations on a 1-DoF friction oscillator with compliant contact. *Nonlinear Dynamics*, 88(4), 3003-3015, 2017.

[100]   Muschalle, C.: *Experimentelle Modalanalyse an einem Versuchsaufbau zur Untersuchung an Kfz-Bremsen*. Bachelor thesis, TU Berlin, 2015.

[101]   Ewins, D. J.: *Modal testing: theory and practice*. Vol. 15. Letchworth: Research studies press, 1984.

[102]   Gom mbH: 3D deformation determination of tire surfaces under extreme driving conditions. http://www.gom.com/fileadmin/user_upload/industries/tire_testing_EN.pdf, Accessed at 2016.

[103]   Glocker, C.: *Set-valued force laws: dynamics of non-smooth systems*. Springer Science and Business Media, 2013.

[104]   Hagedorn, P.: *Nichtlineare Schwingungen*. Akad. Verlag Ges., 1978.

[105]   Tustin, A.: Effects of backlash and of speed-dependent friction on the stability of closed-cycle control systems. *Electrical Engineers-Part IIA: Automatic Regulators and Servo Mechanisms*, 94(1), 143-151, 1947.

[106]   Snyman, J.: *Practical Mathematical Optimization: An Introduction To Basic Optimization Theory And Classical And New Gradient-Based Algorithms*, Springer Science and Business Media, 2005.

[107]   Lenz, W.; Eberhard O. and Manfred, K.: *Grundlagen der Steuerungs-und Regelungstechnik*. Hüthig, 1984.

[108]   Darouach, M. and Boutayeb, M.: Design of observers for descriptor systems. *IEEE transactions on Automatic Control*, 40(7), 1323-1327, 1995.

[109]   Butlin, T. and Woodhouse, J.: Friction-induced vibration: Should low-order models be believed? *Journal of Sound and Vibration*, 328(1), 92-108, 2009.

[110]   Papakos, V. and Fassois, S. D.: Multichannel identification of aircraft skeleton structures under unobservable excitation: a vector AR/ARMA framework. *Mechanical Systems and Signal Processing*, 17(6), 1271-1290, 2003.

[111]   Richardson, M. H. and David, L. F.: Parameter estimation from frequency response measurements using rational fraction polynomials. *Proceedings of the International Modal Analysis Conference*, Orlando, 167-186, 1982.

[112]   von Wagner, U.; Hochlenert, D.; Jearsiripongkul, T. and Hagedorn, P.: Active control of brake squeal via "smart pads". *SAE Technical Paper*, No. 2004-01-2773, 2004.

[113]   Hagedorn, P. and von Wagner, U.: "Smart pads": A new tool for the suppression of brake squeal? *Fortschritt-Berichte VDI*, *Reihe 12: Verkehrstechnik/Fahrzeugtechnik*, 153-172, 2004.

[114]   Farmer, C. M.; Lund, A. K.; Trempel, R. E. and Braver, E. R.: Fatal crashes of passenger vehicles before and after adding antilock braking systems. *Accident Analysis and Prevention*, 29(6), 745-757, 1997.